Master's thesis

NTNU
Norwegian University of Science and Technology
Faculty of Engineering
Department of Energy and Process Engineering

Morten Haugsvær

Computational fluid dynamic simulations of liquid ammonia spray

Master's thesis in Mechanical engineering
Supervisor: Terese Løvås
Co-supervisor: Michal T. Lewandowski
June 2023

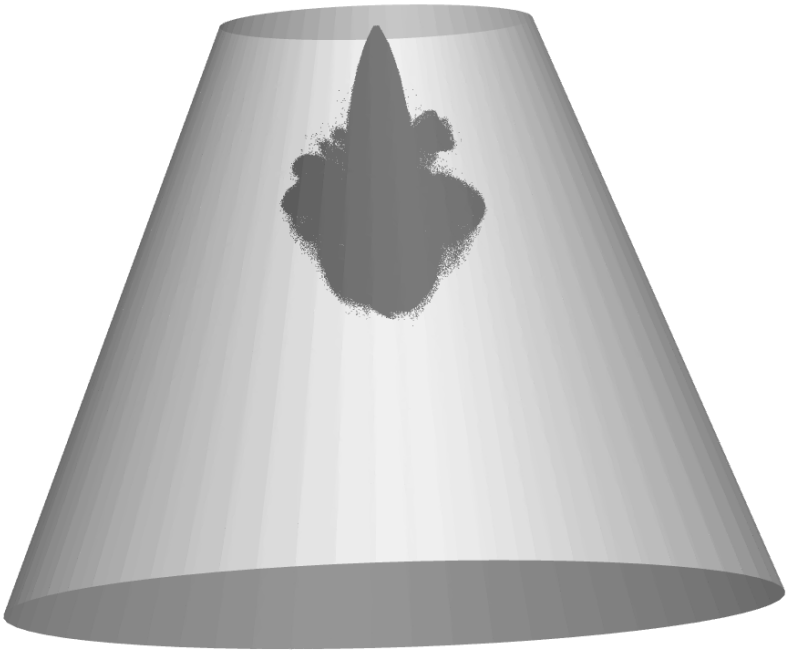

NTNU
Norwegian University of
Science and Technology

Morten Haugsvær

Computational fluid dynamic simulations of liquid ammonia spray

Master's thesis in Mechanical engineering
Supervisor: Terese Løvås
Co-supervisor: Michal T. Lewandowski
June 2023

Norwegian University of Science and Technology
Faculty of Engineering
Department of Energy and Process Engineering

NTNU
Norwegian University of
Science and Technology

Problem description

The project will focus on using 3D computational fluid dynamics (CFD), and the software CONVERGE CFD to model the spray of liquid ammonia from a gasoline direct injection (GDI) injector. The Langrangian approach will be used to model the droplets in the spray. The goal is to reproduce ammonia spray behaviour under internal combustion engine conditions. This could be useful for the development of new ammonia injection systems and strategies. To represent the spray characteristics, various models will be used to account for different spray development processes, such as break-up, evaporation, and collision. The overall process, including fuel injection and spray formation, is complex and requires proper model selection and parameter prescription under various conditions. In addition to spray formation processes, the project will focus on the injection aspects, which significantly impact spray behaviour, and settings for these must be carefully prescribed. Based on availability, new experimental data on injection aspects, such as cone angle, plume angle, actual fuel temperature, and injected mass, will be used. The influence of the most important spray models and their settings will be assessed based on experimental data from international partners. The project will specifically focus on modelling conditions where the injected liquid ammonia is subcooled, and there is no flash boiling effect, as this is more relevant for real engine applications (late rather than early injection).

Abstract

Ammonia is a potential carbonless fuel for use in internal combustion engines. However, the successful application is challenging due to the unfavourable fuel properties and concerns regarding nitrogen emissions, including N_2O and NO_x. Directly injecting liquid ammonia into the engine can improve performance and emissions characteristics compared to the more commonly investigated gaseous injection strategy. To run successful engine simulations, crucial to develop new injection strategies and for engine optimization, accurate modelling of the liquid ammonia spray is critical. In this thesis, sprays from multi-hole Gasoline Direct Injection (GDI) injectors have been modelled under multiple thermodynamic conditions with the Eulerian-Lagrangian spray modelling approach and the software Converge 3.0. Based on the available literature and recent experiments, numerical models and injection parameters to replicate the spray behaviour for various conditions were selected. The numerically calculated vapor and liquid penetration length, droplet size, and spray shape were compared to experimental values (Pelé et al. *Fuels* 2 (2021) 253-271). Under subcooled conditions, the simulations reasonably replicated spray characteristics regarding penetration and shape. However, there was a noticeable discrepancy in the obtained droplet sizes. In strong flash boiling conditions, the simulation significantly underestimated the penetration lengths, and further model development is needed to capture the flash boiling effect on phase change and droplet breakup. Additionally, sprays were set up in an engine simulation with combustion to show the application of spray modelling. Various injection strategies in an ammonia/diesel dual-fuel engine were explored, and the importance of accurate spray modelling and the prescription of injection parameters was highlighted.

Sammendrag

For å redusere utslippene innenfor maritim transport, har bruken av ammoniakk i forbrenningsmotorer blitt betraktet som en mulig løsning. Dette er utfordrende på grunn av de dårlige drivstoffsegenskapene samt at forbrenningen er svært utsatt for uønskede nitrogenutslipp som N_2O og NO_x. Ved direkte innsprøytning av flytende ammoniakk i motoren forventes forbedret ytelse og lavere uønskede utslipp sammenlignet med den mer utforskede gassinnsprøytningen. For å gjennomføre vellykkede motorsimuleringer, noe som er avgjørende for å drive motorutvikling og optimalisering, er nøyaktig modellering av ammoniakkspray viktig. I denne oppgaven ble det gjennomført simuleringer av ammoniakkspray fra gasoline direct injection (GDI) injektorer under ulike termodynamiske forhold. Dette ble utført med flerfasesimuleringer i programvaren Converge 3.0. Numeriske modeller og injeksjonsparametre for å etterligne spray ble valgt basert på tilgjengelig litteratur og nylige eksperimenter for de ulike forholdene. Spray fra simuleringene ble sammenlignet med resultater fra et nylig eksperiment (Pelé et al. *Fuels* 2 (2021) 253-271). Det ble observert god overensstemmelse med eksperimentet når trykket i omgivelsene var over damptrykket til ammoniakk, både når det gjaldt lengde og form av sprayen. Imidlertid var det et betydelige avvik i oppnådde dråpestørrelser. For trykkforhold hvor væsken var tydelig overopphetet, var det store avvik i simuleringene sammenlignet med eksperiment når det kom til sprayens lengde. Videre modellutvikling er derfor nødvendig for å ta hensyn til den hurtige faseforandringen og følgende effekt på fordampning og oppløsning av dråper for slike trykkforhold. Bruken av spraymodellering ble også demonstrert i motorsimuleringer med forbrenning. Forskjellige innsprøytningsstrategier ble utforsket i en kombinert ammoniakk- og dieselmotor, og viktigheten av nøyaktig spraymodellering og bestemmelse av injeksjonsparametere ble understreket.

Table of Contents

List of Figures

List of Tables

List of Abbreviations

AMR	Adaptive mesh refinement
bTDC	before Top dead center
CAD	Crank angle degree
CFD	Computational fluid dynamics
CI	Compression ignition
CVCC	Constant volume combustion chamber
CVC	Constant volume chamber
DICI	Direct injection compression ignition
DI	Direct injection
ECN	Engine combustion network
EPT	Institutt for energi- og prosessteknikk
GDI	Gasoline direct injection
GHG	Greenhouse gases
HPDF	High-pressure dual fuel
HRR	Heat release rate
ICE	Internal combustion engine
KH	Kelvin-Helmholtz
LES	Large eddy simulations
LHV	Lower heating value
LPL	Liquid penetration length
LPFD	Low-pressure dual fuel
NTC	No time counter
NTNU	Norges teknisk-naturvitenskapelige universitet
PDE	Partial Differential Equation
PFI	Port fuel injection
PL	Penetration length
RANS	Reynolds-averaged Navier–Stokes
RCEM	Rapid compression expansion machine
RNG	Renormalization group
RT	Rayleigh Taylor
SI	Spark ignition
SMD	Sauter mean diameter
SOI	Start of injection
TAB	Taylor breakup analogy
TDC	Top dead center
TKE	Turbulent kinetic energy
VPL	Vapor penetration length

1 Introduction

Climate change is among the greatest challenges we are facing, and urgent action is needed. The key driver to the climate crisis is the increasing levels of greenhouse gases (GHG) in the atmosphere, particularly carbon dioxide (CO_2) from burning fossil fuels. To address this issue, 195 countries signed in 2015 the Paris Agreement [1], which aims to limit global warming to below 2 degrees Celsius above levels from before the industrial revolution. The transport sector is a significant energy consumer with the potential for massive reductions in GHG emissions as it is largely dependent on petroleum-based fuel. Electrification is a promising option for short-trip and land-based transport. However, for long-distance marine transport, electrification is not a viable option because of the low power density of batteries [2]. Because of this, the search for carbon-free and low-carbon fuel sources has recently gained much attention. Finding an attractive new green fuel has shown to be an immense challenge. In addition to give satisfactory performance and low emissions. Production needs to be cost-effective, scalable, and sustainable. Furthermore, it should also facilitate easy transportation and storage.

The utilization of hydrogen as an energy carrier is regarded as promising in decarbonising the energy sector. It is widely accessible as it is the most abundant element, has a high energy density by weight and can be used directly as fuel in fuel cells and gas turbines. Even though the energy density by weight is high, the energy density by volume is extremely low, making storage and transport challenging. Hydrogen must be stored under high pressure or cooled as a cryogenic liquid and still requires 6 to 10 more space than conventional fuels [3]. To liquefy, extensive cooling to very low temperatures is needed (-253°C). Compressed is a more straightforward solution but very high pressures (200-700 bar) are required, which means high costs associated with storage [4], and at the same time, the energy density is lower than for liquid. The burning properties are another issue that makes the handling of hydrogen a challenge. The very low ignition energy and wide flammability range make it highly flammable [5].

The hydrogen carrier ammonia, NH_3, has gained a lot of interest lately as it is also a carbonless structure but with significantly simplified handling. It can be liquefied at approximately 9 bar at ambient temperature or by cooling to -33.4°C at atmospheric pressure [6]. Stored as a liquid, its storing is more expensive and volume demanding on an energy basis than conventional liquid fuel, but far better than compressed and liquefied hydrogen [7]. Production and handling of large quantities of ammonia are not new, as it is the second most produced chemical worldwide, with main applications as the nitrogen source in fertiliser production [8]. This means that infrastructure and knowledge of handling large quantities exist. Also cost on an energy basis is reasonable. The production of ammonia today comes from a well established process, making it highly scalable. It is mainly created by combining H_2 gas and N_2 through a thermocatalytic ammonia synthesis [5]. The nitrogen gas is obtained through the refinement of air. Currently, the primary source of H_2 comes from natural gas through steam reforming, resulting in what is known as "grey" hydrogen. This hydrogen can be classified as "blue" if carbon capture technology is implemented. Another option is producing hydrogen from water electrolysis using clean energy, which can then be called green hydrogen. These last two alternatives won't have any CO_2 emissions and align with the requirement for sustainability. The ammonia can be converted back to hydrogen for end use. However, this comes with a catch in cost and energy cycle efficiency and could appear that it would be more expensive compared to liquid transport of hydrogen over long distances [9]. Using it as fuel directly would then be very advantageous.

There are several ways to use ammonia directly as a fuel. It can be combusted directly in a gas turbine or internal combustion engine. Where the latter is more efficient [10] and is also better regarding infrastructure compatibility. Currently, in long-distance marine transport, ICEs are used, meaning that existing engine technology with some modifications can be used. Another option is using ammonia directly in a fuel cell. Solid oxide fuel cell (SOFC) gives better efficiencies compared to ICEs [11], however, is not competitive when it comes to power density, load response and cost. Due to this and to the better robustness of ICEs, combustion engines are a more promising choice in the near future [12][13]. Ammonia in ICE is not a new approach. Research on this topic has been conducted at two separate historical times. First, as a replacement for conventional fuel due to low supply and currently with environmental impact is a motivational factor [5]. This task

is challenging due to ammonia's many non-favourable fuel properties [5]. The high autoignition temperature makes it difficult to achieve ignition, and the low flame speed of ammonia combined with the small flammability range makes the combustion propagates very slowly, resulting in low combustion efficiency. Additionally, the high heat of evaporation gives in a cooling effect. Another challenge is the low energy density compared to conventional liquid fuel which necessitates larger fuel injections to deliver the same amount of energy into the engine. Although more fuel is required, this is not the case with air, as the stoichiometric air/fuel ratio is low compared to conventional fuel. This can be favourable air is a limiting factor in engines, but it can also easier result in lean mixtures that are harder to ignite [14].

Because of many non-favourable fuel properties, the application has shown to be difficult and faces several challenges. The low combustion efficiency results in unburned ammonia, which is undesirable both because of its toxicity [15] and regarding efficiency. Also, nitrogen emissions are an issue, and the fuel bond nitrogen in addition to the nitrogen in the air, makes the burning of ammonia extra exposed to these emissions. Besides the NO_x emissions, N_2O is also a concern. This is a GHG with warming potential about 300 times that of CO_2 on a 100-year time scale [16] and could reduce some of the climate benefits of decreased carbon emissions [17]. Different approaches for using ammonia in ICEs have been considered, and use in spark ignition (SI) and compression ignition (CI) engines have been performed. Ammonia has been successfully used as a fuel together with a more reactive fuel in SI engines. The high resistance to autoignition makes it a promising fuel for SI engines together with more reactive fuel, as shown by Ryu et al. [18] where gasoline port injection and direct injection of gaseous ammonia were considered. Moreover, Lhuillier et al. [19] considered premixed air, hydrogen and ammonia and concluded that it is a suitable fuel for modern SI engines. CI engine has a higher thermal efficiency than SI and is, therefore, more suitable for heavy-duty marine applications and energy production [5]. For instance, in international shipping, 99% of vessels in 2020 used CI engines for primary power production[7].

Due to the high auto-ignition required, a compression ratio of about 35 [20] is needed when running on only pure ammonia in a CI engine. This is much higher than usual (12-24) and is not applicable in real applications [21]. One way of coping with the poor burning properties is adding a more reactive fuel, as shown for the SI engine. Fuel injection is a crucial part of engine performance and emissions control. There exist two main ways of supplying the fuel to the engine: 1) Port fuel injection (PFI), where fuel is injected into the intake manifold and enters with air through the intake port. 2) Direct injection (DI), where fuel is brought directly into the engine [21]. Port injection of ammonia is the easiest way to convert an existing engine and is the most explored option in literature [5]. One approach considered is to inject the ammonia with port injection giving the air/fuel good time to mix and then inject the more reactive pilot fuel later with direct injection, known as low-pressure dual fuel (LPDF) mode. This has been considered by, for instance, Nadimi et al. [17] and Yousefi et al. [22][23]. Stable operation and reduction in carbon-based emissions compared to pure diesel operations were achieved. However, problems with high levels of unburned NH_3 and NO_x emissions were encountered, attributed to the wall-quenching effect, valve overlap and slow propagation of flames.

To overcome some of these issues, direct injection of the main fuel ammonia has gained considerable attention recently. Direct injection allows for higher energy density and injection pressure (i.e. more fuel can be added) and more flexible fuel injection. This approach offers several advantages and allows for more advanced injection strategies as the fuel-air mixing can be controlled more precisely. By altering the injection timing of ammonia, it is possible to achieve different combustion regimes. Also, as ammonia is stored as a liquid, injecting it as a liquid is beneficial as adding gaseous ammonia to the engine would require some extra equipment to vaporize, store and prevent condensation [24]. The direct injection of ammonia is a novel approach, and there is considerable ongoing research in this field. Where numerous aspects relating to injection strategies are being explored and investigated. E.g. Ryu et al. [25] considered direct injection of an ammonia/Dimethyl ether (DME) mixture. The most considered approach is with separate injections for pilot fuel and ammonia. Lewandowski et al. [26] have explored this approach numerically and considered different injection timings for ammonia, giving different combustion regimes. The latest ammonia injection, close to conventional diesel injection (non-premixed), was most promising regarding ammonia slip. Different emission characteristics are also encountered. Injecting both fuels close to the top dead center to overcome some of the challenges of the port injection approach and reduce unburned

ammonia and NO_x has recently attracted attention from various sources, including [7][27][28][29]. For these, both fuels are injected with high pressures in the approach known as high-pressure dual fuel (HPDF) combustion.

For developing new engines, there are various parameters to consider regarding injection strategies for engine optimization, e.g. timing and duration of fuel injections for different fuels, where to place the nozzles in relation to each other, considering interactions between pilot and main fuel spray etc. Spray modelling could be a valuable tool for developing new injection systems and strategies, and therefore is modelling and understanding of the liquid ammonia spray is of interest. Advanced experimental imaging methods can capture the main spray morphology and provide information about, e.g. droplet sizes. However, these methods face limitations close to the nozzle [30] and for specific parameters such as temperature, air/fuel ratios, and the states of the spray (liquid/vapor) [14]. Despite the limitations, experiments remain crucial in the development of reliable models. Once a good model has been established, it can provide quantitative estimates for parameters that are not easily measured. As the fuel/air mixing is crucial for the combustion and thus accurate modelling of the spray characteristics is essential for running successful engine simulations with combustion. In addition, numerical models could be valuable to understand the different physical processes occurring in spray development.

The modelling of the liquid ammonia spray is challenging for several different reasons. As it is a novel approach, there is little available literature on this field, both numerical and experimental. This is a problem for setting up the simulations, as many parameters are unknown, and for model validation purposes. The properties of ammonia differ from conventional fuels normally used in injection systems, and as a consequence, the spray behaviour varies compared to these [31]. Ammonia has a high vapor pressure which makes it exposed to flash boiling. This phenomenon happens when a liquid is entered into an environment with pressure under saturation pressure, i.e. liquid is superheated. This causes the formation and growth of bubbles inside the liquid droplets, and when the bubbles burst, this results in enhanced droplet atomization. This effect could thus be used as an advantage in creating effective injection strategies [32], but also completely changes the spray characteristics and is a challenge from a modelling perspective. The thickness of the individual plumes exiting the nozzles, the cone angle, widens, and in a multi-hole injector interactions between plumes could result in spray collapse from low pressure inside the plume rose. Also, the phase change from liquid to vapor increases compared to the subcooled conditions. Moreover, Ammonia has a high latent heat of vaporization which results in a strong cooling effect and further complicates the modelling of the vaporization process. Additionally, ammonia exhibits a low dynamic viscosity [33].

To model liquid fuel sprays, the Euler-Lagrangian approach, i.e., where the spray's droplets are handled in the Lagrangian frame, is affordable regarding computational time and is often the preferred choice. However, its accuracy largely depends on submodels employed to imitate the different spray development processes the in the spray (drag, collisions, evaporation, etc.). The choice of submodels and submodel parameters is therefore important. It can be challenging since different models must be chosen depending on the conditions, specifically when it comes to the vaporization and breakup processes of ammonia [34], due to the reasons mentioned above. Moreover, software currently lacks models to handle the intensified breakup caused by flash boiling. As a result, adjusting the constants within standard aerodynamic breakup models is necessary to imitate this behaviour.

Another challenge with this modelling approach is that the nozzles are not modelled. Thus, the effect of in-nozzle flow on spray behaviour near the nozzle must be set by injection parameters, e.g. injection rate, initial droplet size and the cone angle. And the right prescription for these is crucial for replicating sprays. While Eulerian two-phase flow simulations can capture the effects inside the nozzle, they are computationally expensive and unsuitable for large scale spray simulations in engineering applications. The flow within the nozzle is complex, and various effects affect the flow resulting in a lower mass flow than a theoretically perfectly smooth nozzle. This behaviour also varies in time during the injection. These factors must be taken into consideration when setting up simulations. One of these effects is cavitation from when the local pressure drop within the nozzle, which creates vapor bubbles. Ammonia is particularly susceptible to this due to its high vapor pressure and the low viscosity. Cavitation can affect the flow rate and droplet size and cause

vapor to exit the nozzle, a problem in Lagrangian simulations as only liquid fuel is set to enter the domain. Furthermore, different back pressures impact the flow within the nozzle [35]. Considering various conditions, input parameters need to be adjusted, and since this is a relatively unexplored topic, various assumptions must be made.

Multiple studies have successfully replicated the primary characteristics of subcooled liquid ammonia spray using standard breakup models and vaporization models available in commercial software [27][36][37][38]. However, there are still many unknowns regarding the parameters used and only a single subcooled condition was considered in these studies. Both sprays from single-hole injectors from diesel injection systems and multi-hole GDI-injectors have been attempted replicated. Multi-hole GDI injectors are being considered in this thesis and add complexity as multiple plumes and their interactions must be handled. The direction of the individual plumes must be set, and these differ from the physical angle of the injector [39]. Numerical modelling of sprays under flash boiling conditions from multi-hole GDI injectors has also been conducted very recently. Some of these studies have successfully replicated main characteristics such as the penetration length well but have not accurately captured its shape [38][37]. Zhang et al. [36] got an underprediction of liquid penetration length under strong flashing conditions. In these studies, the shape was only assessed qualitatively, and only a few conditions were considered. Input angles have also not been emphasized, and the same angles have been set for many conditions. In most cases, the cone angle is set too narrow in flash-boiling conditions as it should be increased according to experiments [33].

Late injection of ammonia is considered most promising for real engine applications, i.e. injection of ammonia near conventional diesel injection. Under these conditions, pressure in the engine is higher than vapor pressure for liquid ammonia at room temperature, as shown by [40]. This means the liquid is subcooled, and no flash boil effect must be accounted for. However, Scharl et al. [14], and Franki et al. [29] suggested preheating the ammonia fuel to cope with the bad combustion behaviour and achieve better emissions, the vapor pressure also increases, meaning that operating conditions where the spray is superheated are broadened. Additionally, an increase in fuel temperature can come from the compression process in high-pressure diesel injection systems [36] and the heating of the engine during operation. Therefore, the modelling of superheated sprays continues to be of interest.

1.1 Research question and objectives

The main objective of this study is to recreate liquid ammonia spray characteristics from a multi-hole GDI injector under multiple thermodynamic conditions. This will be achieved with the 3D computational fluid dynamics (CFD) approach with the software CONVERGE 3.0 [41] and the Eulerian-Lagrangian method for dealing with the two-phase flow of the spray.

Initially, sprays in a constant volume chamber are considered. Where first, various aspects of modelling under flash boiling conditions are assessed. To acquire knowledge on simulating flash boiling sprays and identifying the limitations of current model setups with a primary emphasis on injection parameters. This part is a continuation of the project work from the fall of 2022 [42]. The second and main part of this study is to simulate sprays under multiple thermodynamic conditions, both with and without flash boiling, to reproduce the spray characteristics accurately with a main focus on penetration length and shape. Lastly, sprays are set up in an engine simulation model with combustion. This part aims to show the application of spray modelling and explore different injection strategies in an ammonia/diesel dual-fuel engine.

1.2 Scope

Sprays validated against experimental data will only be in conditions at room temperature, and the injected liquid will also be at room temperature, given the limited time available for this work. However, it is important to note that significantly higher temperatures are expected under engine conditions, which are not addressed in this thesis.

2 Literature Review

This section includes a comprehensive literature review on liquid ammonia fuel spray. Firstly, different experiments on this topic will be presented and discussed, including their applications and how the physics compares to conventional fuels. Secondly, numerical studies using different approaches and conditions will be presented, focusing on how well experimental data is replicated. Lastly, due to the few numerical studies on flashing ammonia sprays, an overview of approaches used for modelling flash-boiling sprays of conventional fuels will be presented and discussed, focusing on how the injection, breakup and phase change aspect is handled.

In addition, this section will also include the application of direct injection of ammonia in compression ignition engines. The most promising injection strategies will be presented and discussed. This is for identifying which conditions are most important from a modelling point of view and for setting up in-engine simulations.

2.1 Ammonia spray experiments

Author	year	Injector type	Application	Comment
Okafor et al. [24]	2021	Hollow cone in swirl combustor	Gas turbine	Flame stability and emission characteristics of liquid ammonia spray combustion in micro-GT.
Pelé et al. [31]	2021	GDI 7-hole injector	ICE	Constant volume chamber (CVC) heated and pressurized to different conditions. Subcooled and superheated spray.
Cheng et al. [43]	2021	GDI hollow cone	ICE	CVC at different ambient pressure. Several injection pressures and needle lifts considered.
Li T. et al. [27]/ Zhou et al.[7]	2022	Diesel single hole	ICE	Constant volume combustion chamber (CVCC) with thermodynamic conditions as at TDC. One condition considered (subcooled.)
Li S. et al. [33]	2022	Diesel single hole	ICE	CVC at various pressures, fuel heated to different temperatures. Only superheated liquid spray.
Scharl et al. [14]	2022	Diesel single hole	ICE	RCEM three different injection pressures. Non-reactive ambient conditions.
Zhang et al. [44]	2023	Diesel single hole	ICE	One condition considered (subcooled). Ambient at room temperature.
Fang et al. [45]	2023	Diesel single hole	ICE	Superheated and subcooled. High injection pressures (500 - 1000 bar).
Bjørgen et al. (NTNU lab not published)	2023	GDI 6-hole injector	ICE	CVC Multiple pressures for injection and in chamber considered. Ambient at room temperatures.

Table 1: Summary of liquid ammonia spray experiments in literature.

Direct injection of liquid ammonia is a relatively new approach, and the ammonia liquid spray is little explored experimentally. However, a few studies exist, which will be presented in the following section to the best of my knowledge, focusing on non-reactive sprays. There has been a significant increase in activity in this area of research, with many papers published in the last

few years. The studies have primarily focused on the use of single-hole diesel injectors and very high injection pressures exceeding 500 bar. For this work, the two known experiments on multi-hole GDI injectors are the most relevant and will be highlighted. While the use of ammonia in a diesel injection system is not directly comparable to a GDI system, studying how different conditions affect the spray and how it compares to other fuels can still provide valuable insights. Additionally, as the system uses a single-hole injector, there are no plume interactions, unlike a multi-hole injector. Understanding how the spray angle, equal to the cone angle in a single-hole injector, changes in different conditions is also valuable for setting up simulations. An overview of the various spray experiments considering spray characteristics is shown in Table 1. For sprays under/near flash boiling conditions, the superheat degree, here expressed as the ratio of ambient to saturation pressure, $\frac{P_a}{P_s}$, is crucial for describing spray formation [32] and will be used to compare conditions.

The first known study on liquid ammonia spray and combustion was by Okafor et al. [24] and explored the injection of liquid ammonia spray in gas turbines co-fired with methane. The system used here differs significantly from those employed in ICEs and operates at much lower pressures for both injection and ambient conditions. Although not directly comparable, this study discusses some challenges of introducing liquid ammonia into the combustion chamber. Cavitation in the nozzle was an issue, and extra cooling had to be added to the liquid supply to prevent phase change in the nozzle.

Pelé et al. [31] conducted the first experimental investigation on the characteristics of ammonia spray using a multi-hole GDI injector (7 holes with orifice diameter 150 μm). The experiment involved injecting the spray into a constant volume chamber (CVC) at an injection pressure of 120 bar while varying the ambient temperature between 293 and 393 K and ambient air densities; for the ambient temperature of 293 K, the pressure was varied between 2 and 25 bar. Spray features were compared to that of the conventional fuels more common in GDI-injectors, gasoline and ethanol. The injected liquid was assumed to be 293 K. Thus; the considered conditions were in the range with $\frac{P_a}{P_s}$ from 0.23 to 2.91. High-speed Schlieren imaging was used to monitor both the liquid and vapor phases. This experiment showed that liquid ammonia's spray characteristics differ from conventional GDI fuels and are more sensitive to air pressure and temperature differences. The spray characteristic of ammonia is generally longer and thinner than gasoline and ethanol, both at high and low pressure (flashing and non-flashing). Generally little difference between penetration lengths for liquid and vapor. In Pelés study, the widest spray was found for ambient pressures around saturation pressure for ammonia, i.e. $\frac{p_a}{p_s} = 1$, which is in contrast to conventional fuels where the widest spray was observed at $\frac{P_a}{P_s} = 0.3$ as reported by Xu et al. [32]. The elongated and thin shape of the ammonia spray was found to be a disadvantage for adapting to engines currently fitted with GDI injectors with conventional fuels due to the likelihood of wall contact when $\frac{P_a}{P_s} << 1$. The data obtained from this study will be used to set up numerical simulations and validate them.

Cheng et al. [43] conducted an experimental study on ammonia spray characteristics of liquid ammonia spray in a CVC with a hollow cone (nozzle as a ring, gives hollow spray pattern in the middle) GDI piezoelectric injector. Characteristics such as penetration, spray angle and cross-section area were compared to methanol and ethanol in ICE-relevant conditions. Different injection pressures varying from 40-100 bar and ambient pressures of 5, 10 and 15 were considered. The temperature was not stated, But if ammonia were at room temperature or higher, at least one condition is superheated. If fuel is at room temperature 5 bar means $\frac{P_a}{P_s} = 0.58$ i.e. transitional flash boiling [32]. Ammonia was found to differ from the other fuels with longer penetration length, larger spray angle and cross-section area. The difference in behaviour was explained due to the lower density and viscosity. Additionally, the evaporation process of ammonia was stated to be faster due to the higher vapor pressure.

Li T et al. [27] and Zhou et al. [7] (Same experiment mentioned in both articles). Conducted the first experiment with high-pressure injection in conditions of CI engine near TDC. This experiment was done with a single-nozzle diesel injector and an injection pressure of 600 bar. This experiment aimed to validate spray models used to model combustion in an engine environment. One condition was tested with engine-like conditions at ambient temperatures and pressures of 900 K and 48 bar, respectively, achieved in a constant-volume combustion chamber (CVCC). A fuel temperature of

350 K results in a superheat degree of $\frac{P_a}{P_a}$ of 1.24. No oxygen was present in the chamber to prevent combustion. The high-speed schlieren method was used to capture the vapor phase, and the diffused back-illumination method was used to capture the liquid phase. Making it possible to capture penetration lengths for liquid and vapor and the shape of the plume. A clear separation between liquid and vapour penetration length was found for these conditions.

Also Scharl et al. [14] conducted a spray experiment in a non-reactive atmosphere for spray model validation purposes. To validate a 1D spray model used to obtain quantitative info on equivalence ratio, temperature and mixing, which is difficult to obtain experimentally. In this experiment, two different single nozzles injectors were considered with diameters of 980 and 940 μm and injection pressures of 265 and 530 bar. This was done to ensure the model is valid independent of the injector. The experiment was conducted in an optical accessible rapid compression expansion machine (RCEM) to achieve engine-like conditions with ambient temperature and pressure of 920 K and 125 bar. Given a liquid fuel temperature of 293 K, the injected liquid is subcooled. Cone angles of approximately 25 degrees were measured for both injections.

Li S. et al. [33], from the same research group as [27][7], conducted the first extensive study on the characteristics of superheated liquid ammonia spray. The study considered various flashing conditions and employed a single-hole diesel injector and high-speed diffused back-illumination to observe the spray characteristics in an optical accessible CVC. The injection pressure used of 300 bar is low for a diesel system making this study more comparable to GDI compared to the other diesel injections. Both the fuel temperatures (308 K, 323 K, and 338 K) and ambient pressures were changed to cover many superheat degrees. Both the macro and microscopic characteristics of the spray were considered, focusing on the bubble explosion intensity in the near field and the penetration length and cone angle in the far field. Characteristics were also compared to the fuels Methanol and n-hexane. Spray from ammonia was found to be smaller near the injector under all superheated conditions compared to these. The spray characteristics could be divided into three regions based on $\frac{P_a}{P_a}$: 1-0.5 initial flashing, 0.5-0.2 for transitional flash boiling, and < 0.2 for flare-flash boiling. This is similar to [32], but there only two different regions were used for flashing (1-0.3 and <0.3). In the initial flashing region, superheat degree was found to have little effect on near-field behaviour, and the spray evolution in the far field was similar to traditional diesel. Below 0.5, transitional and flare flash region, there was a significant effect near the nozzle due to the rapid bubble explosions. The authors proposed relations for near-field bubble explosion intensity near the nozzle for the different flashing regions. The relations were functions of superheat degree, viscosity and the non-dimensional Ohnesorge number (Oh), which represents the ratio of internal viscosity dissipation to surface tension energy. Superheat degree and viscosity are important for the bubble explosion intensity in the whole flashing region, while for $\frac{P_a}{P_a} < 0.5$, the Oh number has a more important role. The cone angle obtained from this study will be used as model input, and the characterisation based on the degree of superheating will be used for model selection.

Zhang et al. [44] investigated the characteristic of ammonia spray to see how it compared to diesel spray. The study was conducted at room temperature and 15 bar ambient pressure, with a single-hole injector and injection pressure of 500 bar. The fuel temperature is not known, but the spray was likely subcooled. High-speed photography was used to observe the sprays liquid penetration and angle. The ammonia spray's behaviour was similar to that of diesel spray under considered conditions. The liquid penetration length of ammonia was longer than diesel right after the start of injection due to its lower viscosity. However, due to the faster evaporation caused by the lower boiling point of ammonia, the penetration length became shorter after a while, and the spray angle got wider than diesel. A spray angle of around 18° for ammonia was reported.

Fang et al. [45] investigated the effects of flash boiling on high-pressure injection of ammonia using a single-hole diesel injector. They used injection pressures between 500-1000 bar and a fuel temperature of 300 K. The diffusive back illumination method was used to study the spray characteristics. The study found that cavitation inside the nozzle caused lower liquid penetration at the start of injection for $\frac{P_a}{P_s} < 0.65$, and was referred to as the "spray resistance phenomenon". Additionally, more superheating was found to give wider sprays near the nozzle (cone angle), with the width increasing with increasing superheating. The increase in width was greatest at $\frac{P_a}{P_s} < 0.3$, which corresponds to the full flash boiling regime [32], and was explained due to bubbles exploding at the nozzle exit.

Gaucherand et al. [35] investigated numerically the internal flow of liquid ammonia in a GDI injector. This was done with two-phase Eulerian flow simulations. The injector considered have six holes with orifice diameters of 227 µm. An injection pressure of 200 bar and a liquid ammonia temperature of 300 K were used, along with various back pressures. The study reported phase change within the nozzle, and two sources were identified for vapor formation inside nozzles, heat transfer from the walls and cavitation. The geometry of the injector was found to be crucial, as well as the outlet pressure. Ammonia was considered exposed due to the fuel properties viscosity and vapor pressure, and a considerable amount of vapor exited the nozzle for low back pressures. The study concludes that for outlet conditions of 1 bar ($\frac{P_a}{P_s} = 0.094$), the liquid fractions exiting was 0.2 while for a pressure of 40 bar, liquid fractions were 0.95. The discharge coefficient also increased with the back pressures and was for these two cases 0.65 and 0.71, respectively.

Bjørgen et al. [46] at NTNU have done several experiments on ammonia injections using a GDI multi-hole injector. The same injector is considered by [35] and is fitted in the modified research engine at NTNU. In a recent convention paper, this injector's momentum flux and mass flow were presented. The study considered two different back pressures, 2 bar ($\frac{P_a}{P_s} = 0.23$) and 20 bar, and an injection pressure of 200 bar, with the ammonia temperature set at 293 K. When the back pressure was raised, a decline in discharge coefficient were observed. It was 0.54 and 0.48 for the low and high back pressure, respectively. The study showed that the momentum flux varies during the injection process. It reaches a peak immediately after the start of injection, followed by a decrease in momentum, and then shows another increase until the end of injection. The spray behaviour from this injector was also investigated in a constant volume chamber but are not published yet. This thesis will use pictures of sprays captured from this experimental setup and the momentum flux profile to set up simulations.

2.2 Ammonia spray simulations

This section will address studies on modelling liquid ammonia spray using the Eulerian-Lagrangian approach, where simulations are validated against experimental data. The setups used for validation are:

- Pelé et al.[31] - Multi-hole GDI injector under flashing and non-flashing conditions (ambient temperature 293-393 K).
- Li T. et al.[27][7] - Single-hole Diesel injector under non-flash engine conditions (ambient temperature 900 k).
- Li S. et al. [33] - Single hole Diesel injector under flashing conditions (room temperature).

An overview is presented in Table 2 to the best of my knowledge as this field of research has had much activity lately with several articles being available during spring 2023, e.g. the paper by Pandal et al. [38] was made available mid-April. How the various authors have dealt with modelling the injection (initial droplet size, input angles), spray breakup, and phase change process will be emphasized. Unless otherwise specified, the turbulence in the Eulerian phase is modelled using RANS RNG k-ϵ.

In the internal report from the research project ACTIVATE [34], Lewandowski et al. simulated the spray from [31] with ambient at room temperature and $\frac{P_a}{P_s}$ of 0.23. The effect of different submodels and settings found especially influential for modelling flashing sprays were assessed. These were models for evaporation, models for the breakup and input angles. Different evaporation models (Chiang, Frossling) with and without Price addition for flash boiling were considered. The KH-RT breakup model was set up with four different sets of constants (GDI non-flash, GDI flash, Diesel and as Duronio et al. [30]). The injection was modelled using blob distribution, and three different sets of input angles were investigated. The two input angles were set to match the experimental full spray angle. In the first set, the plume angle was set equal to the injector drill angle, in the second, the cone angle was increased by 50 % compared to the first, and in the third set, the relation between the two input angles was adopted by [30]. This resulted in cone angles of 10° 15°

and 20.9°. Vapor penetration length was in good agreement with experimental data, but none of the setups could reproduce liquid penetration lengths, which was greatly underestimated. It was hypothesized that the actual fuel temperature was reduced due to phase change inside the nozzle leading to too much evaporation in the current setup. However, in these simulations, the larger step diameter of 365 µm and a mass of 150 mg was used, much higher than the measured injected mass of ca. 40 mg.

A group in Italy have replicated ammonia spray from [31] with two different software. In the fall of 2022, Battistoni et al. [37] presented spray simulations at the 1st symposium on ammonia in Cardiff using the software Converge v3.0. The conditions with ambient pressures of 2 bar and 15 bar ($\frac{P_a}{P_s}$ 0.23 and 1.74) and no heating of the chamber were considered. Vapor and liquid penetration and droplet sizes from five locations were compared to experimental values. The blob injection model with a cone angle of 25° for the superheated case and 20° for the subcooled was used. For vaporization, Frossling correlation with Price for the flash boil was applied. KH-RT model was used to model breakup, and the constants were tuned for both conditions based on droplet size measurements. The other models used for the discretized phase were the dynamic drop drag and NTC collision models. The standard $k-\epsilon$ model was applied for the continuous phase turbulence modelling. The number of injected parcels was not stated, and the finest mesh size was set to 0.25 mm. The results were in good agreement with experimental values. However, they were only shown for the first half of the injection (2 ms), and some underpredictions and overpredictions of penetration length were found for the superheated and subcooled condition, respectively.

In mid-April 2023, the same authors published a study [38], This time with Pandal as the first author. The same two conditions as previously were considered, but this time using the solver sprayFoam from the open source software OpenFOAM. The paper includes a grid sensitivity study and a parametric study on the turbulence model and cone angle to set up a configuration best replicating experimental values. A mesh size of 1 mm in the axial and 0.61 mm in the radial directions was chosen as sufficient, and 27 000 parcels were injected. The standard $k-\epsilon$ turbulence was applied with a modified $C_{\epsilon 1}$ constant (eq. 16) from 1.44 to 1.55 (i.e. enhanced production of dissipation, ϵ, resulting in less radial dispersion and thus longer penetration). The blob injection model was applied, and a cone angle of 20° was set for both conditions. For calculating breakup, the KH-RT model was used and set up as recommended (rec. GDI non-flash) for flashing and modified for the subcooled case ($B1 = 40$ and $C_{RT} = 0.1$). To calculate phase change, a flashing vaporization model by Zuo et al.[47] was applied, which utilizes the Adachi correlations [48] for calculating heat transfer for superheated droplets (same as in Price model [49]). The simulated penetration lengths were in good agreement with experimental values but were only shown for half the injection duration. Some discrepancy between simulations and experimental data was experienced as droplet sizes obtained were underpredicted for the subcooled case, and spray collapse in the superheated case was not well captured.

In my project work in fall 2022 [42], an attempt was made to replicate the most superheated condition by [31]. The condition with $\frac{P_a}{P_s}$ of 0.23 also considered by [37][34] was attempted reproduced. The software used was Converge v3.0 and a similar set of submodels as [30][34][37]. A parameter study was conducted for parameters, and submodels thought crucial for spray modelling flash boiling, looking at the effect on penetration lengths, spray morphology and droplet size at a specified location and for the entire spray. The minimum mesh size was set to 0.25 mm, and 512 000 parcels were injected per nozzle. A blob injection model was used for modelling the input, and several different input angles were considered. The locations of the nozzle holes were also simplified. The breakup model was set to KH-RT with many different configurations of constants considered. To model the phase change of droplets, the Frossling correlation with Price additions was chosen with both the uniform temperature model and the more accurate discretized temperature model for the larger droplets. The use of the discretized temperature model slowed down evaporation resulting in less separation between liquid and vapor penetration and better agreement with the experiment. Also, the spray collapse effect was improved. The penetration lengths obtained were generally underpredicted compared to the experiment. Setups with small cone angles or decreased fuel temperatures (resulting in increased droplet sizes) and increased initial droplet velocity gave penetration lengths closer to the experiment, but for these setups, the shape was not accurately replicated.

Zhang et al. [36] conducted an extensive numerical study of an ammonia spray. Both experiments from [27] and [31] were used for validation. Conditions from [31] included both different pressures and ambient temperatures. In addition to this, ethanol sprays were also simulated. The two superheated conditions were of $\frac{P_a}{P_s}$ of 0.23 and 0.31, with ambient temperatures of 293 K and 393 K, respectively. The software used was Converge v3.0, and the mesh was set to a minimum of 0.5 mm based on a grid independence study. The initial droplet diameters were determined from a chi-squared distribution, and the prescribed input angles for ammonia spray were set to 20° and 15° for cone and plume angles, respectively. The KH-RT model determined the breakup, and constants were fine-tuned for the flashing conditions, but how this was set up other than that $B1$ was set to 10 was not stated. The Frossling correlation with and without the Price flash boiling model was considered in addition to a conventional boiling model to calculate vaporization. The study concludes that the current setup can replicate subcooled sprays well with slight overpredictions. However, the liquid penetration was significantly underestimated for the flashing cases when using the Frossling models. Also, no difference in results was experienced with/without the Price model. Using the conventional boiling model, the liquid penetration is closer to the experiment. However, the shape was not replicated, i.e. the model does not capture the physics of the spray. The authors stated that an improved flash boiling model that also considers the thermal (flash boiling induced) breakup is needed for modelling highly superheated sprays. It was hypothesized that more breakup resulting in smaller droplets could actually increase liquid penetration length due to the low vaporization rate of small droplets, given the strong cooling effect. The importance of setting up a plume angle for flashing sprays from multi-hole injectors to capture the collapse effect was also highlighted. In this article, the stated nozzle diameter is the step diameter of 365 µm which is significantly larger than the orifice diameter of 150 µm. If this diameter was used for modelling and if the injected mass were close to as in the experiment or estimated based on the larger diameter as in [34] is unknown.

Li T. et al. [27]/[7] simulated the spray from their experiment to validate a submodel setup to use in engine simulation. The software Converge was used, and from a grid independence study, a minimum mesh size of 0.45 mm was assessed as sufficient. Both Large Eddy Simulations (LES) and RANS $k-\epsilon$ RNG models were used to resolve the turbulence in the Eulerian phase. Still, the additional accuracy in LES simulations was considered not worth it regarding computational cost since it should also be coupled with chemical kinetics. The model used for the injection was not stated other than that initial droplet distribution is based on nozzle size. The KH-RT breakup model was modified, and the modified constants were set to $B1 = 36$, $C_{RT} = 0.68$ and $C_{bl} = 18$. For evaporation, the Frossling correlation was applied. Also, contrary to my project work and [34][30], the Turbulent Kinetic Energy (TKE) preserving model for turbulent dispersion is used instead of O'Rourke. The authors concluded that the current setup could replicate the ammonia spray's liquid and vapor phase under engine conditions near diesel injection timings.

Shin and Park [50] simulated the superheated sprays from the test rig by [33]. This was done with the Software Converge v3.0 and a minimum mesh size of 0.125 mm (both temperature and velocity AMR criterion). To decide the initial droplet size, the blob model was used, and the cone angle was set to 40° for all conditions. KH-RT and a developed thermal breakup model were used to model the breakup. The KH-RT model was modified, and the constant that differs from recommended GDI non-flash were $B1 = 100$ and $C_{RT} = 0.7$. The thermal breakup model is based on bubble dynamics and models the fundamental steps in flash boiling (bubble nucleation, bubble growth and droplet burst). The thermal breakup was set to work on a time step one-twelfth of the time step for the conventional breakup. The vaporization was calculated using the Frossling correlation with and without the Price model. Liquid penetration length with the Price model was in poor agreement with the experiment due to excessive evaporation compared to the conventional evaporation model. Therefore only the latter was used in the rest of the results. Fourteen different conditions were simulated, and good agreement of liquid penetration length with the experiment, however for the conditions where the fuel was heated to 338 K and $\frac{P_a}{P_s} > 0.3$, differences up to 10% was experienced.

An et al. [51] also simulated sprays from the test rig of [33]. Twelve different conditions were considered. They used their own solver in the open-source software OpenFOAM. The turbulent motions in the Eulerian phase were solved using LES, and a minimum mesh size of 0.125 mm was used. The size of the injected parcels was from a Rosin-Rammler distribution model with the

largest and smallest sizes based on turbulent length scales. The max size was set by the largest turbulent eddies or nozzle, and the Taylor microscale set the lower limit. For the condition of $\frac{P_a}{P_s} = 0.1$, a mean droplet size of 14 µm (min 3.6 and max 119 µm) was used with shape and scale parameters of 1.4 and 9.5, respectively. For comparison, the nozzle size is 280 µm. A parametric study examined the effect of different initial droplet size distributions. The cone angles used were from the considered experiment and varied with conditions. Five different vaporization models were assessed; two equilibrium models, a non-equilibrium evaporation model, a flash boiling model (same as Pandal [38]), and a combined model. The article concludes that conventional models significantly overestimate evaporation and that the two others are closer to experimental values, with the combined model performing best. The authors highlighted that the initial particle size distribution is important for simulating spray characteristics and must be carefully described. Distributions with the largest mean particle performed worst.

Apart from simulations validated experimental data, some other articles with simulations of liquid ammonia sprays in engine simulations are known of. Frankl et al. [29] simulated subcooled ammonia with the software Converge set up with KH-RT breakup. Wang et al. [52] and Liu et al. [53] (same setup) also simulated liquid ammonia spray in engine simulations. They also used Converge with KH-RT breakup. The breakup model was set up with constants as recommended for GDI non-flash, which was justified due to the physical similarity of gasoline. To model evaporation, the Frossling correlation was applied.

In summary, the current models are reported to be able to replicate subcooled sprays. However, replicating ammonia spray under flashing conditions without thermal breakup is challenging. Although some have replicated the main characteristics of penetration length and droplet size, less agreement with the shape of the spray was encountered. In addition, cone angles which do not align with the experiments are used.

Author	Year	Experiment	Software	Flash boiling	Cone angle input (°)
Lewandowski et al. [34] (internal report)	2022	[31]	Converge	Y	10 , 15 and 20.9.
Battosini et al. (Presented at convention) [37]	2022	[31]	Converge	Y/N	Flashing 25, non flash 20.
Li T. et al. [27], Zhou et al. [7]	2022	[27]/[7]	Converge	N	N/A
Haugsvær (Project work) [42]	2022	[31]	Converge	Y	Several cones considered.
An et al. [51]	2023	[33]	OpenFOAM	Y	Varying angle based on experimental data.
Zhang et al. [36]	2023	[31] + [27]/[7]	Converge	Y/N	20 for flash and non flash. Also same for the GDI and diesel type injector.
Shin et al. [50]	2023	[33]	Converge	Y	40 for all Conditions.
Pandal et al. [38] (same authors as [37])	2023	[31]	OpenFOAM	Y/N	Flashing and non flash 20.

Table 2: Summary of liquid ammonia Eulerian-Lagrangian spray simulations. Simulations validated against experimental data.

2.3 Flash boiling spray modelling

At the start of the preliminary project work leading to this thesis, no 3D CFD simulations on flash boiling ammonia sprays were published. And only the papers by Li T et al. [27][7] on the simulation of subcooled sprays were available. Approaches used in previous Eulerian-Lagrangian simulations of flash boiling fuel sprays and the physics of the spray will be presented. The main emphasis is how injection, breakup and phase change are modelled. An overview is shown in Table 3 together with the recent ammonia studies mentioned in the above section.

Author (year)	Fuel	Thermal breakup	Comment
Price et al. [54] (2018)	N-pentane/ iso-octane	N	Superheated droplet model, flash boiling effective nozzle model, cone angle based on superheat relation [55].
Price et al. [56] (2019)	N-Pentane	Y	Thermal breakup model, flash boiling effective diameter model.
Duronio ey al. [30](2020)	Iso-octane	N	Superheated droplet model, modified KH-RT.
Duronio et al. [57] (2022)	N-hexane / Iso-octane	Y	Eulerian modelling of nozzle coupled with lagrangian spray modelling. Superheated droplet model.
Gao et al. [58] (2022)	Iso-octane, hexane and ethanol + mixtures	Y	Thermal breakup model incorporated into the TAB breakup model.
Battosini [37] (2022) (presented at convention)	Ammonia	N	Modified KH-RT, blob injection model and superheated droplet model.
An et al. [51] (2022)	Ammonia	N	Different phase change models, Initial droplets based on turbulent length scales, Cone angle based on exp.
Zhang et al.[36] (2023)	Ammonia	N	KH-RT breakup, specified initial droplet diameter same cone as for subcooled
Shin et al.[50] (2023)	Ammonia	Y	Thermal breakup model, blob injection, Cone angle const. 40°.
Pandal [38] (2023)	Ammonia	N	Superheated droplet mode, KH-RT, blob injection model, modified turbulence model, same cone as subcooled.

Table 3: Overview over Lagrangian modelling of flash boiling fuel sprays and the approaches used.

Price has been the first author of several articles regarding flash boiling fuel sprays from GDI multihole injectors. And is behind the widely used flash boiling vaporization model based on the Adachi [48] correlation to account for the additional heat transfer from superheated fuel droplets [59]. This model was first introduced in an article from 2015 on the modelling of superheated and subcooled sprays from a GDI injector using the software STAR-CD. In this article the breakup was modelled using a highly modified Reitz-Diwakar aerodynamic breakup model [60], similar to the KH-RT model, and specified the initial droplet size for injection. The authors could accurately replicate spray characteristics by setting the appropriate initial droplet size and cone angle. For highly superheated fuels, both vapor and liquid exit the nozzle resulting in much smaller initial liquid droplets compared to nozzle geometry. Choosing an appropriate initial droplet size was therefore stated to be challenging. Also, the cone angle changes with conditions and has to be changed. To address these issues, a flash boiling effective nozzle model was proposed [54] to quantify the effect of in-nozzle phase change on initial droplet size. To quantify the change in cone angle, an empirical relation based on superheat degree and fuel properties was adopted from [55]. The model setup was applied to several different injectors, conditions and fuels and captured important spray

characteristics like spray collapse. The cone angle relations were said to give some improvement, but a more accurate modelling of the widening effect was proposed. In 2019 the same Authors [56] developed a thermal breakup model that captures the enhanced breakup caused by bubbles growing within superheated liquid droplets, as previous approaches for achieving smaller droplets were based on adjusting certain constants in the aerodynamic breakup model. This was done by modelling nucleation and growth of bubbles inside droplets. The smaller droplets after the breakup were given radial velocity; thus, the model could capture the plume widening effect and no longer rely on empirical cone angle relation. The thermal breakup model was used with the flash boiling effective nozzle model and was reported to be in good agreement with the experiment regarding penetration lengths and droplet size.

Duronio et al. [30] reconstructed the ECN spray G [61] (multi-hole GDI injector with an injection pressure of 200 bar) using the models available in the software Converge v3.0. A mesh refined up to 0.125 mm was utilized. One superheated condition of $\frac{P_a}{P_s}$ of 0.26 and the standard subcooled case were considered. The initial droplet size approach is unknown. The cone was set to an angle of 24° for flashing and 30° for non-flash. The plume angle is also reduced from non-flash to flash, and also the relation between the angles is significantly altered. The breakup model KH-RT is applied with significantly altered RT constants to enhance breakup and are $C_{RT} = 0.15$ and $C1 = 0.1$. This is similar to recommended for GDI flash but with a further reduced C_{RT}. In addition to this, the $B1$ constant is slightly lowered. For Vaporization, The Frossling correlation with the Price flashing model is applied with the use of the more accurate discretized temperature model for larger droplets. This setup achieved an excellent agreement with experimental penetration lengths, and the shape was accurately reproduced with the spray collapse phenomena well captured. Some discrepancies between numerical and experimental were however found for droplet size. A similar set of submodels for the discretized will be used in this thesis. However, not the same turbulence model as the standard $k - \epsilon$ was applied here.

Although accurate reconstruction of main spray morphology for flashing spray. Only one superheat degree was considered and significant tuning of breakup parameters was performed. Also, a reduced cone angle for the superheated case is the opposite of what is observed experimentally. Moreover, relying on extensive tuning of parameters is not an optimal approach for engineering applications. To address these issues, Duronio et al. [57] simulated again the ECN spray G [61] with another approach more suitable for flashing sprays. This time an additional fuel and different injection pressures were also considered. This time the nozzle was modelled using the Eulerian-Eulerian method and data from this simulation were used as input for the Eulerian-Lagranginan modelling. I.e. Initial droplet size, mass flow rate and input angles were obtained from the computationally expensive and accurate two-phase modelling with a minimum mesh size of 25 µm. This resulted in a cone angle of 36° whereas an angle of 24° was used in the previous study. A user-defined model also considering the thermal breakup mechanism was added to model the breakup. In this model, the thermal breakup is computed first as this breakup has a shorter timescale [50] and then aerodynamic breakup based on the Reitz-Diwakar model [60] is calculated. The thermal breakup model is based on bubble dynamics and resembles that of the abovementioned [56][50]. The evaporation was based on the Frossling correlation with the Price flash boiling addition. The nozzle modelling captures well the cone angles and mass flow rate from the experiment. Coupled with the Lagrangian modelling, good agreement was observed for both liquid and vapor penetration. This was a notable improvement compared to the KH-RT breakup model. Additionally, the droplet size is also in better agreement with the observed data. Also, it was observed that higher injection pressure results in smaller droplets, which in turn helps to avoid spray collapse and facilitates faster evaporation.

Gao et al. [58] has also developed a model that considers thermal breakup. They did this using the software KIVA-3V. The thermal breakup is modelled after the same principles as the model of [57][50][56]. The model was tested with two fuel blends at numerous superheat degrees. The thermal breakup model was incorporated into the aerodynamic TAB (Taylor breakup analogy) breakup model [62], resulting in a unified model. The model considers a competing breakup criterion between thermal and aerodynamic breakup. The study found good agreement between the model and experimental results, capturing the spray characteristics under different degrees of superheat degree, including liquid penetration length, plume interactions (important for collapse effect), and droplet size.

In summary, capturing the main characteristics of flashing sprays without the standard submodels (no thermal breakup) is possible. However, significant modifications are required. Involving considerable tweaking of initial droplet size, spray angles, and breakup constants, which may vary considerably depending on the degree of conditions. As a result, this approach may not be appropriate for engineering applications and thermal breakup models are preferred for strong flashing sprays.

2.4 Ammonia spray in engine

Direct injection of ammonia in internal combustion engines is a novel approach, and literature in this field is limited. Some numerical and experimental exists and will be presented. This section aims to get an overview of promising injection timings of ammonia and the corresponding conditions, i.e. what is most important from a modelling point of view. In addition, this review examines promising injection strategies, including injection timings and interactions between sprays, which is valuable for setting up the engine simulation in the last part of the thesis.

Ryu et al. [25] conducted experimental studies on the combustion and emission characteristics of a blend of NH3 and dimethyl ether (DME) in a CI engine using a GDI injector. A single-cylinder engine with a compression ratio of 20 was used. DME was chosen due to its similar vapor pressure, good burning properties, and fuel energy cost to diesel. Different fractions of NH3 and DME were considered, and the results showed that increasing the ammonia concentration led to decreased engine performance. Ammonia caused longer ignition delays, limited engine load conditions, and decreased combustion temperature, resulting in higher CO and hydrocarbon emissions, while NO_x emissions increased due to the formation of fuel NO_x. Advancing the injection timing was necessary for successful engine operation as the ammonia content in the fuel mixture increased. High ammonia concentration could not successfully run at conventional diesel injection timing due to the in-cylinder air cooling and slow chemical kinetics. The best combustion characteristics for the case with the highest ammonia concentration (60/40 ammonia/DME) were achieved for early injection, meaning that low pressures are expected and that flash boiling is likely.

Zhang et al. [44] investigated the use of dual direct injection of ammonia and diesel in a low-speed two-stroke CI engine experimentally. Combustion of ammonia was done with the diesel jet-controlled compression ignition (JCCI) concept, where the main combustion is ignited with jets from an ignition chamber. 50% of the energy was supplied from ammonia, and performance and emissions were compared to pure diesel operation. The study investigated various timings and quantities of ammonia injection, and different diesel injection timings. Varying the ammonia start of injection allowed them to explore different combustion regimes. When the ammonia injection was advanced too much, ignition of all ammonia was found difficult. Injecting ammonia and diesel fuel simultaneously was considered best regarding emissions and engine performance. When injecting ammonia later, the total combustion duration increased and the thermal efficiency decreased.

Lewandowski et al. [26] conducted a numerical study on a single-cylinder compression ignition engine using direct injection of both diesel and ammonia. They used a diesel injector and a GDI injector for ammonia, studying ammonia spray evaporation, cooling, mixture formation and combustion. 50% of the energy was provided by ammonia. Three different injection timings for ammonia were considered, representing three different combustion regimes; premixed, partially premixed and non-premixed. With ammonia at room temperature, the two latest injection timings correspond to subcooled conditions. They found that the later ammonia injection, which was injected 5 CAD before diesel, performed best and had the highest combustion efficiency. This injection timing also led to the highest NO_x emissions, but this was due to burning more ammonia. The earliest injection showed similar behaviour as port fuel injection and suffered from unburned ammonia. It was suggested that ammonia injection after diesel should also be considered. Also, interactions between sprays could also increase combustion efficiency and lower emissions. The same engine setup used here will be used later in the thesis, but at different operating conditions and with a modified diesel injector with welded nozzles to provide a lower mass flow.

In the following studies, both ammonia and the pilot fuel are injected with high pressures separately and close to the top dead centre, known as the high-pressure dual fuel (HPDF) combustion

approach.

In 2020, Frankl et al. [29] conducted a numerical investigation on the dual direct injection of ammonia/diesel and hydrogen/diesel in a dual-fuel marine engine. However, the setup was not validated for ammonia and did not analyze emissions and thermal efficiency. In this study, ammonia was injected after the pilot fuel. Compared to hydrogen, the ignition was delayed due to its low flammability range, high latent heat of vaporization, and ignition temperature. The study concludes that ammonia is suitable for this dual-fuel direct injection. To increase the combustion efficiency, preheating ammonia was suggested. To improve the ignition, a suggestion was made to increase the pilot fuel mass.

Scharl et al. [28] studied HPDF combustion with ammonia and diesel in a rapid-compression-expansion-machine (RCEM). Different spray configurations and pilot amount, duration and timing were investigated by examining the heat release. They got successful combustion with pilot energy fractions as low as 3.2 %. It was observed that when ammonia is injected before the pilot fuel is ignited, this negatively affects combustion and interactions between the sprays are not favourable. A strong wall quenching effect for early ammonia injections was encountered but likely reinforced as walls are cold in an RCEM compared to a real engine. A similar (and simplified) study with several injection timings and injector locations will be performed at the end of this thesis. The same authors also combustion and mixture formation characteristics of ammonia sprays in an optically accessible RCEM under engine conditions [14]. Ammonia was injected after diesel, and interacting sprays were used, as this was the most favourable from the paper above. This study concluded that ammonia spray flames are unstable under the conditions examined due to difficulties in achieving a high-quality fuel and air mixture. The observed combustion behaviour led to elevated levels of unburned ammonia, NO_x and N_2O emissions. To improve the combustion behaviour of ammonia sprays and to reduce emissions, post-injections of diesel (two diesel injections) and fuel preheating were suggested.

Li et al. [27] conducted a numerical study comparing the HPDF approach with port injection of ammonia. This was based on a four-stroke diesel engine with a bore of 95 mm. In the study, pilot fuel injection was prior to ammonia injection, and different injector configurations and ratios of ammonia to diesel fuel were considered. The HPDF approach was found to reduce unburned NH_3, NO_x and GHG emissions compared to the LPDF approach and achieve a similar thermal efficiency as pure diesel, with a significant reduction in GHG. However, the highest thermal efficiency was found for the LPDF mode due to reduced cooling. During the study, stable operation with 97% energy from ammonia was achieved, and the nozzle configurations with the most interactions between the different fuel sprays were considered best. The same authors also conducted a similar study on a low-speed two-stroke marine engine [7]. Low-speed engines have more time for the fuel to burn, which is particularly favourable for ammonia due to its low burning velocity. For the HPDF case effect of injector arrangement, energy fraction of ammonia, pilot fuel injection timing, excess air ratio and engine load on engine performance were considered. The results showed that the configurations with the most interactions between fuel sprays resulted in the lowest levels of unburned ammonia. Additionally, advancing the diesel injection decreased and increased NH_3 and NO_x emissions, respectively.

To summarize this section: Late ammonia injection, close to diesel injection, is most promising as premixed combustion of ammonia and air suffers from high unburned ammonia and NO_x emissions. The most considered is injecting the more reactive pilot fuel first. Spray interactions between the pilot and main fuel are important for the combustion process and can have different effects on the combustion depending on the injection timing of the main fuel [28]. From a modelling point of view, high pressures are expected, meaning that ammonia is subcooled with fuel at room temperature. If fuel is preheated as suggested by Scharl et al. [14] and Frankl [29], or elevated from the heating of the engine, flash boiling could occur. In the engine considered by Lewandowski et al. [26], the ammonia is subcooled if injected after -40.5 CAD to TDC given a fuel temperature of 20°C. With a fuel temperature of 80°C the fuel is subcooled if injected after -8 CAD, which is after the diesel injection at -15 CAD. Modelling sprays with $\frac{P_a}{P_s} < 1$ could thus be useful in engineering applications.

3 Theory

This section provides an overview of the theory and background related to the topic. It includes some physics about ammonia and flash boiling, as well as the governing equations of the fluid flow and the theory behind the submodels applied to model the spray. The following sub-sections are based on the theory presented in the project thesis of the current author [42] and are extended to be more comprehensive.

3.1 Ammonia properties

This subsection compares selected characteristics and properties compared to diesel, the commonly used fuel in CI engines, and methanol. Methanol is used as a comparison as it is considered a promising alternative fuel. However, methanol contains carbon, and carbon neutral usage requires carbon capture and utilization. Also, the hydrogen content by weight is lower compared to hydrogen (12.5 % vs 17.6 % [5]).

Selected fuel properties are presented in Table 4. Diesel consists of several compounds, and the properties can thus vary. Ammonia has as seen the lowest boiling point and is a gas at ambient. When compared to diesel, ammonia has some extreme properties as a fuel. One aspect is the low energy density; thus, a larger amount of fuel is needed for the same energy output. Also, ammonia possesses an exceptionally high latent heat of evaporation. In addition, the burning properties also differ significantly, as seen from the flammability limits, flame temperature and autoignition temperature. Another characteristic that stands out is the stochiometric air demand, which is low compared to diesel. This makes up for some of the low energy density, and the energy content of the (stoichiometric) air/fuel mixture is similar to that of diesel [63]. However, it also makes it more susceptible to lean fuel/air mixtures that are hard to ignite [14].

Ammonia exhibits additionally unfavourable characteristics such as corrosive properties, which can affect materials such as copper, nickel, and plastics and is a problem for designing fuel handling systems. Moreover, it is considered toxic and classified as an extremely hazardous substance in many countries [15], which poses a significant risk, especially in enclosed spaces. However, it can be smelled in concentrations well below harmful limits.

Table 4: Selected fuel properties. Adopted from [14].

Parameter	Ammonia	Diesel	Methanol
LHV [MJ/kg]	18.8	~ 43.4	19.9
Latent heat of vaporization at 1 bar [kJ/kg]	1371	~ 256	1101
Flammability limit [vol%]	$16 - 25$	$\sim 0.6 - 6.5$	$6.7 - 36$
Adiabatic flame temperature [K]	2123	~ 2326	2143
Minimum auto-ignition temperature [K]	924	$\sim 527 - 558$	738
Boiling temperature [K]	240	$\sim 555 - 611$	338
Fuel density (at 293 K, 10 bar) [kg/m^3]	610	~ 870	792
Stoichiometric air demand [kg air/kg fuel]	6.05	$\sim$14.5	6.47

3.2 Flash boiling

Flash boiling is defined as the rapid transformation of a liquid into vapor when exposed to an environment with a pressure lower than its vapor pressure, illustrated in Figure 1. This phenomenon leads to the formation of vapor bubbles within the liquid. This process is similar to cavitation but comes from a different cause as flash boiling is caused thermodynamically, while cavitation is mechanically induced [30]. When a liquid exists in an environment where the pressure is below its saturation pressure, it is considered superheated and thermodynamically unstable. To reach equilibrium, the liquid undergoes flash boiling, a rapid transition into a vapor state.

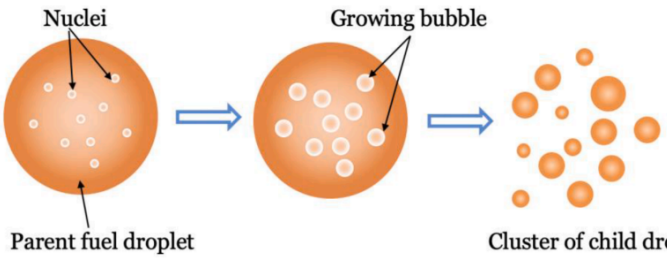

Figure 1: Bubbles grow inside droplet until it reaches a threshold and the bubbles burst, leading to many smaller droplets. Picture adopted from [58].

The flash boiling process can be divided into three separate processes as described by Sher et al. [64]: 1) bubble nucleation, 2) bubble growth and 3) two-phase flow, as illustrated in Figure 1. Bubble nucleation refers to the formation of tiny bubbles that can happen inside the liquid or at a surface interface. Following their formation, these small bubbles experience stages of either growth if stable or collapse. As described by Plesset et al. [65], Many factors influence bubbles' growth throughout the bubbles life. The max growth rate relies primarily on how superheated the surrounding liquid is. The rate is slow for small droplets due to the surface tension holding it back. As it grows larger, the influence of the surface tension declines, leading to an increase in growth. As bubbles grow, the surrounding liquid is cooled down due to evaporation resulting in lower vapor pressure and, thus, lower superheat. Then the growth rate is controlled by thermal diffusion and inertia. When pressure and temperature in the bubble are getting closer to ambient, growth slows down even further. For bubbles growing inside a liquid droplet, the maximum size of the bubbles is constrained due to surface tension, viscosity and droplet size. As the volume fraction of vapor to the total droplet volume increases, reaching a critical threshold, the droplets eventually burst. This "explosion" leads to a large increase in the number of droplets, as illustrated. In addition to internal factors, droplets can break due to external forces such as pressure waves.

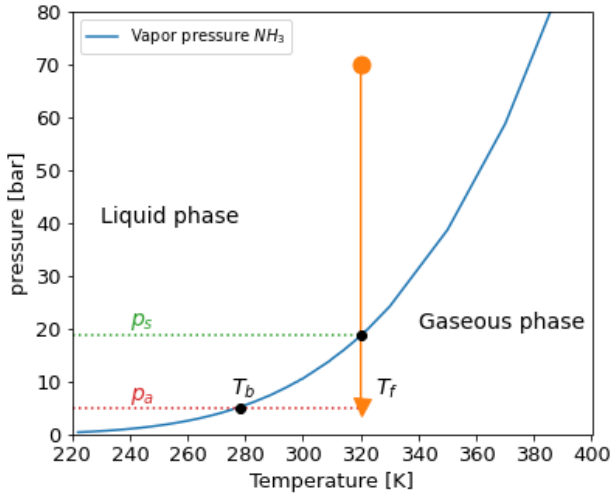

Figure 2: The arrow shows ambient pressure before and after injection under flash boiling conditions. In the end position, the superheat can be quantified with both pressure and temperature.

3.2.1 Superheat degree

To quantify the intensity in the flash boiling process which is crucial for describing spray formation under these conditions [32] the degree of superheat is useful. It is defined as:

$$T_f - T_b, \tag{1}$$

where T_f is the fuel temperature exiting the injector, and T_b is the boiling temperature at the ambient pressure. It could also be defined as the non-dimensional quantity

$$\frac{p_a}{p_s\left(T_f\right)}, \tag{2}$$

where p_a is ambient pressure and p_s is the saturation pressure at fuel temperature. As seen from these equations, the degree of superheat can be changed by altering ambient pressure or fuel temperature, and the ambient temperature is thus not a part of this equation. These two definitions are shown in Figure 2.

Xu et al. [32] studied flash boiling sprays for several conventional fuels (n-heptane, methanol, ethanol) using a multi-hole GDI injector and identified the degree of superheat as dominant for the spray behaviour and not fuel properties. Three different regimes with different behaviour were proposed, seen in Table 5 And correlations for spray penetration and with were proposed. In the transition region, plume width increases, and penetration length decreases as $\frac{p_a}{p_s}$ decreases. This is until $\frac{p_a}{p_s} = 0.3$, where the spray plumes collapse, creating a single body spray. Further decrease leads to the opposite effect. In the transition region, the width of the spray plume increases while the penetration length decreases as the ratio $\frac{p_a}{p_s}$. This trend continues until it reaches $\frac{p_a}{p_s} = 0.3$. At this point, the spray plumes collapse, resulting in a single body spray. Further decrease in the ratio has the opposite effect on penetration and width.

$p_a/p_s < 0.3$	Full flash boiling
$0.3 < p_a/p_s < 1$	Transition Region
$p_a/p_s > 1$	Non Flash-Boiling

Table 5: Different regimes based on degree of superheat [66].

3.3 Lagrangian-Eulerian multiphase flow

To model the multiphase flow of a spray, the Eulerian-Lagrangian modelling approach is applied, and this is done with the software Converge v3.0 [41]. Eulerian-Lagrangian multiphase flow modelling implies that the gas phase is modelled with an Eulerian solver, and the liquid phase is modelled with a Lagrangian solver. The liquid particles are hence tracked for their every move, i.e. their position, velocity etc., is calculated for each time step, whereas for the continuous gas phase, small fluid domains are fixed in space, and the flow properties are computed for this domain at every timestep. To emulate the physical effects of the liquid particles in the spray and to couple the two phases together, different submodels are applied to the discrete particles, e.g. for drag and evaporation. The dynamics of the Lagrangian and Eulerian phases and how they are implemented in the software will be described in the next chapter. How they are solved is presented in the next section. The theory is based on the Converge v3.0 manual [41].

3.3.1 Continuous phase

The continuous fluid flow, in this case consisting of air and evaporated ammonia, is governed by the Navier-stokes equations, which describe the conservation of mass, momentum and energy. To couple the liquid and vapor phases together, source terms are present in these equations to account for, e.g. evaporation of droplets and drag. For a compressible flow, the conversation equations written in Einstein summation notation are as follows. Conservation of mass is given by:

$$\frac{\partial \rho}{\partial t} + \frac{\partial(\rho u_i)}{\partial x_i} = S_{mass}, \tag{3}$$

where ρ is the density of the fluid, t is time, u_i is the velocity vector in the ith direction, and x_i is the position vector in the i th direction. S_{mass} source term for mass. The conservation of momentum is given by:

$$\frac{\partial \rho u_i}{\partial t} + \frac{\partial \rho u_i u_j}{\partial x_j} = -\frac{\partial P}{\partial x_i} + \frac{\partial \sigma_{ij}}{\partial x_j} + S_{mom,i}, \tag{4}$$

where P is the pressure and S_{mom} is the source term for momentum and can represent here the gravitational acceleration and coupling with the discrete phase. Three momentum equations are present, which can be seen as there is a vector in the numerator on the left hand. The term σ_{ij} is the viscous shear stress tensor and is defined as:

$$\sigma_{ij} = \mu \left(\frac{\partial u_i}{\partial x_j} + \frac{\partial u_j}{\partial x_i} - \frac{2}{3}\delta_{ij} \frac{\partial u_k}{\partial x_k} \right), \tag{5}$$

where μ is the dynamic viscosity and δ_{ij} is the Kronecker delta, which takes the value 1 if $i = j$ and 0 otherwise. The energy equation for compressible flow is given by

$$\frac{\partial \rho e}{\partial t} + \frac{\partial \rho e u_j}{\partial x_j} = -P\frac{\partial u_j}{\partial x_j} + \sigma ij \frac{\partial u_i}{\partial x_j} + \frac{\partial}{\partial x_i}\left(K_t \frac{\partial T}{\partial x_i} \right) + \frac{\partial}{\partial x_j}\left(\rho D_m \sum_m h_m \frac{\partial Y_m}{\partial x_j} \right) + S_{energy}. \tag{6}$$

Here e is the internal energy per unit mass, K_t is the turbulent thermal conductivity (when a turbulence model is applied), and T is the temperature. S_{energy} is the energy source term to account for turbulent dissipation. In addition to a pressure and viscous term also present in the momentum equation, energy transport terms for conduction and species diffusion are present. In the calculation of the species diffusion term, quantities for the different species present are needed, denoted by m. D_m, Y_m, and h_m are, respectively, mass diffusion constant, mass fraction and specific enthalpy of species m. As this is a compressible flow, an equation of state is needed to couple pressure, temperature and density. This is handled using the Redlich-Kwong equation, an empirical and algebraic relation with increased accuracy compared to the ideal gas law. To handle several species involved in the continuous phase, an additional equation for the transport of species is also needed. This is not included here for brevity. In addition to transport equations to handle the turbulent motions. These will be presented in the next section.

3.3.2 Turbulence modelling

Resolving all the motion in turbulent flows is demanding and impractical as turbulent eddies span several length scales. This is handled by solving the governing equations presented in the last section in a time-averaged manner, obtaining the (Reynolds averaged Navier-Stokes) RANS equation. This gives a simple description of turbulent flows, making it suitable for practical applications. This section explains how turbulence is modelled using the k-ϵ RNG model. The RANS equation is obtained by dividing the flow properties u_i and P into a mean and fluctuating part and time averaging the equations as shown for velocity:

$$u_i = \bar{u_i} + u_i', \tag{7}$$

where $\bar{u_i}$ is the time-averaged velocity and u_i' is the instantaneous fluctuating velocity. Density averaging (Favre averaging) is used to present the equation as shown for velocity to handle the varying density.

$$\tilde{u_i} = \frac{\overline{\rho u_i}}{\bar{\rho}}, \tag{8}$$

where $\bar{\rho}$ is the time-averaged density of the fluid. The compressible Reynolds-averaged Navier-Stokes equations can then be written as:

$$\frac{\partial \bar{\rho}}{\partial t} + \frac{\partial (\bar{\rho}\tilde{u_i})}{\partial x_i} = S_{mass} \tag{9}$$

for conservation of mass and for momentum:

$$\frac{\partial \bar{\rho}\tilde{u}_i}{\partial t} + \frac{\partial \bar{\rho}\tilde{u}_i\tilde{u}_j}{\partial x_j} = -\frac{\partial \bar{P}}{\partial x_i} + \frac{\partial \bar{\sigma_{ij}}}{\partial x_j} + \frac{\partial}{\partial x_j}\left(-\bar{\rho}\widetilde{u_i'u_j'}\right) + S_{mom,i} \tag{10}$$

Where $\bar{P}$ is the time-averaged pressure and $\bar{\sigma}_{ij}$ is the time-averaged viscous stress tensor. (also for energy and species not included here for brevity). Compared to Equation 4, a new term is added to the momentum equation:

$$\tau_{ij} = -\bar{\rho}\widetilde{u_i'u_j'}. \tag{11}$$

This term is known as the Reynold stress tensor, and is a second-order tensor yielding six unknown variables, Reynolds stresses. As no more equation is added, this leads to a closure problem. In k-ϵ models, the closure problem is handled by treating the Reynolds stresses as viscous stresses as done in the Navier-Stokes equations and linked to the mean flow field through the Boussinesq approximation. The same as how the viscous stresses in Equation 5 are linked to flow parameters:

$$\tau_{ij} = \mu_t\left(\frac{\partial \tilde{u_i}}{\partial x_j} + \frac{\partial \tilde{u_j}}{\partial x_i} - \frac{2}{3}\delta_{ij}\frac{\partial \tilde{u_k}}{\partial x_k}\right) - \frac{2}{3}\delta_{ij}\bar{\rho}k, \tag{12}$$

where is μ_t turbulent viscosity and k denotes the turbulent kinetic energy and is defined as:

$$k = \frac{1}{2}\widetilde{u_i'u_i'}. \tag{13}$$

In k-ϵ models the turbulent viscosity is defined as:

$$\mu_t = C_\mu \rho \frac{k^2}{\epsilon}, \tag{14}$$

where ϵ is the turbulent dissipation, and C_μ is a model constant. This way, the six unknown variable is reduced to two. Two additional transport equations are needed to solve for k and ϵ to get the eddy viscosity. Here the equations are shown with a neglected buoyancy effect. Transport equation for k is given by:

$$\frac{\partial \rho k}{\partial t} + \frac{\partial \rho u_i k}{\partial x_i} = \tau_{ij}\frac{\partial u_i}{\partial x_j} + \frac{\partial}{\partial x_j}\left[\left(\frac{\mu + \mu_t}{Pr_k}\right)\frac{\partial k}{\partial x_j}\right] - \rho\epsilon - \frac{C_s}{1.5}S_s. \tag{15}$$

And the transport equation for ϵ is:

$$\frac{\partial \rho \epsilon}{\partial t} + \frac{\partial \rho u_i \epsilon}{\partial x_i} = C_{\epsilon 1}\frac{\varepsilon}{k}\tau_{ij}\frac{\partial u_i}{\partial x_j} - C_{\varepsilon 2}\frac{\varepsilon^2}{k} + \frac{\partial}{\partial x_j}\left[\left(\frac{\mu + \mu_t}{\mathrm{Pr}_\varepsilon}\right)\frac{\partial \varepsilon}{\partial x_j}\right] + C_s S_s \frac{\epsilon}{k} - \rho R_\epsilon. \tag{16}$$

In these equations, Pr_k, Pr_ε, $C_{\varepsilon 1}$, $C_{\varepsilon 2}$ and C_s are model constants. The source term S_s occurs from interactions with discrete phase and is from work done by the turbulent eddies on droplets, i.e. negative term. The terms on the left hand side represent the convective transport. The terms on the right hand side represent 1) production, 2) diffusion, 3) dissipation and 4) source of k and ϵ, respectively. The difference between the standard and RNG model is the fifth term, R_ϵ, only present in the dissipation equation. This term is given by:

$$R_\epsilon = \frac{C_\mu \eta_3\left(1 - \frac{\eta}{\eta_0}\right)}{1 + \beta\eta^3}\frac{\epsilon^2}{k}, \tag{17}$$

where η_0 β, models constants, and η is the mean strain rate tensor. The Re-Normalisation Group (RNG) $k - \epsilon$ turbulence model [67]. This model uses the Re-Normalisation Group to attempt to account for more scales of motions. This makes this model suitable for in-cylinder flow [59] and is widely applied in engine simulations. The additional term, including strain, makes it better at handling rapid strain inflows (and swirling). However, it is less numerically stable than the conventional $k - \epsilon$ model.

3.3.3 Discrete phase modelling

The discrete phase consisting of liquid ammonia droplets is modelled as parcels which statistically represent several droplets with the same properties. This reduces the number of discrete particles needed to track and therefore cuts computational cost. The governing equation is solved for each individual parcel to obtain the velocity. The force on the droplet affected by drag and gravitational acceleration, g, is

$$F_{droplet} = C_D A_f \frac{\rho_g |U_{rel,i}|}{2} U_{rel,i} + \rho_l V_d g_i, \tag{18}$$

where C_D is the drag coefficient, A_f is the droplet frontal area, V_d is the droplet volume, and $U_{rel,i}$ is the relative instantaneous velocity to the air around the droplet given by:

$$U_{rel,i} = \bar{u_i} + u_i' - v_i, \tag{19}$$

where v_i is the instantaneous droplet velocity. u_i', the instantaneous fluctuating velocity of the continuous phase is not included in the RANS equations and must be modelled with a turbulent dispersion model. Applying newtons second law on the force equation and by assuming that the droplets are spherical for simplicity, the governing equations of the parcels can be written as:

$$\frac{dv_i}{dt} = \frac{3}{8} \frac{\rho_g}{\rho_l} C_D \frac{|U_{rel,i}|}{r_d} U_{rel,i} + g_i, \tag{20}$$

and

$$\frac{dx_{p,i}}{dt} = v_i, \tag{21}$$

for acceleration and velocity, respectively. Where ρ_l and ρ_l are the density of the liquid and the surrounding air, respectively, and r_d is the droplet's radius. From these equations, the velocity and position of the parcels are described. C_d is the drag coefficient, and models for this one will be described in the next section. Different discrete phase submodels, presented in Figure 3, used in the simulations are explained in the following section. Drop and wall interactions are not considered here, and thus models for this are not included.

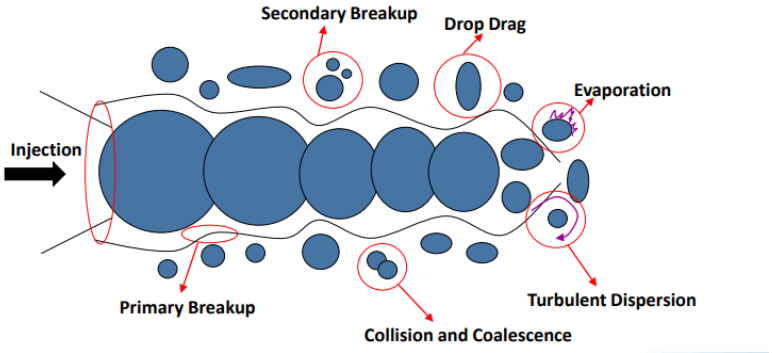

Figure 3: Spray development processes. Adopted from [41].

3.3.4 Model for drop drag

The model for drop drag is important for accurately reproducing spray behaviour. In the particle equation of motion, both velocity of the continuous phase and discrete is present in addition to the drag coefficient. Thus this is important for coupling the two phases. The Dynamic droplet drag model takes the basis in the relations for drag on a rigid sphere by Liu et al. [68].

$$C_{D,sphere} = \begin{cases} 0.424, & Re_{d,rel} > 1000. \\ \frac{24}{Re}\left(1 + \frac{1}{6}Re^{\frac{2}{3}})\right), & Re_{d,rel} < 1000. \end{cases} \tag{22}$$

In this equation, $Re_{D,rel}$ is the droplet Reynolds number based on the relative velocity between droplets and the continuous phase. The Reynolds number is given by:

$$Re_{d,rel} = \frac{\rho_l 2 r_d |U_{rel}|}{\mu_l}, \tag{23}$$

where μ_l is the dynamic viscosity of the liquid. The assumption that droplets are spherical leads to underpredictions of drag. The Dynamic droplet drag model takes the distortion of the droplets into account, and the coefficient is calculated as follows:

$$C_D = C_{D,sphere}\left(1 + 2.632y\right), \tag{24}$$

where y is a distortion parameter between 0 and 1, with the value of 0 meaning no distortion and drag as a sphere, and 1 gives drag as a disc. The drop distortion is calculated based on the Taylor analogy breakup model [62], which is based on the damped spring-mass analogy. Where the drag is the external force, the surface tension is the spring force (restoring), and the viscosity is the cause of the dampening. The equation for y is mainly dependent on the Weber number, which represents the ratio of inertia to surface tension, meaning that larger droplets and faster droplets will have increased distortion and thus higher C_D.

In summary, from equation 22, it can be seen that for $Re_{d,rel} < 1000$, i.e. small droplets and/or slow droplets, the $C_{D,sphere}$ is higher, whereas for higher Reynolds numbers ($Re_{d,rel} > 1000$), C_{d_sphere} is constant, but droplets with high inertia get increased C_D due to distortion. Equation 20, shows that larger droplets have lower acceleration given the same C_D. This means that, for droplets with the same velocity, small droplets will thus not travel as far due to less inertia (and possibly higher C_D). Larger droplets experience a reduced acceleration due to more inertia, but as C_D increases from distortion, this affects the droplet acceleration in the opposite direction, and there is a battle of effects on the acceleration of the droplet.

3.3.5 Turbulent dispersion

RANS only solves for the mean flow properties, and the instantaneous fluctuating u_i' in Equation 19, to account for the effect of the turbulent eddies on the droplets needs to be modelled. In the O'rourke approach by Amsten et al. [69], u_i is stochastically determined. In this model, the component of the vector u_i' is set to follow a Gaussian distribution with probability density function given by:

$$G(u_i') = \frac{1}{\sigma\sqrt{2\pi}} e^{-\frac{-(u_i')^2}{2\sigma''^2}}, \tag{25}$$

where the variance is given by $\sigma''^2 = \frac{2}{3}k$. By creating random numbers and the cumulative version of Equation 25, values for u_i' are obtained in all three directions. This is done for each turbulent correlation time, which is either the eddy breakup time or the time needed for a droplet to travel the distance of the turbulent length scale, depending on which is shortest. The eddy turnover time is defined as $\frac{k}{\epsilon}$, and the time for the droplet to travel across an eddy is given by the turbulent length scale divvied by the relative velocity, $C_\mu^{\frac{3}{4}} \frac{k^{\frac{2}{3}}}{\epsilon} \frac{1}{|U_{rel,i}|}$.

u_i' appears in the source terms in the k transport equation due to when the eddies perform work on the parcels, the flow gets less turbulent.

3.3.6 Model for collisions

Droplet interactions are another spray development process that needs to be accounted for. Collisions result in changes in size, velocities and number of parcels. In the No time counter approach (NTC) by Schmidt et al. [70], interactions between parcels in the same computational cell are randomly determined. In this model, the computational cost is proportional to the number of parcels present, as opposed to many collision models where the computational cost grows exponentially. This model can be set up with different collision outcomes. With the O'Rourke collision outcome, droplet interactions lead to grazing collisions or coalescence. Grazing collisions is a way of calculating new parcel velocities based on energy conservation and momentum, including some fraction of energy and angular momentum loss. If set up with Post collision outcomes [71], the two additional outcomes stretching separation and reflective separation, are added. The collision model can be used with adaptive collision mesh to get more accurate results, as collision models are highly grid sensitive. Without collision mesh, parcels only within the same cells can interact, resulting in unrealistic behaviour and pattern from these effects.

3.3.7 Model for injection

Modelling the injection is a crucial aspect. This decides the size and velocity of initial parcels, in addition to how they are injected. The mass flow and a discharge coefficient, C_d, must be specified to calculate initial droplet velocity. To account for the varying mass flow occurring in a real injector, a rate-shape profile can be specified in addition to the mean mass flow given by total mass and injection duration. An instantaneous ideal velocity, V, can be calculated using liquid density and injector geometry. The initial parcel velocity is obtained by dividing this by a contraction coefficient which is given by:

$$C_a = \frac{C_d}{C_v}, \tag{26}$$

where C_v is the velocity coefficient, this can be calculated based on a correlation based on the instantaneous injection pressure [41] or set to a constant value. For a constant mass flow, C_v is a constant, but as the relation between C_a and C_d is not proportional, a correlation can be used instead when mass flow is varying. Lowering the C_d will thus increase initial parcel velocity for the same mass flow through the injector. C_d is a relation between the theoretical and actual fluid flow and is defined as:

$$C_d = \frac{\dot{m}}{\dot{m_{ideal}}} = \frac{\dot{m}}{A\sqrt{2\Delta P \rho_f}}, \tag{27}$$

where A is the total surface area of the nozzle holes, ρ_f is the density of the fluid, and ΔP is the difference between injection pressure and ambient pressure in the chamber.

Some of the required parameters for calculating the initial parcel velocity are often unknown. Then the spray rate calculator in Converge can be used. This calculates the injection pressure by:

$$P_{inj} = \frac{1}{2}\rho_l \left(\frac{V}{C_d}\right)^2, \tag{28}$$

e.g. if injected mass or C_d is unknown, but injection pressure is known. The initial size distribution exiting each nozzle also needs to be set. This can be done either by the Blob injection method or with a specified droplet distribution. With the blob injection method, the initial droplet size is based on the contracted nozzle area, i.e. droplet diameter is equal to $\sqrt{C_a}$ multiplied by nozzle diameter. Alternatively, it can be set by a distribution, then a specified Sauter mean diameter (Eq. 45) and distribution needs to be specified. In Converge, the Rosin-Rammler distribution and Chi-squared distribution are available. For the Rosin-Rammler distribution, a shape parameter

must also be specified. With different initial droplet sizes, the number of droplets per parcel also changes to ensure mass conservation.

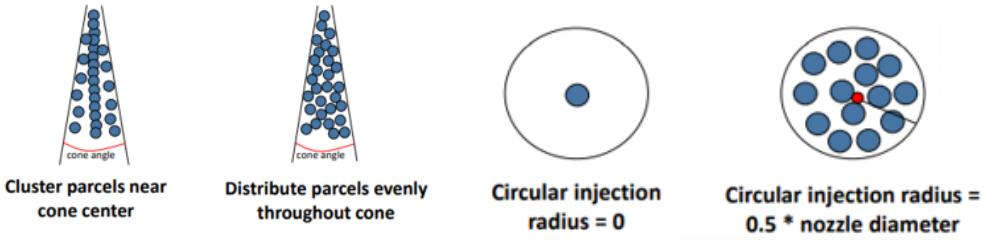

Figure 4: Left: distribution of parcels in the cone. Right: Location of which parcels are injected from. Picture adopted from [41].

How the parcels are injected also needs to be specified. The cone angle, seen as the thickness of a single plume in Figure 4, is to determine the angular spread of injected parcels. In this cone, the distribution also needs to be specified, and it can be set to either clustered or evenly distributed. When the clustered distribution is applied, more parcels are set along the plume's centre axis, whereas for evenly distributed, the placements are more evenly, and more spread of parcels is the outcome. In addition to this, where parcels should be injected from in the nozzle must be specified. The parameter circular injection radius determines this. When the value is set to 0, all parcels are injected from the center of the nozzle. Contrarily, when the value is set to the nozzle radius, parcels are injected from across the entire nozzle area.

3.3.8 Evaporation and flash boiling

Evaporation model

To model the evaporation process of the liquid phase droplet, the Frossling evaporation model [69] is chosen. This model gives an expression for the rate of change of droplet radius, r_0:

$$\frac{dr_0}{dt} = -\frac{\alpha_{spray}\rho_g D}{2\rho_l r_0} B_d Sh_d, \tag{29}$$

where α_{spray} is a scaling factor for mass transfer, D is the mass diffusivity of liquid vapor in air, and Sh_d is the Sherwood number. In Converge, D is calculated from a relation with two empirical constants, D_0 and n_0. The Sherwood number is a dimensionless parameter representing the ratio of the convective to diffusive mass transfer (As Nusselt number but with mass instead of heat). This here calculated from a correlation including relative droplet Reynolds number ($Re_{d,rel}$) and Schmidt number (Sc):

$$Sh_d = (2 + 0.6 * Re_{d,rel}^{\frac{1}{2}} Sc^{\frac{1}{3}}) \frac{\ln 1 + B_d}{B_d}, \tag{30}$$

where B_d is the Spalding transfer number representing vapor mass fraction on the droplet surface and is given by:

$$B_d = \frac{Y_1^* - Y^1}{1 - Y_1^*}, \tag{31}$$

where Y_1^* and Y^1 are the vapor mass fraction on the droplet surface and the vapor mass fraction away from the droplet, respectively. The parameters which are included in the Frossling correlation ($Re_{d,rel}$, Sc and D) are calculated at the temperature $\frac{1}{3}T_{gas} + \frac{2}{3}T_d$, where both liquid temperature of the droplet and surrounding gas temperature is included. From Equation 29, it can be seen that a smaller droplet evaporates faster if the rest of the parameters is the same. Also, the Schmidt

number is increasing for smaller droplets as this is inversely proportional to the droplet diameter. For calculating the droplet temperature, two different approaches can be applied:

- Uniform temperature model - Same temperature for the entire droplet.
- Discretized temperature model - Temperature varies by radius.

With the uniform temperature model, the temperature of the droplet is obtained by solving two ordinary differential equations. For the discretized temperature model, a 1D spherical partial differential equation (heat equation) must be solved to get the temperature for droplets larger than a specified size. This additional PDE significantly increases the computational cost needed but results in a more accurate temperature for larger droplets. The simplified uniform temperature model tends to underpredict temperature for larger droplets [41], leading to an underprediction of evaporation rate.

For the uniform droplet temperature model conservation of energy equation for a droplet can be expressed as:

$$hA_d(T_{gas} - T_d) = m_d Cp \frac{dT_d}{dt} - \frac{dm_d}{dt} H_{vap}. \tag{32}$$

Given the assumption that all heat transferred to the droplet leads to either an increase in temperature or the evaporation of liquid mass. C_p is the specific heat coefficient of the liquid, H_{vap} is the latent heat of vaporization at droplet temperature, A_d is the droplet surface area and h is the heat transfer coefficient based on Ranz-Marshall correlation [72] and is based on the ratio of convective to conductive heat transfer (Nusselt number).

Flash boiling model

For superheated liquid the evaporation is calculated with the model by Price et al. [49]. In Converge, this model takes basis in the Frossling correlation but expands it by accounting for the enhanced phase change expected under these conditions. The Frossling equation is based on heat transfer from air to the droplet, which for subcooled liquid is considered adequate [59]. For superheated droplets, the inside of the liquid has a higher temperature than the surface, and thus the heat transfer from within also has to be accounted for. In this model, the surface temperature is set equal to the saturation temperature of the ambient pressure. The Price model increases the phase change by adding a superheat term to the evaporation equation. The total evaporation, here shown as the rate of change of droplet mass, is then given by:

$$\frac{dm_d}{dt} = \frac{dm_{sh}}{dt} + \frac{dm_{sc}}{dt} \tag{33}$$

The subcooled contribution to the evaporation, $\frac{dm_{sc}}{dt}$, is given by the Frossling correlation, Equation 29 (by rewriting the equation using the volume and density of a liquid) and the superheated evaporation term is given by:

$$\frac{dm_{sh}}{dt} = \frac{4\alpha r_d^2 (T_d - T_{b)}}{H_{vap}}, \tag{34}$$

where α, the transfer coefficient, is determined by an empirical relation established by Adachi et al. [48] presented in Equation 35.

$$\alpha = \begin{cases} \beta \cdot 760 \left(T_d - T_b\right)^{0.26} & \text{when } 0 \leq (T_d - T_b) \leq 5 \\ \beta \cdot 27 \left(T_d - T_b\right)^{2.33} & \text{when } 5 \leq (T_d - T_b) \leq 25 \\ \beta \cdot 13800 \left(T_d - T_b\right)^{0.39} & \text{when } (T_d - T_b) \geq 25 \end{cases} \tag{35}$$

The heat transfer can be adjusted by modifying the user-defined parameter β. The degree of superheat, expressed here as the temperature difference between the droplet and the boiling temperature, $T_d - T_b$, is the driving force behind this evaporation term. To include the reduced droplet

size resulting from flash boiling, the model can be extended by incorporating size reduction. This can be done based on the assumption of constant liquid density and the droplet mass change rate from Equation 36.

$$\frac{dr_d}{dt} = \frac{\lambda}{4\pi\rho_l r_d^2}\frac{dm_d}{dt} \tag{36}$$

The model scaling factor, denoted by λ, is utilized to either amplify or reduce drop atomization. The flash boiling evaporation process can thus be scaled with the constants β and λ.

Conventional boiling model

In addition to the evaporation model, a conventional droplet boiling model is available in the software. This model uses the Frossling relation until the droplet reaches boiling temperature at a given pressure. When droplet temperature reaches boiling temperature, T_b, the temperature remains constant at the and change in size is given by:

$$\frac{dr_o}{dt} = \frac{K_\infty}{\rho_l C_{p_\infty} r_0}\left(1 + 0.23\sqrt{Re_{d,rel}}\right)\ln\left(1 + \frac{C_{p,\infty}\left(T_{gas} - T_b\right)}{H_{vap}}\right), \tag{37}$$

where K_∞ and $C_{p,\infty}$ are the surrounding gas phase's conductivity and specific heat capacity, respectively. As seen in equation 37, the change in size is in large dependent on $T_{gas} - T_b$ and therefore, the rate of change is slow when the surrounding air temperature is approaching saturation temperature.

Flash boiling and conventional boiling are processes with rapid phase change, but they result from different causes and have different behaviour. The main difference between the two is the conditions where they occur. Conventional boiling happens when the temperature of a liquid exceeds its saturation temperature at (nearly) constant pressure. Flash boiling, on the other hand, occurs if a liquid undergoes suddenly is exposed to pressure conditions under its saturation pressure while maintaining a nearly constant temperature. In flash boiling, the heat transfer comes mainly from within the droplet itself, while conventional boiling heat transfer is from the surrounding air. The timescale for flash boiling is also much smaller, and the effects are therefore also more dramatic.

The main difference between the conventional boiling model and the Price model is the temperatures considered in calculations. In the Price model, $T_d - T_b$ is used (droplet - boiling) in the superheated term in addition to the Frossling correlation. The conventional boiling, however, the model relies on $T_{gas} - T_b$ (ambient - boiling).

3.3.9 Models for breakup

The Kelvin-Helmholtz Rayleigh Taylor (KH-RT) breakup model is applied to model the droplet breakup. This hybrid model utilises both Kelvin-Helmholtz (KH) and Rayleigh Taylor (RT) models to model the complex droplet breakup. These models cause droplets to break up due to different instabilities. This section will not address how the waves causing the instabilities are calculated. The focus here is on the various configurations in which the model can be set up and how the different model parameters affect the breakup process.

The Kelvin-Helmholtz Breakup Model [73] based on liquid jet stability analysis. This model is based on the fact that breakup is proportional to the wavelength of the fastest growing unstable surface wave, Λ_{KH}. Starting out with a droplet of size r_p, this will, after breakup, result in child droplets with radius r_c given by:

$$r_c = B_0\Lambda_{KH}, \tag{38}$$

where B_0 is a model size constant. As a result of the breakup, the parent droplet experience

reduction in mass. The rate of change in the radius parent droplet size is given by

$$\frac{dr_p}{dt} = -\frac{r_p - r_c}{\tau_{KH}}. \tag{39}$$

where, τ_{KH}, is the breakup time defined as:

$$\tau_{KH} = \frac{3.726 B_1 r_p}{\Lambda_{KH}\Omega_{KH}}. \tag{40}$$

Ω_{KH} is the frequency of the most unstable KH wave, i.e. wave with the maximum growth rate and B_1 is a model time constant. This constant is related to disturbances at the start of the jet and varies with the injector. The model can be run both by adding the child droplets to the computation and not. The child droplets get a velocity v_n normal to the parent droplets path given by:

$$v_n = C_1 \Lambda_{KH}\Omega_{KH}, \tag{41}$$

where C_1 is a model velocity constant. Only running the KH model in Converge without the creation of child parcels is similar to the Reitz and Diwakar model [60]. When not creating new child droplets, the number of droplets in the parent parcels is adjusted to achieve conservation of mass.

In the Rayleigh-Taylor breakup model, the instabilities arise due to the drag force acting on the droplets, resulting in significant acceleration (Eq. 20). After the RT breakup, the size of the droplets are as for the KH model proportional to the fastest growing wavelength, Λ_{RT}, but the cause of the waves are different. The radii of the new droplets are thus given by:

$$r_c = C_{RT}\Lambda_{RT}. \tag{42}$$

The breakup time, τ_{RT}, is in this model defined as:

$$\tau_{RT} = \frac{C_I}{\Omega_{RT}}, \tag{43}$$

where Ω_{RT} are the frequency of the fastest growing RT instability. C_{RT} and C_I are the model size and time constant, respectively, as described by Xin et al. [74]. For calculating the frequency and wavelength, an extended version of the standard RT model is applied which also includes viscosity [75].

When using the two breakup models together, a breakup length from the nozzle, L_b, is defined where only the KH instabilities are causing the breakup, as shown in Figure 5. This length is given by:

$$L_b = C_{bl}\sqrt{\frac{\rho_l}{\rho_g}} d_0, \tag{44}$$

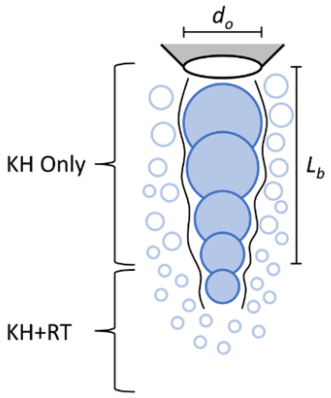

Figure 5: Breakup mechanisms in different regimes of spray in the combined KH-RT breakup model. Picture adopted from [41].

where C_{bl} is a model length constant. Outside of this length, breakup is decided by competing effects from both model, i.e. in the combined model KH is causing the primary and RT the secondary breakup of the droplets. The thought behind this is that liquid close to the nozzle is part of a liquid core and, thus not as affected by the drag acceleration which is causing the RT instabilities. For sprays with high pressure and velocities, where the inertia is dominating (typical diesel sprays), the KH equations can be written as a breakup length, and to keep these two lengths similar, C_{bl} needs to be set equal to $\frac{B1}{2}$ [76]. Applying both breakup mechanisms to the entire spray can be achieved by setting the constant for the breakup length, C_{bl}, to zero. The KH-RT model can also be run in a modified version without a breakup length.

Based on the equations mentioned earlier, breakup time is controlled by the model constants B_1 and C_I. And the size of the resulting droplets can be changed by the constants B_0 and C_{RT}. In the results, the conventional model is employed with the RT length constant C_{bl} set to zero, which software recommends for both flash and non-flash conditions with GDI injection systems.

3.4 Combustion phases in direct injection compression ignition engine

The combustion process in a direct injection compression ignition (DICI) engine consists of several distinct phases. These phases can be identified from the heat release rate (HRR) chart as shown in Figure 6. The time (x-axis) is in Crank angle degrees (CAD), Where 0 corresponds to the piston in the top position, top dead center (TDC). As seen from the figure, there are four main phases. The first phase is the ignition delay, which occurs between the start of injection (SOI) and actual combustion/ignition. After this, the premixed combustion phase takes place. In this phase, the combustible fuel/air mixture that was premixed during the ignition delay ignites and rapidly combusts. This phase is characterized by a high peak in HRR and short duration. The next phase is mixing controlled combustion. In this phase, the HRR depends on the fuel/air mixture that gets available for burning continuously. This phase is influenced by processes such as fuel atomization, vaporization, and the mixing of fuel vapor with air. A peak in HRR also characterizes this phase but with a smaller magnitude and extended time period compared to the premixed combustion phase. The last phase is the late combustion phase, which occurs after the main combustion phases. In this phase, there is a slower release of heat from fuel that has not yet burned completely. It includes unburned fuel, fuel present in combustion products, and the mixing of these components. In this late phase, the temperature is lower, and thus also, the chemical reactions are slower [21].

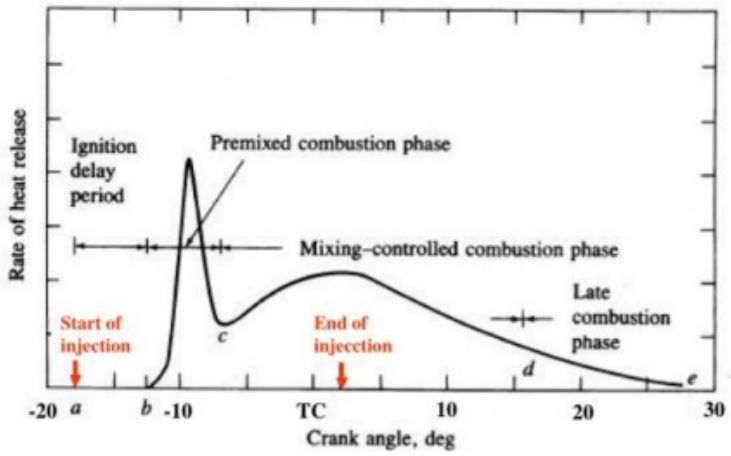

Figure 6: The different phases in a DICI combustion process. Picture adopted from [21].

4 Spray in constant volume chamber

This section presents numerical modelling of liquid ammonia spray from a GDI injector into a constant volume chamber. This was done using the commercial software Converge [41]. To begin with, an investigation was conducted on flash boiling spray, covering aspects not previously addressed in the project thesis [42]. In simulated sprays from the project thesis, penetration lengths were generally underpredicted. Understanding the underlying causes for this and finding a setup in better agreement with the experiment for these conditions are the objectives for this part. The analysis places the main emphasis on various injection parameters, which were found to significantly impact spray behaviour. In the second part, simulations are conducted for six different pressure conditions, with and without the flash boiling. The main aim of this part is to replicate penetration length and shape from the experimental sprays.

The section starts with methodology; how the experimental data is obtained, the simulation conditions considered and how data will be analysed. Following that, the simulation setups and the assumptions and simplifications in the model are presented. Next, the results and discussions are presented separately for each part. The introductory segment of the results sections includes the model setup for the discrete phase as they differ for the two parts.

4.1 Experimental case description

The experimental conditions considered and how they are obtained are presented here. Additionally, the methodology used to compare numerical simulations with the experimental data is presented.

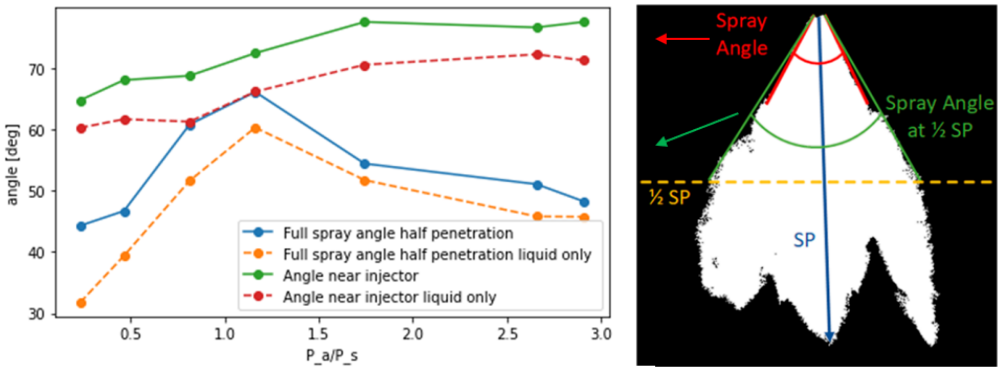

Figure 7: Left: Spray angles from experiment for various conditions measured 2 ms after the start of injection. Right: how angles are measured in the experiment. The picture on the right-hand side is adopted from [31].

4.1.1 Experiment

The experiments by Pelé et al. [31] from 2021 are used both for model input and validation. In this experiment, the liquid spray was injected into a constant volume chamber using a multi-hole Bosch GDI injector. The injector is compromised of 7 holes of 150 µm diameter and counterbore diameter, step diameter, of 365 µm. The chamber was pressurised with an air compressor and heated through wall resistance to reach desired conditions. The ammonia used for injecting was pressurised up to 120 bar and assumed to be 293 K when injected.

To examine the spray, Schlieren imaging technique were applied, making it possible to distinguish between air and fuel. By adjusting the light intensity, the liquid and vapor spray phases could both be tracked, obtaining both liquid and vapor penetration lengths. From these same pictures, spray angles near the injector and at half penetration length were measured for different time steps, as seen in Figure 7 for the two distinct phases. To see how angles evolve in time. Some microscopic

characteristics were also considered as droplet sizes were measured using a Malvern droplet size analyser at five different locations in the spray. More details about the experimental setup and post-processing of the data can be found in [31].

4.1.2 Conditions considered

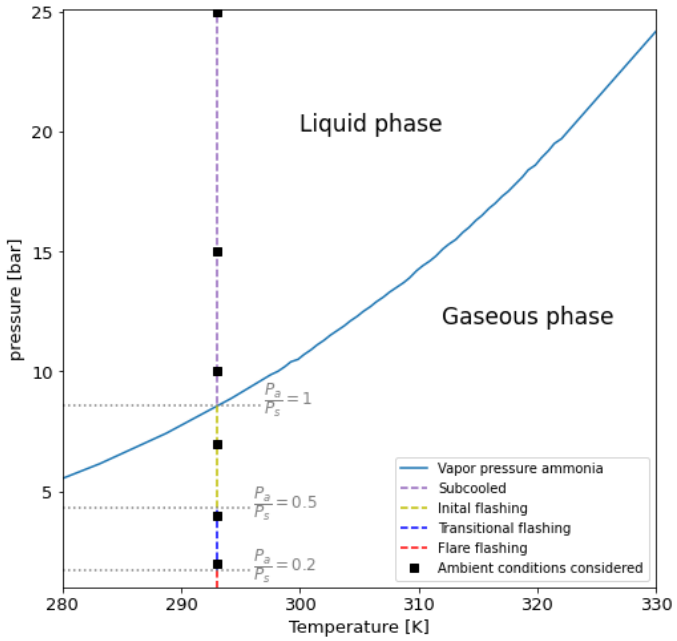

Figure 8: The ambient pressures considered are shown together with the different flashing regions for expected behaviour [33]. The vertical line represents the fuel temperature. Ammonia properties from [6].

The conditions considered for reconstruction were all for the chamber without any heating. Higher ambient temperatures and the same degree of superheat would have been interesting. However, this was not considered in the experiment as ambient density was kept constant when adjusting for different chamber temperatures, altering the degree of superheat. The ambient pressures that were considered can be seen in Figure 8 and varies from 2 to 25 bar. The vertical line represents the fuel temperature. Given a saturation pressure of 8.6 bar [6], this corresponds to superheat degree from 0.23 to 2.91. Based on the regions for flash boiling proposed by Li et al. [33], two conditions are in the transitional flashing region where the case with ambient conditions of 2 bar, used in the parametric study, is bordering the flare flash region. The third flashing condition considered is in the initial flashing region, approaching critical flashing. The subcooled cases consist of one close to critical flashing, expected to behave similarly to the pressure case below, and two highly subcooled conditions. This is based on a liquid fuel temperature of 293 K. If the actual fuel temperature were lower, e.g. due to cooling due to phase change in the nozzle, the line would move to the left, making the same ambient conditions less superheated. The opposite would be the case if the temperature were underestimated.

Parameter	
Injection pressure	120 bar
Fuel temperature	293 K
Injection time	4.0 ms
Mass injected	40 mg
Ambient temperature	293 K

Table 6: Details of spray experiment setup.

Injection duration is here set to 4 ms. The injected mass is set to 40 mg for all conditions based on a lack of experimental values. 39.93 mg was presented in the presentation in Cardiff [37] where simualted ambient pressure were 2 and 15 bar. Pelé [31], author of the experimental paper, was also mentioned as an author there. What condition(s) this measurement is based on is not known. Actual injected mass for the higher ambient pressures probably differs from this and will be discussed. A summary of the experimental spray conditions can be seen in Table 6.

4.1.3 Comparing data

Validation and sensitivity are essential aspects of any numerical analysis. This thesis is mainly about replicating sprays from an experiment, and how these are compared is crucial. The methods used to compare the simulation results with experimental data are presented in this subsection, and assumptions and simplifications will be presented and discussed. Also, uncertainty when it comes to measurements will be discussed. Obtained data is not only for comparing with the experiment but also for examining the effect of parameters and explaining the physics behind the behaviour.

Penetration length

Both liquid and vapor penetration lengths are of interest. In the simulations, the liquid penetration length, LPL, is calculated as the distance from the nozzle where a given percentage of the total liquid mass can be found within. 95% of the liquid mass is set to the default value in the software. However, what value is closest to the measuring technique is unknown, and changing the definition can significantly affect the reported length, especially for superheated conditions. What value has been used in literature is usually not included. Some do, e.g. Duronio [30] uses 99%. Therefore, both 95% and 99% are used when comparing simulation to experimental data. Vapor penetration length, VPL, is in the software defined as the distance to the computational cell where the vapor mass fraction of ammonia is above a pre-defined limit. This is found to have a less significant effect on the length [42], and the default fraction of 0.001 is applied here. These lengths are calculated separately for each nozzle. When presented, they are averaged over the seven nozzles. For the experimental condition of 2 bar, the wall is hit after approximately 2.5 ms, and penetration lengths are only comparable up to this point.

Furthermore, the measured length by software is the total length travelled and not the length along the axis of the jet, which is the length measured from the experiment. For the lower pressures considered, the narrowing effect of the spray due to plume interactions makes droplets travel mainly in the spray axis direction. This narrowing effect is not as pronounced for the higher ambient pressures, meaning that the reported penetration lengths are slightly overpredicted for these conditions.

Shape

The shape of the sprays will be assessed both qualitatively and quantitatively. When available, sprays from the simulations are compared to Schlieren images of the liquid phase of the spray. The focus is on comparing main spray morphology features, such as the evolution of spray angle along the spray axis as illustrated in Figure 9. This can tell about the interactions between plumes. Also, other main features, such as vorticities to tell about radial velocity, are of interest. In highly superheated conditions, the spray is anticipated to collapse into a unified body with a distinctive bell shape with vortices at the tip. The number of parcels present at locations in the spray can provide insights into the evaporation process as well.

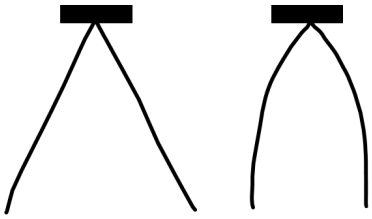

Figure 9: Different spray body shapes. Constant spray angle is presented on the left and decrease in spray angle on the right.

When looking at multiple conditions in the second result part, measurements of pictures of parcels will be compared to angles for the liquid phase from the experiment. The comparison is made 2 ms after the start of the injection. As illustrated in Figure 10, the spray angle is measured at half penetration length. Measuring from a picture like this gives poor accuracy as it is susceptible to where the outer spray is defined. Also, the perspective is not comparable as nozzles are not perpendicular to the plane but are instead pointing slightly outwards. It is still considered good enough to capture the trends. Qualitative and quantitative measurements from the simulation are based on pictures of liquid parcels. The parcels represent several droplets, and how many can't be seen from the picture. Also, the size of droplets is not included, i.e. in reality, the droplets near the nozzle are much larger. Using these pictures is still assessed as well enough to report the main spray characteristic.

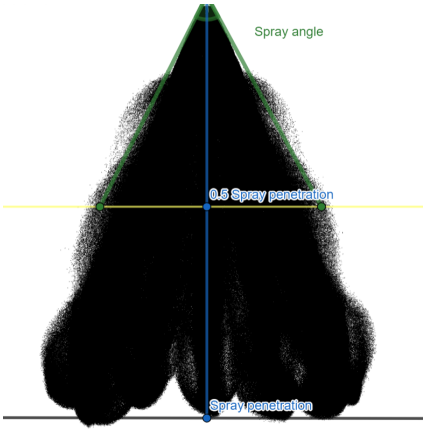

Figure 10: Schematic of spray angle at half penetration length. How spray angle will be measured and compared to experiment in the second part.

Droplet size

The main focus is on the main features of Penetration length and shape when replicating spray. Still, also droplet size is used for comparing data and assessing the effect of parameters. The Sauter mean diameter (SMD, d_{32}) is used to assess and compare spherical droplet sizes. This is especially useful in applications where surface area is important, e.g. combustion physics. The Sauter mean diameter is defined as a mean diameter of a sphere with the same ratio of volume to surface area as the entire collection. In other words, the cube of the volume mean diameter divided by the square of the surface mean diameter. In Converge, the SMD is calculated as in equation 45 [41].

$$d_{32} = \frac{\sum_{i=1}^{N_{tot}} N_i d_i^3}{\sum_{i=1}^{N_{tot}} N_i d_i^2}, \tag{45}$$

where N_{tot} is the total number of parcels, N_i is the number of droplets in parcel i and d_i is the diameter of droplets in parcel i. When comparing droplet sizes from simulations to experimental

values, experimental values from the middle of the spray are compared to droplets in the plane located 40 mm from the injector tip, as shown in figure 11. How comparable these are is not known, but this is considered good enough for comparing the order of magnitude and looking at the trend over various conditions. From the experimental conditions with ambient pressures of 2 bar and 20 °C (can be seen in [38]). The droplet sizes observed in the middle and closest locations to the injector exhibit similar sizes, while the droplets located farther away have a smaller Sauter Mean Diameter (SMD). In other words, the droplets at the outskirts are larger than those in the middle. Comparing the droplets in the outer regions to the middle location would then result in overestimating the SMDs. This trend is not as clear for the higher pressure of 15 bar. When comparing different parameters the SMD of the entire spray is also considered.

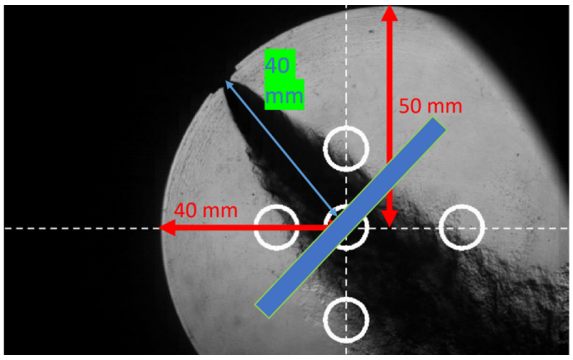

Figure 11: Locations where droplet size is measured in the experiment displayed with white circles. In the simulations, droplet sizes are measured at the plane in blue. Picture adopted from [31] and altered to include the blue plane.

4.2 Simulation description

This section explains, in brevity, how the simulation model is set up. The numerical setup and description are similar to that considered in the project thesis [42]. The CFD software used in this thesis is CONVERGE in version 3.0.26. The solver algorithm adopted in this study solves the transport equations presented in Section 3 (mass, momentum, energy, species) using a co-located finite volume method. In this method, flow quantities are stored at the cell centre, providing a more accurate representation of the flow field. To solve the equations iteratively, a density-based solver based on the pressure implicit with the splitting of operator (PISO) algorithm is used to couple velocity and pressure in a modified version applied in the software. The equations are discretized into a set of algebraic equations using a second-order scheme for spatial discretization and a time discretization of first-order (approximate PDEs as a set of algebraic equations). The Rhie-Chow interpolation scheme is used to obtain all quantities in the cell centre without the need for unwanted checkboarding [41]. Additionally, a variable time step based on the Courant–Friedrichs–Lewy (CFL) number is used, which is based on the distance travelled per time step relative to the mesh size, to ensure a balance between numerical stability and computational cost. Also, a linear solver is employed for each governing equation, with the recommended successive over-relaxation (SOR) algorithm used for most. The solver settings are based on recommended values by the software for time step control, convergence criteria, etc. The RANS RNG k-ϵ adopted with model constants as recommended to model the turbulent motions. This turbulence model is chosen due to being suitable for in-cylinder flow [59] and is widely used in RANS-based engine simulations.

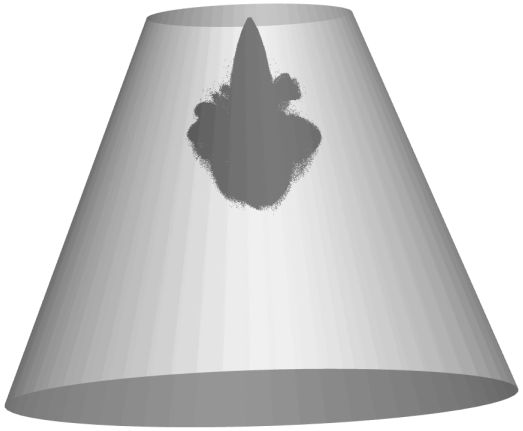

Figure 12: Computational domain shown with a spray.

The computational domain is made large to avoid liquid/wall contact and effect from the wall and is therefore shaped as a truncated cone. The top and bottom radius is 40 mm and 100 mm, respectively, and the height of the domain is 150 mm. The domain can be seen in Figure 12. The base grid size is set to 2 mm and refined is up to 0.25 mm with 3 ($\frac{2}{2^3}$) levels of adaptive mesh refinement (AMR) in places needed for every time-step. The refinement is based on the sub-grid velocity with a refinement criterion set to 1 m/s. The mesh size is also refined to 0.25 near the nozzle region with fixed embedding, as seen in Figure 13. This minimum mesh size and refinement strategy is based on grid sensitivity studies on non-reacting vaporizing spray simulations by Senecal et al. [77] for RANS-based Eulerian-Lagrangian spray modelling. This study considered a single nozzle with a diameter of 140 µm and an injection pressure of 800 bar. This minimum grid size were found to give good accuracy for penetration lengths and acceptable run times and is often set as the suggested value for spray simulations. The similarity in nozzle size to the Pelé experiment (150 µm) and lower injection pressure, meaning lower initial velocity than considered here, makes this mesh regarded sufficient and the only one to be considered. This base mesh size and the number of refinement levels are also what is used by Lewandowski et al. [78] in engine modelling based on grid dependency studies. An extra level of embedding where found to significantly increase computational time with little difference in the result. This minimum grid size is also recommended by Xue et al. [79] to give good agreement with liquid penetration. This simulation also has a Lagrangian phase, so the number of discrete particles must be specified. In order to avoid an excess of liquid mass, increasing the number of parcels with a finer mesh is necessary. Not enough parcels could lead to overprediction of penetration length. The recommended number of parcels per nozzle is set to 512,000 based on recommendations in the same study as mentioned above [77].

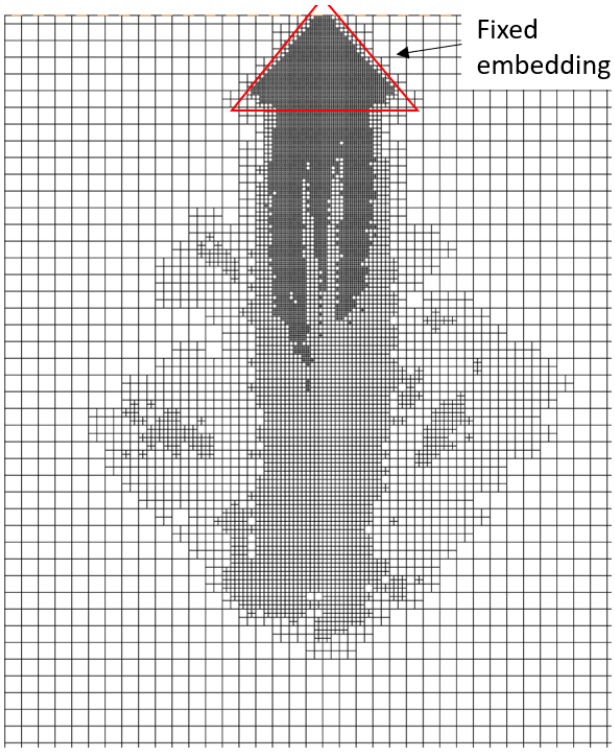

Figure 13: Part of the computational mesh with fixed embedding near the nozzle and adaptive mesh refinement with three levels of refinement based on velocity. The base gird size is 2 mm, and the minimum size is 0.25 mm. The grid is from the same spray and time as in Fig. 12.

For the continuous phase, the initial gas conditions are set with a mass percentage of N2 and O2 of 76.7% and 23.3%. The initial values for k and ϵ are set to 0.0064 m2/s2 and 0.508 m2/s3, respectively, from ECN [61] (same as used by Battistoni et al. [37]). The liquid ammonia is set to real properties from an input text file, and the mass diffusivity constants D_0 and n_0 were set to 3.74e-06 and 1.6. The turbulent Prandtl number is set to 0.9, and the turbulent Schmidt number is set to 0.78. For boundary conditions, no-slip boundary conditions are used for velocity as the influence of the wall is negligible on spray behaviour in the current setup due to the large domain and short duration of the simulations. Wall functions were also tried, but this resulted in no difference in spray morphology. The boundary conditions are set to a fixed value of 293 K for temperature, zero normal gradients for pressure and k, and a global near-wall treatment for ϵ. How the discrete phase submodels and injection parameters are set up varies in the different parts of the results and are described separately in the introductory segment of the result sections.

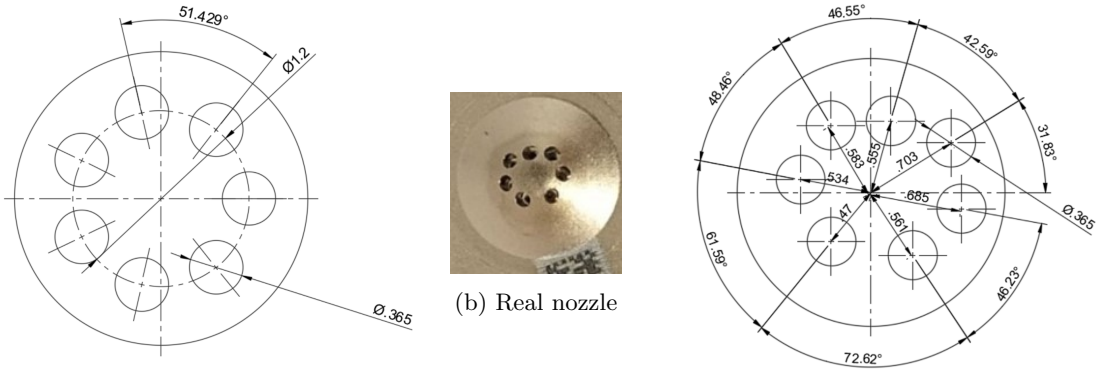

(a) Circular

(b) Real nozzle

(c) Elliptical

Figure 14: Nozzle configurations used in the model compared to the injector from the experiment.

4.3 Injector simplifications and assumptions

The dimensions of the actual nozzle hole locations were unknown, and a few assumptions and simplifications have been made. Both a simplified and more realistic configuration has been considered. The simplified configuration is perfectly circular, with nozzle holes placed at a distance of 0.6 mm from the injector tip centre and shown in Figure 14. As seen from the picture of the actual injector, the locations of nozzle holes are placed more disorganized and do not resemble a circular pattern. To address this, a more realistic nozzle shape was also considered, where the nozzle holes are placed in an elliptical shape based on the picture of the actual nozzle tip. Some holes are closer to each other and the centre of the nozzle to account for more interactions in some parts of the spray and less in others, more in line with reality. The dimensions stated in the drawing are based on the picture of the injector nozzle and are only estimates of dimensions for the real injector, as these were unknown.

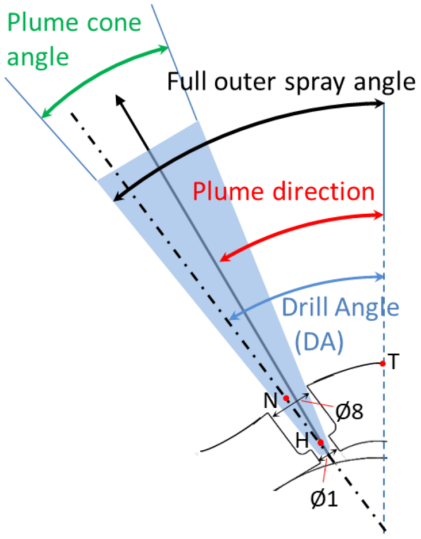

Figure 15: Schematic of a GDI nozzle. Ø1 and Ø8 represent the orifice diameter and step diameter, respectively. Picture adopted from [61].

The drill angle, the physical angle of the nozzle hole, in the plane from the experiment is approximately 46° (two times 23° w.r.t spray axis) with some uncertainty in measurement and production methods as injector geometry is very small scale. The actual injector geometry is very complex, and the different nozzles have different drill angles, as shown by Bjørgen et al. [46] for another

GDI injector. As info about the injector and experiment was limited, the drill angle is considered the same for every nozzle. This is not an input angle in the model but is utilized to establish the plume direction angle. In other words, although the configuration appears more realistic, it is still significantly simplified compared to the actual injector.

Another simplification made when modelling injection from the GDI injector is that the stepped hole geometry, i.e. the counterbore section in the injector, from Ø1 to Ø8, seen from Figure 15 is not included in the model as it usually is not included in Eulerian-Lagrangian modelling of spray from GDI injectors. However, doing so results in a slight difference in penetration length and more fluctuations downstream in spray [39]. When modelling the injection, only the small diameter, orifice diameter (Ø1), is included, and these are placed where the step diameter on the real nozzle is located.

4.4 Part 1 - flash boiling spray

This section considers the superheated condition with an ambient pressure of 2 bar ($\frac{P_a}{P_s} = 0.23$), which borders the flare flashing region [33] and therefore poses a challenge for modelling. Various parameters and approaches related to modelling the injection process, considering the in-nozzle effect on near-spray behaviour, are explored. In addition, multiple strategies for dealing with vaporization are discussed, as this aspect is reported to be problematic under flashing conditions. The reference simulation case, used for comparison, is based on the default model set up in the project work [42]. It is not the best regarding replicating experimental spray characteristics, as the shape is wide and injection velocity is assumed to be too low. However, it can still serve as a useful reference for comparison purposes. Together with previous work, this study could provide valuable insights into modelling flashing sprays.

In the reference setup, the plume direction is set equal to the approximate drill angle of the injector, and the cone angle is set to 25°, the angle used in [37]. The rate shape used to determine the mass flow rate is adopted from spray A from the Engine Combustion Network (ECN) [61]. The rest of the user-defined injection parameters for this setup are as stated in Table 7 and are together with the data from the experiment presented in Table 6, used to model the injection process.

Injection model	Blob w/ parcels evenly distributed
Discharge coefficient	0.8
Mass rate-shape	ECN spray A [61]
Cone angle	25°
Plume direction angle	23°
Nozzle configurations	Simplified circular

Table 7: Injection parameters applied in reference case in Part 1.

To model the spray development processes, the KH-RT model with model constants recommended for GDI flash is applied to deal with the breakup. In this configuration, the RT breakup constants are modified to give faster secondary breakup and smaller droplets than the standard setting. This is done to compensate for the lack of a thermal breakup model. The version used is with breakup length included and with the creation of child parcels. Additionally, it is set up with the creation of child parcels with a shed mass factor of 0.25 and a velocity constant, C_1, of 0.188. Frossling correlation with the Price flash boil model is applied to account for the phase change. The price model is set up with diameter reduction due to flash boiling. Droplet temperature is calculated based on the discretized temperature model for droplets with a radius larger than 1 μm. No scaling is applied in the evaporation and flashing, and the same applies to the droplet heat and mass transfer. Chemical reactions are excluded, and evaporation is only into pure ammonia gas. Collision is handled with the NTC collision model with the Post collision outcome employed and two layers of collision mesh. The dynamic drop drag model is utilized, and the turbulent dispersion of parcels is handled with the O'Rourke approach both these are set up with recommended settings. Table 8 summarises the submodels employed.

Breakup model	KH-RT (GDI flash)
Turbulent dispersion	O'Rourke
Collision model	NTC collision
drop drag model	Dynamic drop drag
Temperature model	Discretized temperature
Evaporation	Frossling
Flash boiling vaporization	Price

Table 8: Submodels in Reference case part 1.

When comparing parameters, only the 95% definition for liquid penetration length is shown for clarity. In this particular analysis, only one condition is taken into account, i.e. strong flash-boiling, and it is important to note that the effects of parameters may vary under different conditions.

4.4.1 Comparison of nozzle configurations

Before considering other parameters, the two different nozzle simplifications are compared to see how enhanced interactions between plumes in one part of the spray and fewer in others affect the spray characteristics. The penetration lengths with the two different configurations are shown in Figure 16 both averaged over the seven nozzle holes and not. It is seen that the elliptical configuration has more spread in penetration lengths for different nozzles compared to the simpler configuration, and the reported distances are both longer and shorter. The difference is negligible at the start of injection and increases with time. The spread in LPL cancels each other out, and from the averaged plot, no clear difference can be seen between these two. For VPL, more nozzles have increased penetration compared to decreased for the elliptical configuration, and the average is longer after approximately 0.75 ms. The difference in interactions between the plumes thus leads to a change in droplet size and velocity. In the elliptical configuration, more interactions are expected as four of the nozzle are closer, as seen in Figure 14. This indicates that more interactions result in larger droplets from coalescence and, thus, longer VPL due to increased momentum (on average). For liquid penetration no distinct difference between the two configurations meaning that the vaporization/breakup process overrules the difference in droplet momentum.

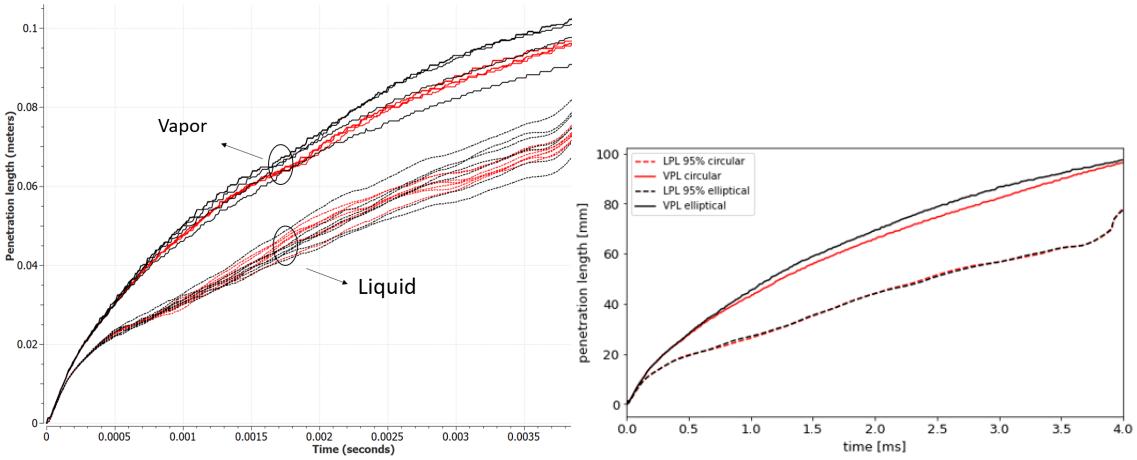

Figure 16: Penetration length for the different nozzle configurations. On the left side, the reported length for every nozzle is shown, and on the right, the averaged value. Red and Black correspond to the circular and elliptical, respectively.

Considering the shape, a clear difference can be spotted in the elliptical configuration leading to an unsymmetrical shape as seen in Figure 17. Less radial dispersion can also be seen, which could indicate less collision. However, only one plane is considered here, and behaviour is expected to differ for other planes as opposed to the symmetrical. Despite some differences in penetration lengths, the simplified circular configuration will be used further in the results as the unsymmetrical configuration is also a simplification, and what plane is equivalent to experimental regarding nozzle configuration is not known, thus simplifying the comparison of spray shapes. The difference in the sprays was also assessed with different input angles (cone and plume of 19 and 18). However, the same trend was seen, and the results are thus not presented. Suppose the penetration lengths obtained from the experiment are more comparable to the penetration length of the longest nozzle. In that case, using the simplified configuration and averaging will lead to some underprediction in the last 2 ms of injection. This illustrates some of the challenges when comparing simulations to experimental data, as different methods for measuring the same parameter could result in different results and conformity.

4.4.2 Mass rate-shape

This section considers the effect of different initial velocities and the shape of velocity profiles on spray morphology. The rate-shape from ECN spray A applied in the reference setup is from a

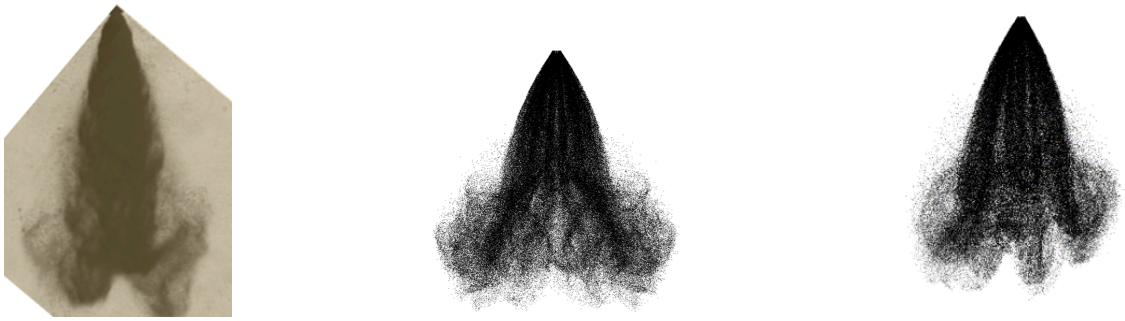

(a) Experimental [31] (b) Circular (c) Elliptical

Figure 17: Shape of spray from the two different nozzle hole configurations considered in one plane after 1 ms. Compared to experimental shape.

single-nozzle diesel injector with a much higher injection pressure (1500 bar) than a GDI injection, and a different shape of the profile is expected. Also, the injection duration (1.5 ms) is significantly shorter, meaning the dimensions get wrong when scaled to the longer lasting injection. This is especially apparent at the start and end of injection, as the change in mass flow is less distinct. The current rate-shape is compared to a rate-shape from a modified spray G, multi-hole gasoline injector (200 bar). The modified shape is elongated in the middle so that ramp-up and ramp-down are scaled more realistically. Spray G has a higher mass flux than the injector of interest but is here used to see the effect of different shapes. The instantaneous injection pressure graphs (Eq. 28) for the different rate-shapes are presented in Figure 18. Two different discharge coefficients are considered where C_d of 0.7 results in a mean pressure of approximately 120 bar and C_d of 0.8 a max pressure below 120.

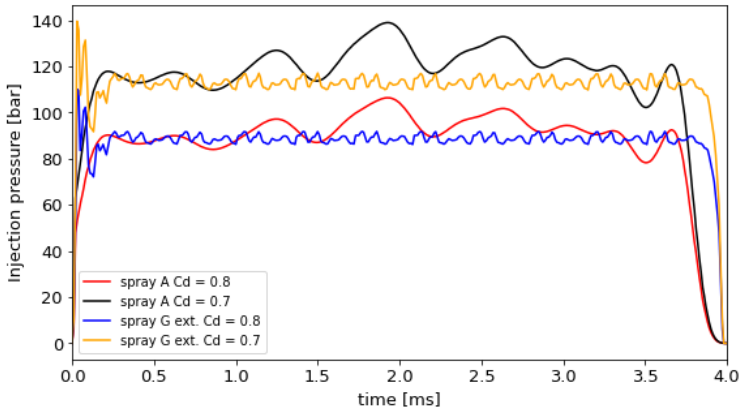

Figure 18: Instantaneous injection pressures for different rate-shapes and discharge coefficients.

The rate-shape for the current injection is unknown. However, momentum flux measurements from ammonia in another multi-hole injector were available from the lab at the higher injection pressure of 180 bar. The measurements were scaled to the same order of magnitude as the mass flow from spray G. Three measurements from the lab is presented in Figure 19, not accounted for measurements noise. The profiles are similar in shape, with a more distinct peak at the start of injection for spray G. In [46], Two peaks in the momentum flux curve were reported, at the beginning of the injection and at the end of the injection.

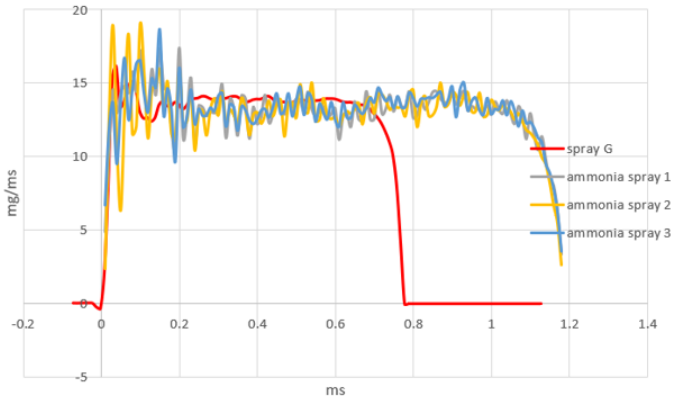

Figure 19: Spray G mass flow compared to mass flux measurements from the EPT motor lab at NTNU.

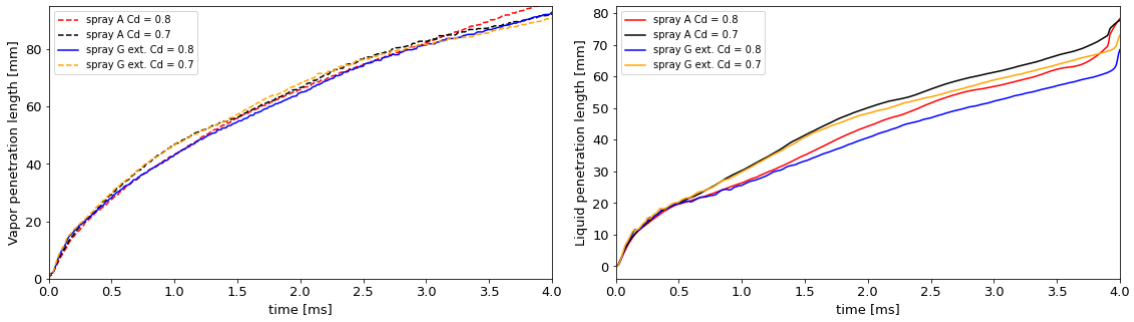

Figure 20: Penetration length for different initial velocities and shape of velocity profiles. Left: Vapor, right: liquid.

The difference in penetration length is presented in Figure 20. For vapor penetration, the two cases with higher initial velocity have longer penetration lengths at the start of injection, as expected, but the difference is small and decreases in time. No clear distinction between the different rate-shapes can be seen for the same C_d. For LPL, the difference is more distinct, and at higher injection pressure, longer liquid penetration is seen. Here, a clear distinction between the different profiles is seen as the spray A profile results in a longer LPL after 1.5 ms due to the higher velocity mid-injection. Different rate-shapes are seen not to be crucial to VPL if mean injection pressure (i.e. initial parcel velocity) is roughly the same but can have some effect on liquid penetration.

4.4.3 Distributions of injected parcels

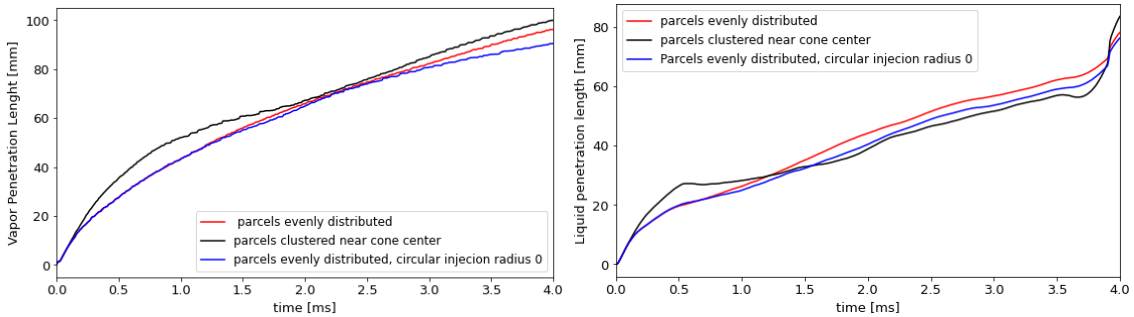

Figure 21: Penetration length for different distribution of parcels. Left: Vapor. Right: liquid.

(a) Reference (b) Parcels clustered (c) Injection radius 0

Figure 23: Distributions of parcels shape effect on shape (1 ms).

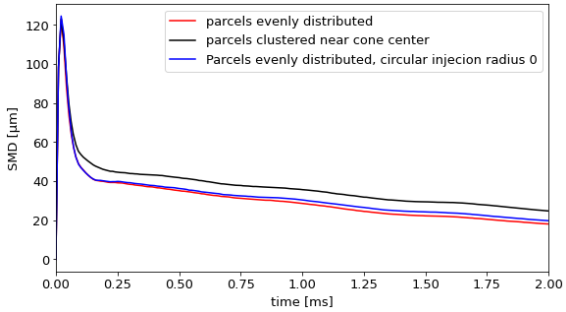

Figure 22: Droplet size for the whole spray with different distributions of Parcels.

Apart from the Cone angle, two other parameters are essential for modelling the injection of parcels and the placement of parcels when injected. In this section, parcels evenly distributed are compared to when clustered. In addition, a reduction in injection radius is considered from the radius of the nozzle to zero.

Figure 21 presents the effect on penetration lengths. When the parcels are clustered, significantly longer VPL is observed at the start of the injection. This is more in line with the experiment, as the reference case underestimates penetration. However, this effect decreases in time, and less difference is seen in the last half of the duration. The LPL for the clustered case is also longer than for the rest at the start, and then the difference diminishes and ends up with the lowest. The more extended penetration at the injection's beginning can be explained by the larger droplets in the spray, as seen in Figure 22, as larger droplets travel faster. This could indicate that the enhanced interactions in the same plume lead to increased droplet size. For the elliptical configuration, the increased droplet size was due to interactions between the plumes giving a delay in the increase of droplet size compared to here. These larger droplets also travel shorter before they vanish as the LPL, after some time, is the longest for the smallest droplet size. This is the opposite seen in Eq. 29 where smaller droplets evaporate faster. Zhang et al. [36] hypothesized that the cooling effect of ammonia slows down the vaporization of tiny droplets making these travel further than the larger droplets. The injection radius set to 0 results in minimal impact since the size of the injected droplets is similar to the nozzle diameter. However, the droplets are slightly larger than the default scenario due to increased interactions within the plume.

The impact on shape can be observed in Figure 23. Clustered parcels exhibit a narrower angle near the injector, and fewer parcels are present downstream due to more vaporization than in the reference case. Furthermore, a reduced narrowing effect, V shape, and weaker reticulation zones are seen, which indicate fewer interactions between the different plumes.

4.4.4 Initial parcel size

For high degrees of superheat, flow exiting the nozzle can exist of a large amount of vapor in addition to droplets, reducing initial droplet diameter. In this section, the effect of different initial droplet sizes is considered. The initial droplet sizes are generated from a Chi-squared distribution with four different specified Sauter mean diameters. Among these, three are smaller and one has a SMD matching the larger step diameter of 365 µm to observe the effect.

Figure 25 demonstrates that the droplet sizes converge rapidly to the same value after approximately 0.1 ms for all droplets in the spray, except for the smallest one. Also, a slight variation is observed for a diameter of 50 µm. This indicates that initial droplet size is not so important for spray morphology. The crucial for droplet size in the early phase, and thus VPL, is what happens in the initial phase, i.e. breakup, vaporization, and interactions decide this to a greater extent. The penetration lengths are presented in Figure 24 and shows little effect of the different initial sizes. Except for the two smallest initial sizes with smaller SMD for the whole spray, this is reflected in the behaviour that differs from the rest. The smallest droplet size results in a strange shape on the penetration length graph and differs from the behaviour observed in the experiment. This effect is similar to that encountered for small plume angles and large cone angles (enhanced interactions of plumes) in the project work. The shapes presented in Figure 26 illustrate that smaller droplets exhibit greater radial dispersion on spray, leading to a wider spray at the tip. The difference in PL for 50 µm could be explained due to more radial dispersion as the reported length is not corrected for the widening. The behaviour of the 20 µm initial droplet size is distinct from the others, as it exhibits significant dispersion also early in the spray. Note that this representation represents parcels and not droplets, which means that the number and size of the droplets per parcel could vary.

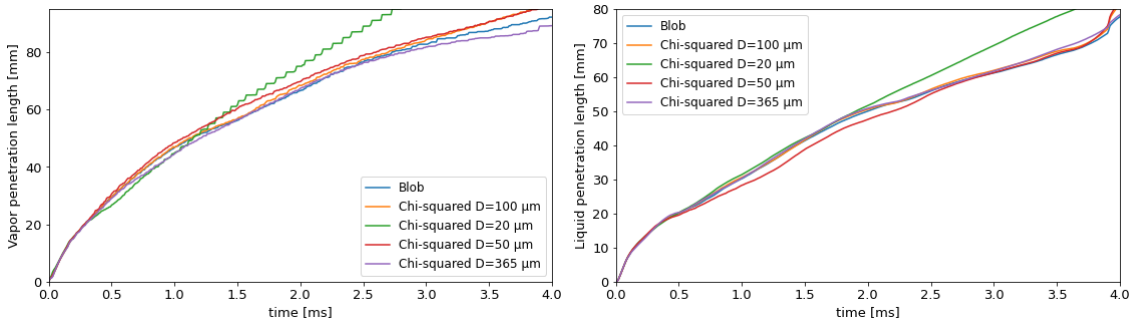

Figure 24: Effect of different initial droplet sizes on penetration length. Left: Vapor. Right: liquid.

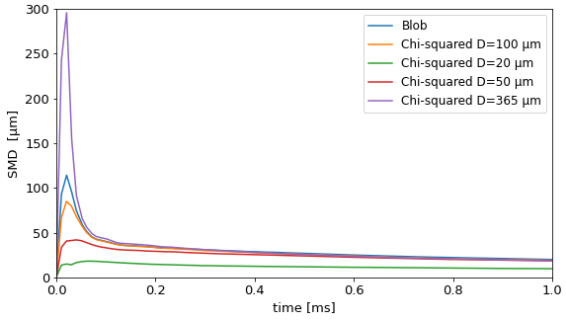

Figure 25: Effect of different initial droplet sizes on SMD for the whole spray.

(a) Blob (b) 50 µm (c) 20 µm

Figure 26: Effect of different initial size on shape (1 ms).

4.4.5 Models for phase change

The models for evaporation and flash boiling are believed to be one of the reasons VPL is underestimated, as An et al. [51] conclude that common models overestimate the evaporation rate under flash boiling conditions resulting in too small droplets. In this section, the Frossling model is considered with and without the superheated term by Price in addition to a conventional boiling model.

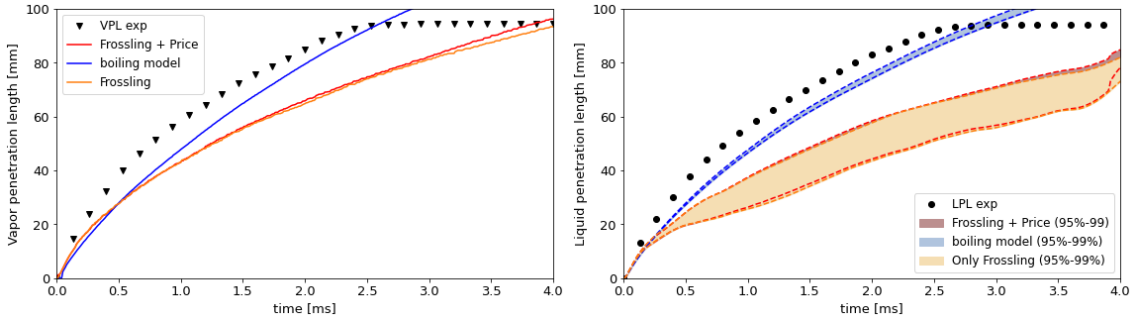

Figure 27: Evap model penetration lengths Left: Vapor. Right: liquid.

From the penetration lengths presented in Figure 27, it is apparent that the result with and without Price is the same, meaning that the superheated term (heat transfer from within droplet) contribution to the reduction in mass is negligible under these conditions. This is the same behaviour as reported by Zhang et al. [36]. The only difference in these models is the SMD at the start of injection, seen in Figure 28, which is reduced when Price is applied. The same results with both models are peculiar because the superheat term in the Price model is dependent on the temperature difference between the boiling point and droplet temperatures, which is 39 K during the initial injection phase. Also, Shin et al. [50] reported substantial differences in results with and without the Price model. However, this was for a more superheated spray. One possible reason for the negligible difference is that the rapid cooling effect significantly alters the degree of superheating. The VPL with Frossling is longer than that of the conventional boiling model until 0.5 ms, and after that, the conventional boiling model results in the longest PL and better agreement with the experiment. This is also the case for liquid penetration, which closely resembles vapor penetration.

The boiling model results in a more rapid droplet size reduction, seen on the graph of droplet size for the entire spray. This is consistent with the lower VPL from the boiling model initially but does not explain the behaviour after this, where the boiling model achieves longer VPL. Considering the droplet size in the plane 40 mm from the injector, the SMD from the boiling model is three times larger than with Frossling. The SMD in the plane is consistent with that of the entire spray, meaning that the droplet size does not change considerably after the rapid size reduction experienced initially. This indicates that the difference between the surrounding air and the boiling temperature of the liquid is small from the significant cooling effect during the first 0.5 ms. Hence, while the boiling model initially yields smaller droplets, this effect diminishes after approximately 0.5 ms, resulting in the largest droplet size. The droplet size during this

phase significantly influences the penetration. It is worth noting that the breakup models remain constant, indicating that the phase change models are decisive here.

The shape when the boiling model is applied also deviates, as seen in Figure 29. The individual plumes are distinct, and no difference in the density of parcels near the tip compared to the base indicating that very little evaporation is happening. The V-shape, not the tulip shape, is obtained, giving characteristics similar to sprays under non-flash boiling conditions. The boiling model does not accurately capture the underlying physics but results in a longer penetration length in better agreement with the experiment. This is due to a lesser reduction in droplet size which could indicate that with Frossling, the reduction in droplet size is overestimated. An explanation for this is that the Frossling model (both w/o Price model) underpredicts the phase change at the start of injection (Fig. 28) which results in less cooling initially and more evaporation later on. A faster thermodynamically induced breakup, e.g. as Shin et al. [50], or enhanced reduction in droplet size due to phase change for superheated droplets (what Price model should have done) are two ways to achieve a smaller droplet size initially.

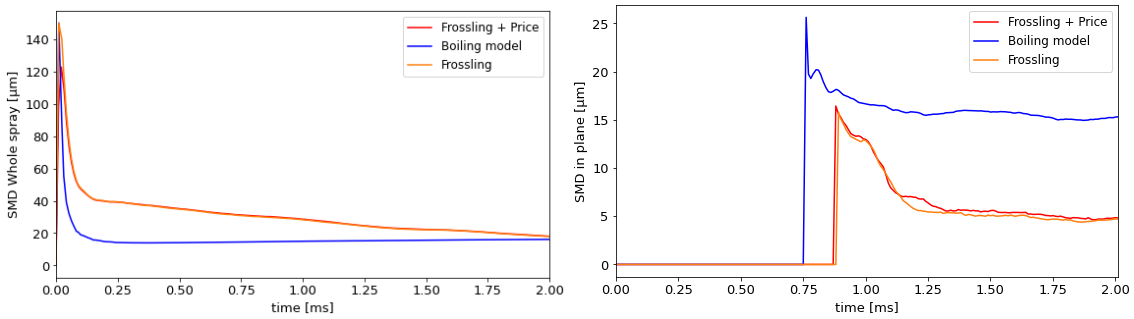

Figure 28: Droplet sizes for different evaporation models. Left: SMD for the whole spray Right: SMD in plane 40 mm from the injector. With the boiling model, the droplet size is approximately the same in both.

(a) Frossling + Price

(b) Boiling model

(c) Frossling

Figure 29: Effect of different vaporization models on shape (1 ms).

4.4.6 Different mass and diameter

In this section, different masses and diameters are considered and set up so that the initial parcel velocity is the same. I.e. same initial velocity (and injection pressure), but the momentum of droplets is increased due to larger initial parcels. Here a different set of angles (cone 19, plume 18) and a discharge coefficient of 0.7 is used as these yield spray characteristics more aligned with the experimental. Both the step diameter of 365 µm and orifice diameter of 150 µm, illustrated in Figure 15 are used.

For the small diameter, the pressure curve is the 'Spray A Cd=0.7' in Figure 18 and corresponds to an approximate average initial parcel velocity of 160 m/s. The discharge coefficient is chosen for the larger diameter, and mass is adjusted to match the initial velocity graph. Discharge coefficients of 0.8, 0.5 and 0.3 correspond to 265 mg, 165 mg and 100 mg of injected mass, respectively. In addition, the initial mass of 40 mg is used, and a C_d of 0.125 was required to reach the same initial velocity. Only the 95 % definition of LPL is shown due to the number of datasets per plot. Experimental data are added for comparison also.

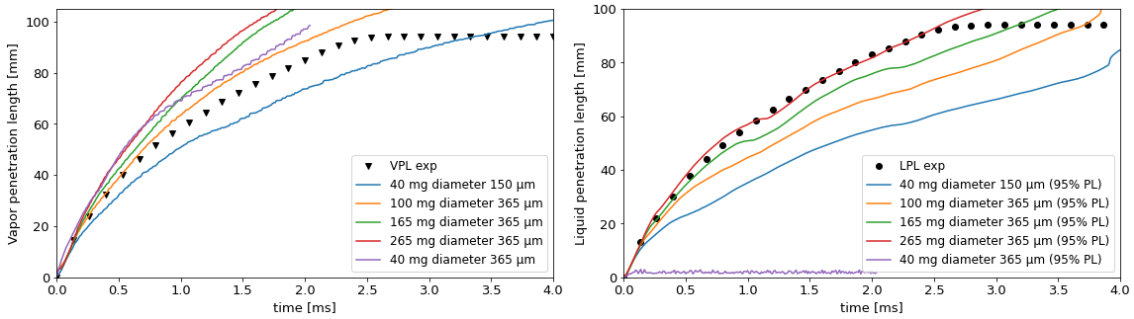

Figure 30: Different mass and diameter. Left: Vapor. Right: liquid. Large and small diameter refers to step and orifice diameter seen in 15.

Penetration lengths for the cases considered are illustrated in Figure 30. It shows that when increasing mass, i.e., initial droplet size, penetration length increases. This increased droplet momentum yields enhanced penetration for both the liquid and vapor phases. Here the injection velocity is higher compared to the reference case, but penetration for the 40 mg and small diameter is still underestimated compared to the experimental. When using a larger mass, the VPL is overestimated for all the masses. A better agreement with LPL is seen. However, only the 95% definition for LPL is included, as this is applied in the rest of the section. If the 99% definition were used, the lengths would increase. The two cases with the same initial mass and velocities have a similar effective diameter and are expected to behave similarly. However, when using the larger diameter, the results are nonphysical. Only a small number of parcels are injected, on the order of 10^4 instead of 10^6. The cause of this behaviour is not known.

The shape presented in Figure 31 shows a clear trend that when mass increases, the shape goes

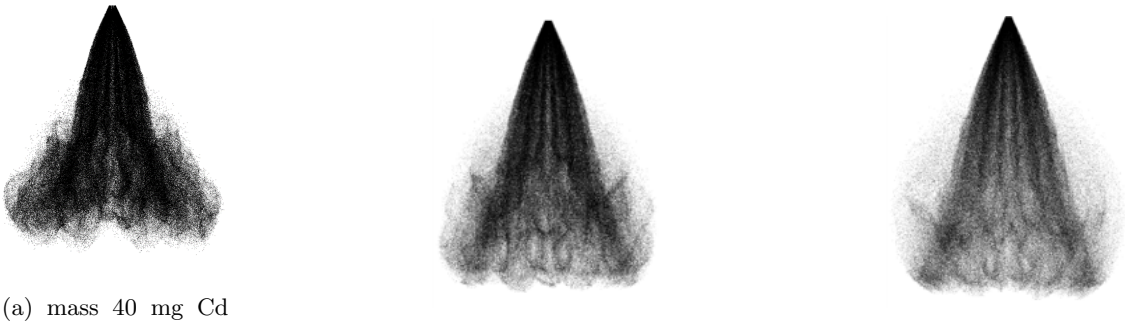

(a) mass 40 mg Cd 0.7

(b) mass 100 mg 0.29

(c) mass 265 mg Cd 0.8

Figure 31: Effect of different initial mass on shape.

towards a constant spray angle, a more V-shape pattern instead of a tulip shape. The expected collapse effect is not accurately captured. If only step diameter (365 µm) and injection pressure are known, the data provided in the paper, and employing a common C_d would result in a significantly different outcome than when using the measured mass and the small diameter. Underestimation of penetration compared to the experimental would not be encountered. Adjusting the initial velocity and input angles, it is plausible that good agreement with experimental data could be obtained.

4.4.7 Summary

The deceleration of the droplets at the start of injection is key for the penetration lengths. Longer penetration lengths can be achieved by larger droplets some time after the start of injection. i.e. less reduction in size from either breakup or evaporation, or increase in size due to interactions both within and between plumes. Long penetration and accurate reproduction of shape appear to be contradictory. Furthermore, there is no noticeable difference between Frossling with or without the Price model. In the case of highly flashing sprays, improvements in the phase change and breakup models are likely required to improve the results. Additionally, it has been demonstrated that relying solely on the step diameter is insufficient for modelling sprays from GDI injectors.

4.5 Part 2 - Multiple thermodynamic conditions

The following section represents the main part of this thesis and will present the spray simulations for the six different pressures. Different approaches for setting up the simulations for the various conditions were used. However, in this section, only the results from one of the approaches are presented. The submodels applied in the current set ups resemble those used previously in Part 1. Only the parameters and models that differ from previous will be mentioned when explaining the setup for the parcels.

Injection model	Blob w/ parcels evenly distributed
Discharge coefficient	0.72
Rate-shape	From Xu et al. [80] (as used in [36])
Cone angle	Vary with conditions
Plume direction angle	Vary with conditions
Nozzle configurations	Simplified circular

Table 9: Injection parameters applied in result part 2.

A rate-shape from a model by Xu et al. [80] is adopted in these simulations. This profile is similar in shape to the spray G illustrated in Figure 18 but with a less distinct peak at the start of injection. The shape of the profile was shown to have a minor effect on spray morphology given the same discharge coefficient. However, without the distinct rise in the beginning, a lower discharge coefficient could be applied without exceeding the injection pressure stated in the experiment. When the spray G profile was set to match the experimental pressure, the average injection pressure was significantly lower. The profile is combined with a discharge coefficient of 0.72 to fit a maximum injection pressure of 120 bar. The input angles are set to vary with conditions, and the prescription is explained in the following subsection. A summary of the injection parameters can be found in Table 9.

Due to the difference in approach in breakup model parameters by others when replicating ammonia spray, and to reduce the number of variables. Only the two sets of breakup parameters, GDI flash and GDI non-flash, were initially considered. These can be seen in Table 10. In the GDI-flash the RT constants are reduced, leading to faster RT-breakup and smaller droplets after the breakup (Eq. 42,43). Both these are set up with the creation of child parcels with a shed mass factor of 0.25 and a velocity constant, C_1, of 0.188, as previously. The different set of constants is applied based on Li's [33] characterization of spray behaviour based on the degree of superheat. Flashing bubble behaviour in near-field and far-field is said to dominate the behaviour for $\frac{P_a}{P_s} < 0.5$, and thus this is set as a limit for when to apply GDI flash parameters. For the ambient pressure of 4 bar ($\frac{P_a}{P_s} = 0.47$), both sets of constants were applied to highlight the difference. As seen in the literature review of other simulations of liquid ammonia spray, some model constants have been altered. But with different approaches, and not all settings have been reported. For the case with an ambient pressure of 15 bar, additional breakup model parameters inspired by literature have been tested. Table 10 shows two setups from the literature applied to subcooled sprays. Both these have increased the $B1$ constant to delay the initial breakup and adjusted the C_{RT} constant.

KH model parameters	GDI flash	GDI non-flash	Li et al. [7]	Pandal et al. [38]	MOD
$B0$ (size constant)	0.6	0.6	0.61	0.6	0.61
$B1$ (time constant)	7	7	36	40	20
$C1$ (velocity constant)	0.188	0.188	N/A	N/A	0.188
RT model parameters					
C_{RT} (size constant)	0.25	0.6	0.68	0.1	0.68
C_I (time constant)	0.1	1	N/A	1	1
C_{bl} (length constant)	0	0	18	N/A*	10

Table 10: KH-RT model parameters applied in the simulations and from literature (*not known whether KH-RT with or without breakup length were used).

Conditions	$\frac{P_a}{P_s} < 0.5$ ($P_a = 2, 4$ [bar])	$\frac{P_a}{P_s} > 0.5$ ($P_a = 7, 10, 15, 25$ [bar])
Break-up model	KH-RT (GDI flash)	KH-RT (GDI non-flash)
Turbulent dispersion	O'Rourke	O'Rourke
Collision model	NTC collision	NTC collision
drop drag model	Dynamic drop drag	Dynamic drop drag
Temperature model	Discretized temperature	Uniform temperature
Evaporation	Frossling	Frossling
Flash boiling vaporization	Price	-

Table 11: Submodels applied for the different conditions in part 2.

To account for phase change, Frossling with Price for is applied for $\frac{P_a}{P_s} < 0.5$, with droplet temperature based on the discretized temperature model for droplets with a radius larger than 1 μm. The less computationally expensive uniform temperature model is applied for the cases with an ambient pressure of 7 bar and higher. The two temperature models were tested for the 7 bar conditions, and no apparent difference in the result was observed. These results can be found in Appendix C Figure 56. The collision, drag, and dispersion models were configured the same as in Part 1. Modifications made to these parameters are less significant [34][39], and changes in these were thus not considered.

4.5.1 Angle prescription

Input angles are crucial to capture spray behaviour, and several methods for describing these were considered. The cone and plume direction angles, seen in Figure 15, must be specified. From the literature review, it is clear that the cone angle, the thickness of a single plume, changes with conditions, especially for ambient pressures close to or under the vapor pressure. But also, the plume direction angle has to be specified. As an approximate drill angle is known, setting this equal to the plume angle is a place to start. This was done in the reference setup used in the parametric study, but the shape was not accurately captured. Due to flow in the stepped hole geometry in the real injector, the plumes get pushed towards the injector axis, making the actual plume angle lower than the physical drill angle [39]. The absence of input angles in the literature challenges the prescription. However, some simulation cone angles are known and presented in Figure 32b. When considering various conditions, it is apparent that a systematic approach for specifying the angles corresponding to different conditions is required.

To prescribe the input angles, methods were inspired by Lewandowski et al. [78][34], who used experimental angle measurements to decide input angles. A simplified relation relating the input angles and full spray angle stating that

$$Outer\ spray\ angle = Cone\ angle + 2 \cdot Plume\ direction\ angle, \tag{46}$$

were used, and to close the system of equations, a relation between the plume and cone angle was adopted from Duronio [30]. These relation are $\frac{plume}{cone} = \frac{37}{30}$ and $\frac{plume}{cone} = \frac{19}{24}$ for the subcooled and superheated, respectively. This method was adopted but based on the angle near the injector, for liquid only, instead of the angle measured at half penetration, illustrated in Figure 7. Also, the experimental angle is obtained at a given time rather than a given penetration length as the angle varies and stabilizes some time after the injection, as seen in [31]. The "steady-state" angle can be reached for only some conditions if a distinct length is used. Figure 32a in dim colours shows the angles obtained from this method. Using this method, nearly constant angles are shown for the subcooled conditions with a cone angle around 20°, similar to the cone angle used in similar studies [38][36][37]. However, the prescribed angles are unsatisfactory for the superheated and critical conditions. The cone should increase for increased superheat, and the leap around saturation pressures makes it unsuitable for these conditions. A smoothing relation was proposed where the plume cone fraction was set to unity around saturation pressure. However, this solution was deemed insufficient and not considered satisfactory.

The approach for prescribing input angles was improved by supplying cone angles and thus not

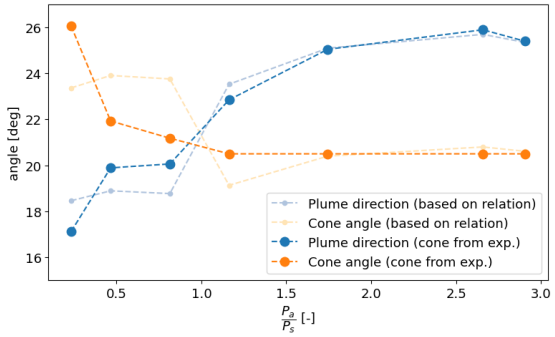

(a) Input angles for different conditions set to fit experimental angle near the injector at 2 ms.

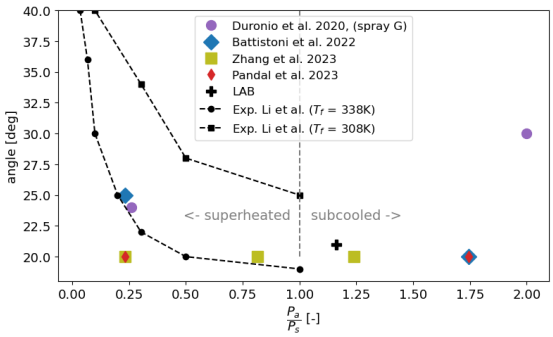

(b) Cone angles used in simulations (in colours) and from experiments (black).

Figure 32: Input angles

relying on the cone/plume relation. For subcooled conditions, the cone angle is set to a constant value of 20.5°. This is similar to cone angles obtained with the relations for $\frac{P_a}{P_s} > 1.5$. Also, this value agrees with preliminary measurements from spray pictures from the lab at NTNU. These pictures are from a different GDI injector and with injection and ambient pressure of 180 bar and 10 bar, respectively, further details and pictures are in Appendix B. For the superheated conditions, the cone angles are based on the relation between $\frac{P_a}{P_s}$ and angles, stated in the recent paper by An et al. [51]. These angles are from the experiment by Li. et al. [33] towards the end of the injection, where they reach a steady state, and are shown in Figure 32b for two different fuel temperatures. The angles for the fuel temperature of 338 K were used and increased by eight per cent, so the angle for $\frac{P_a}{P_s} = 1$ is 20.5°. From this (with polynomial curve fit), cone angles were obtained for the different conditions, and the corresponding plume angle could be calculated from Equation 46. The angles are illustrated in Figure 32a in bright colours and presented qualitatively in Table 12. With this approach, only a slight increase in cone angle as moving into the superheat region is predicted, while the plume angle changes more significantly. For $\frac{P_a}{P_s} < 0.5$, a dramatic change in angles is seen, which substantiates that these conditions are challenging from a modelling perspective. From the spray picture in Figure 55, a more distinct increase in angle is seen for the spray in the transitional region ($\frac{P_a}{P_s} = 0.58$), which may imply that the prescribed cone angles with this method are too low for $0.5 < \frac{P_a}{P_s} < 1$.

P_a [bar]	$\frac{P_a}{P_s}$	Exp. angle near injector	Cone angle	Plume direction angle
2	0.23	60.3	26.06	17.12
4	0.47	61.7	21.93	19.89
7	0.81	61.3	21.18	20.06
10	1.16	66.2	20.50	22.85
15	1.74	70.6	20.50	25.05
25	2.91	71.3	20.50	25.40

Table 12: Angle input in simulation. The experimental angle is the spray angle measured at half penetration after 2 ms.

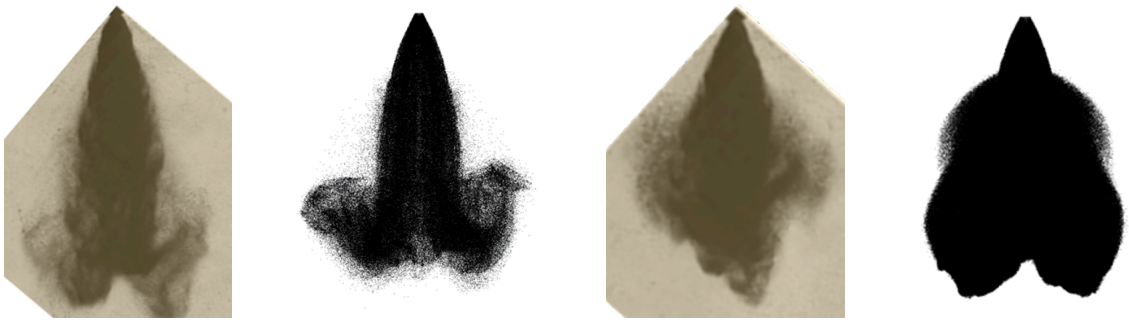

(a) Exp. $P_a = 2$ *bar* (b) Sim. $P_a = 2$ *bar* (c) Exp. $P_a = 7$ *bar* (d) Sim. $P_a = 7$ *bar*

Figure 33: Comparison of shape after 1 ms. Experimental pictures are obtained from [31].

4.5.2 Result and discussion

The subsequent subsection presents and discusses the results for the six conditions using the model setup described earlier in this section. Firstly the shape is presented and compared to experimental data to validate the angle description method. Then the penetration length for vapor and liquid is presented to see how well the main spray morphology is captured. Finally, the droplet sizes for a location in the spray are considered to assess the extent to which more minor spray features are accurately captured.

Comparison of shape

A comparison of shape 1 ms after the start of injection is presented in Figure 33. Unfortunately, only two pictures of the conditions considered were available in the paper by Pelé [31], and the comparison is only for the two superheated sprays of 2 and 7 bar. However, the main spray characteristics are well replicated for these two pressures. For the most superheated conditions, the collapse of the jets is well captured, and the spray body from the simulation is slim and similar in shape, with a clear reduction in spray angle downstream. Distinct vortices are also observed, significantly more pronounced than the experimental results. Nevertheless, since the parcels and droplets are not directly comparable, it is not possible to say certainly to what degree this effect is overestimated, if it is indeed overestimated at all. The predicted shape for the 7 bar case is wider, and the width is quantitatively in agreement with the experiment. Here no reduction in spray angle is seen downstream for either. At the tip of the spray, there is an apparent disparity between the experiment and the simulation. The spray narrows toward the end in the experiment, while the simulation has a broader shape with less narrowing effect. For both conditions, the spray from the experiment is clearly not symmetric, and the liquid penetration is longer on the right-hand side.

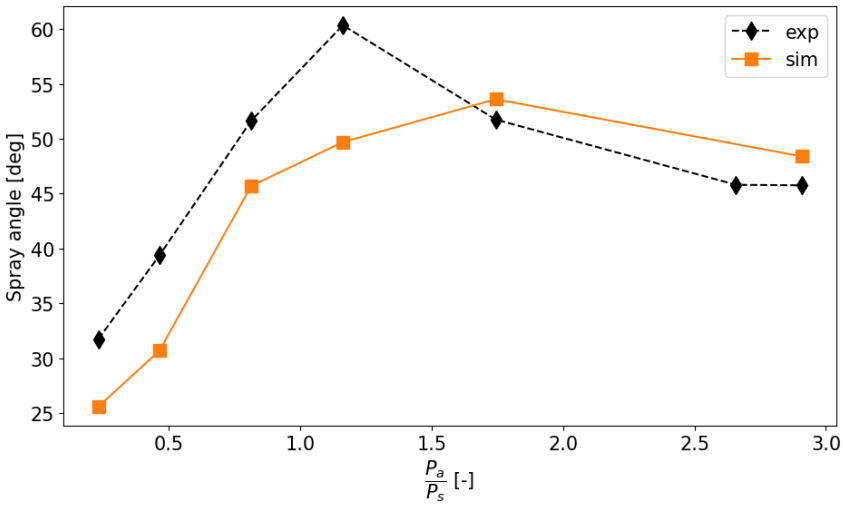

Figure 34: Spray angle at half penetration length measured 2 ms after the start of injection for different conditions. Comparison of numerical and experimental angles.

The shape is also assessed quantitatively, with the spray angle measured at half penetration, presented in Figure 34. Further details about the measurements are found in Appendix A. As a result of the spray collapse effect, the two most superheated sprays have noticeably lower angles compared to the other conditions. The figure shows that the trend is captured and that there is a good qualitative agreement between numerical and experimental. However, some discrepancies between experimental and numerical exist. The angles for the two highly superheated sprays and those close to the vapor pressure are significantly underestimated. The distinct peak in angle for the pressure of 10 bar ($\frac{P_a}{P_s} = 1.16$) is not captured. While some deviations were expected for the lowest pressure conditions due to the strong flash boiling effect, such deviations were not expected for the intermediate pressure ranges. The excessively narrow sprays could indicate excess interactions within the spray, possibly due to a low plume or wide cone angle. The best agreement is observed for the significantly subcooled conditions, with only slight overprediction of the spray angle. The plume direction angle is set wider than the approximate plume angle of 23° for these and could potentially account for some of the discrepancies.

The comparison involves a significant amount of uncertainty due to several factors. Experimental angle measurements are challenging because it is difficult to define the outer boundaries of the spray precisely. Also, there is some uncertainty in the numerical measurements and the specific plane from which the picture is taken, in addition to the simplifications in the model, e.g., nozzle locations.

Penetration length

Figure 35 presents the penetration lengths for the three superheated sprays. The results from the two sets of breakup parameters are presented in blue and red for flash and non-flash, respectively. The numerical results show a problem with the strong flashing conditions as the 2 and 4 bar pressure conditions lead to significant underprediction in penetration for both vapor and liquid phases. For the lowest pressure, a large leap in penetration is observed after approximately 1.7 ms and unrealistic evolution in penetration (similar to the smallest droplet size in Fig. 24). This behaviour was also encountered in the project thesis [42] for large cones and small plume angles. Using a smaller cone and larger plume angles would result in better agreement with penetration, as demonstrated in the project thesis. Furthermore, this adjustment would eliminate the significant leap in penetration also. This agrees with Duronio et al. [57] that capturing the main spray morphology for flashing sprays requires tuning cone angle to non-physical value. However, this would also affect the replication of shape for the worse. The 4 bar case also demonstrates a significant underprediction of penetration, regardless of the two sets of breakups considered. Altering the secondary RT breakup does not noticeably affect the VPL here. Deceleration at the start of injection is decisive for VPL, and the phase change modelling or early breakup must be changed

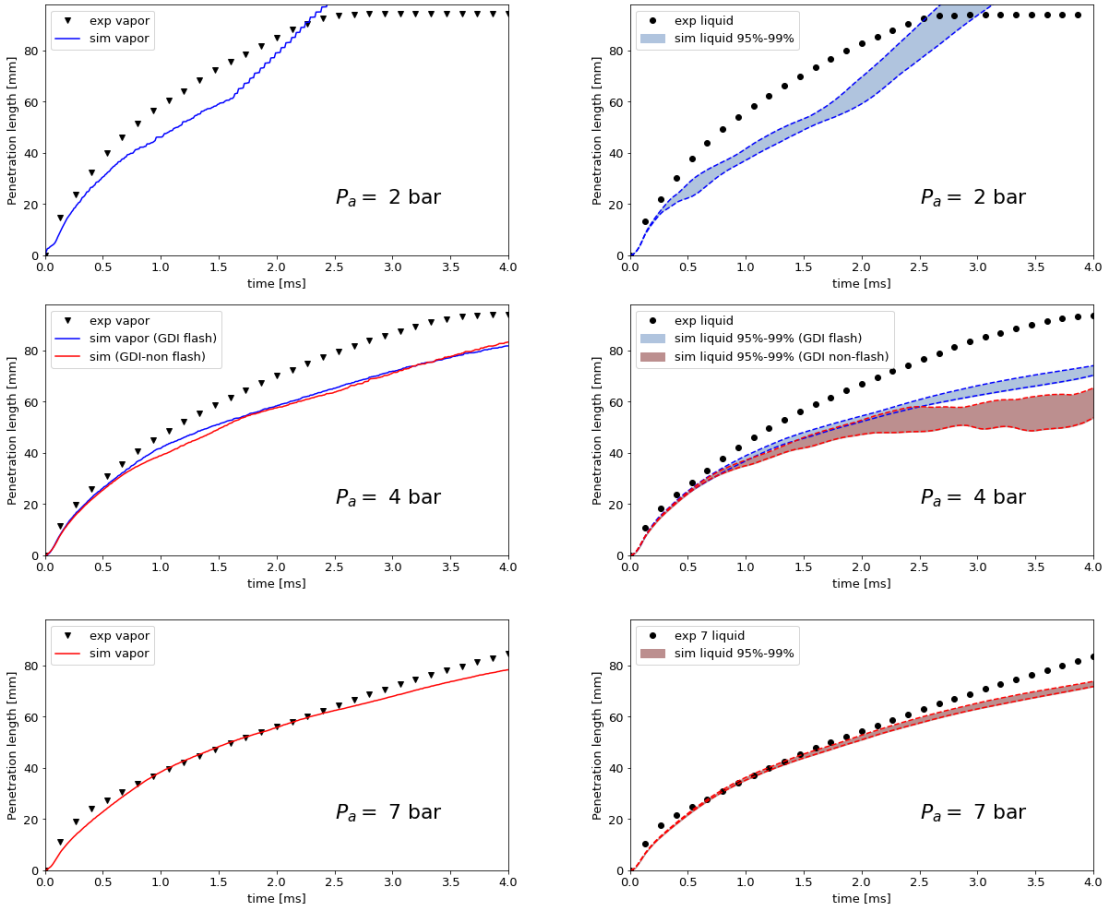

Figure 35: Vapor (left column) and liquid (right column) penetration length for chamber pressures of 2, 4, and 7 bar. Blue and red lines represent breakup as GDI flash and GDI non-flash, respectively. Experimental values from [31].

to increase this, as shown in Part 1. Still, the more minor droplets result in more extended liquid penetration, suggesting a decrease in the vaporization rate compared to larger droplets. Zhang et al. [36] explained this due to the cooling effect. For the last superheated condition with a pressure of 7 bar, there is an improvement in agreement with the experiment. However, the penetration is still underpredicted during the early and late injection phases.

Figure 36 presents the penetration lengths for the higher pressures. These results show better agreement than the lower pressure conditions, with the highest level of agreement observed at the beginning of the injection. Also, the predicted behaviour is similar for both phases. Furthermore, the shape of the numerical graph is more bent and deviates from the experimental data, resulting in overpredictions in the middle part of the injection. This indicates that the droplets in the model travel faster in the middle section of the injection and slower at the end, compared to the experiment. This overprediction also increases with the increase in back pressure. For the 25 bar case, experimental data were only available for half of the injection period.

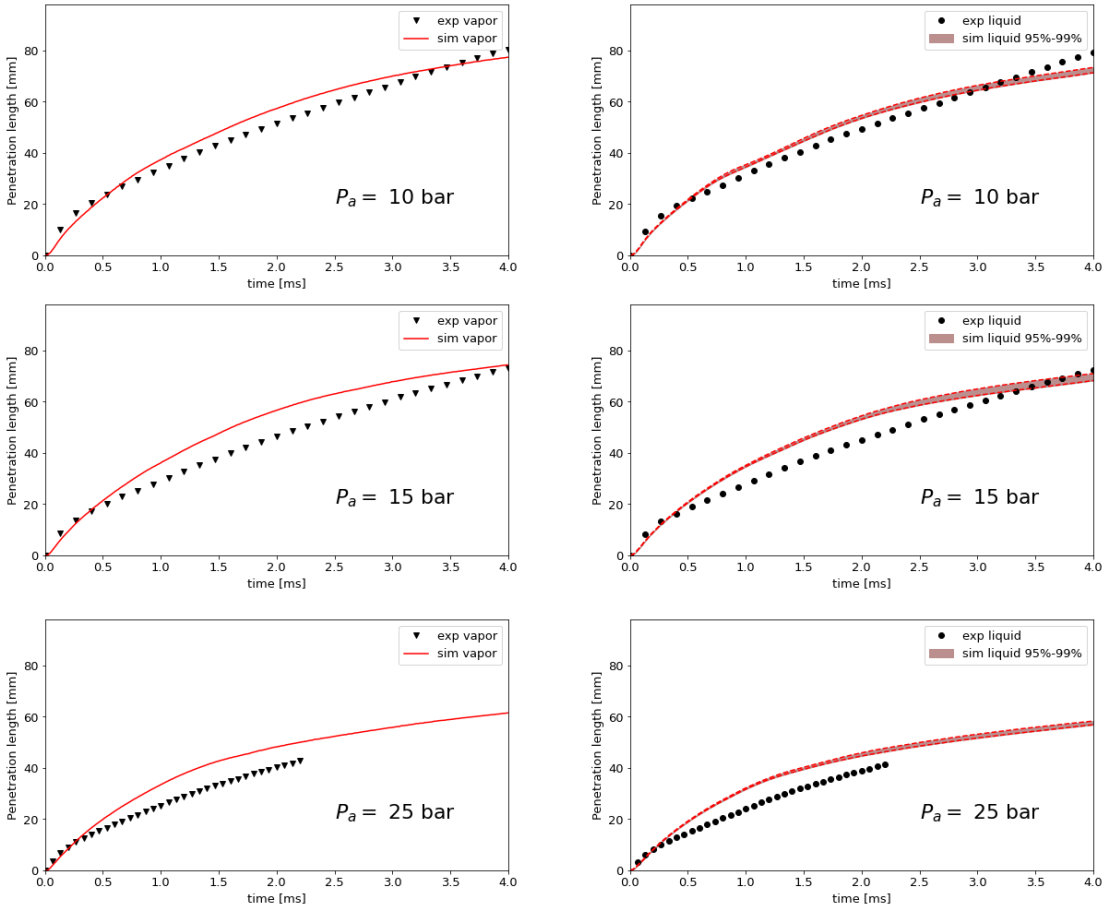

Figure 36: Vapor (left column) and liquid (right column) penetration length for chamber pressures of 10, 15 and 25 bar. Experimental values from [31].

Droplet size

Figure 37 compares droplets from the measuring plane, measured at 2 ms, to the experimental values in the middle of the spray. The 4 bar conditions are considered with two different breakup parameters, and as expected, the GDI flash constants result in the smallest droplet size. It is seen that there is a substantial discrepancy between experimental and numerical results. The predicted droplet sizes are generally too small, and the largest deviations are observed for the high and low pressures. Even though it is uncertain how comparable the numerical and experimentally obtained droplet size is, it is apparent that the trend is not captured. The experimental droplet sizes increase with the increasing pressure, whilst for the cases where the standard KH-RT constants are applied, the opposite effect is observed. This difference in droplet size between experimental and numerical was also encountered by Pandal et al. [38] and could indicate the need for adjustment in breakup model parameters.

Summary

For the superheated sprays where $\frac{p_a}{p_s} < 0.5$, the penetration lengths are significantly underestimated. Changing the RT breakup to increase droplet size does not increase VPL for the superheated conditions. The shape is however reasonably captured for these conditions. Under subcooled conditions, the main spray characteristics shape and penetration are reasonably reproduced, showing the most accurate agreement in terms of penetration during the initial phase of injection. However, some discrepancy in penetration arises during the middle phase of the injection, and this discrepancy becomes more prominent as backpressures increase. The best results for subcooled sprays are positive, as they have the highest relevance in practical applications. Nevertheless, the model fails to replicate droplet sizes for these conditions accurately.

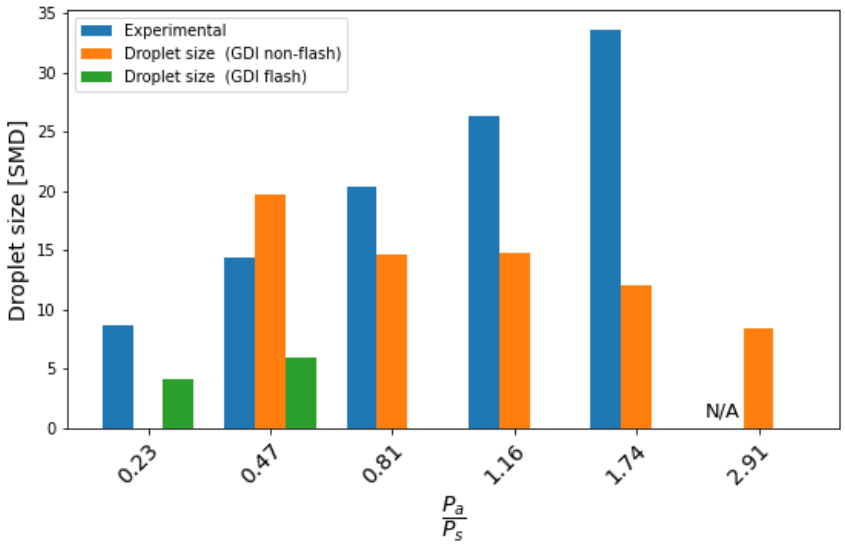

Figure 37: Droplet size in measuring plane compared to experimental values as described in Figure 11. The numerical values are obtained at 2 ms.

The accuracy and reliability of the results are subject to limitations from the measurement method and model assumptions in this study. One aspect is that the length measurement is not accounted for the length travelled off-axis, which results in slight overpredictions for the subcooled cases. Model assumptions like neglecting the step hole geometry and the simplified nozzle configuration are also a source of uncertainty. The simplified injection geometry could result in some under-prediction of penetration length, as shown previously in the section. The initial conditions for the spray also contribute to the uncertainty. Due to limited data, the same initial velocity (same mass and C_d) were used for all conditions, and the reduction in pressure difference over the injector has been neglected. The initial velocity of parcels may have been set too high for the higher pressures, resulting in overpredicted penetration lengths. Additionally, some uncertainty is associated with the experimental measurements.

From a numerical standpoint, grid independence has not been considered, but the mesh size is based on recommendations based on grid independence studies for different injections, is deemed sufficiently accurate. Also, the other numerical studies of sprays from Pelé have all utilized similar or coarser mesh. The number of parcels injected is based on a grid independence study on a shorter injection but with a substantially higher initial parcel velocity and only one nozzle. As the case involves a lower initial velocity and multiple nozzles, the number of parcels injected is assumed to be sufficiently large.

4.5.3 Different breakup

To address the significant deviation in droplet sizes experienced for the higher pressures. Different sets of breakup parameters were considered for the case with an ambient pressure of 15 bar. The effect on both major and minor characteristics was considered. The other numerical studies on liquid ammonia sprays inspired the breakup parameters. One inspired by Li T et al. (and Zhou et al) [27][7], and one by Pandal et al. [38]. The parameters not stated are assumed to be the same as for GDI non-flash. For the Pandal setup, it is assumed that the modified KH-RT model without RT length is used (also tested with breakup length and constant set to 0 and B1/2 results for these setups gave a smaller droplet size in the plane after 2 ms). In addition to these, another set inspired by Li T but with a reduced $B1$ and RT length constant. The parameters can be seen in Table 10. The simulation for the Li parameters did not fully converge and stopped after 3.5 ms.

Penetration lengths for the different breakups are shown in Figure 38. The modified parameters behave similarly to the other two and thus are omitted. The new breakup parameters are in

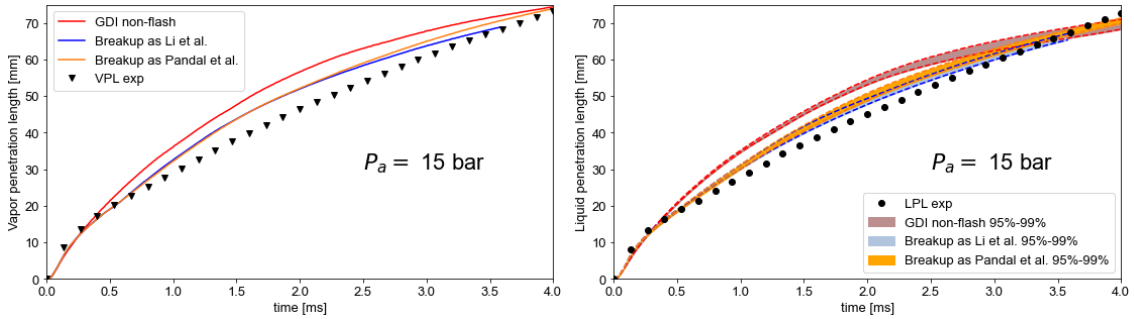

Figure 38: Different breakup effect on penetration lengths for vapor (left) and liquid (right).

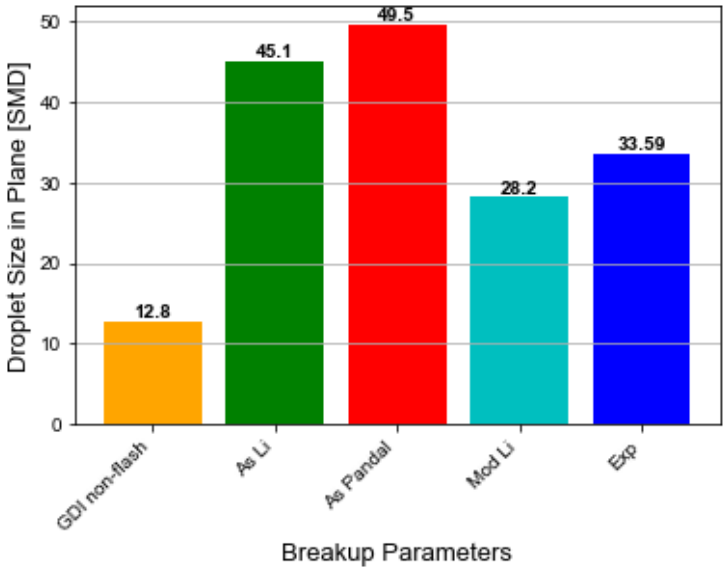

Figure 39: Effect of various breakup model setups on droplet size in measuring plane. The different model constants can be seen in Table 10.

better agreement with the experimental penetration for both liquid and vapor, and a decrease in the curvature of the graph is observed. However, there is still some overestimation present in the results for the middle part. The droplet size measured in the plane after 2 ms is illustrated in Figure 39. Both the setups from the literature achieve larger droplets. Indicating that the $B1$, the KH time constant, is the reason as, the other parameter that has been changed, C_{rt}, is changed opposite for these two. The modified setup, with a lower $B1$ value, is in better agreement with the experiment. Based on this, an increase in the $B1$ parameter is likely required to improve the results regarding both penetration and droplet size. The impact on the shape has not been considered in this brief analysis. Consequently, there is a possibility that the obtained results may no longer correspond to the experimental shape.

4.5.4 Reduced initial velocity

Due to limited data regarding the injection, all simulations earlier were set up with the same initial droplet velocity, i.e. same mass and discharge coefficient. As the backpressure increases, the theoretical mass flow through the injector decreases, as seen from Equation 27. Using the same initial velocity is probably a good approximation for more minor changes in the backpressure. Still, for higher backpressures, especially since the injection pressure here is so low, it is anticipated that overestimation of the initial velocity will occur. Especially for the ambient pressures of 15 and 25 bar is this more significant and could explain some of the overpredictions in penetration. In this section, the discharge coefficient is kept constant while the mass is reduced based on Equation 27,

this result in injection pressure from the spray rate calculator (eq. 28) close to $P_{inj} - P_a$. It should be noted that this is a simplification as also discharge coefficient changes with conditions. However, it illustrates the approximate magnitude of the potential overprediction in the results in Figure 36. Figure 40 shows the reduced velocity profiles.

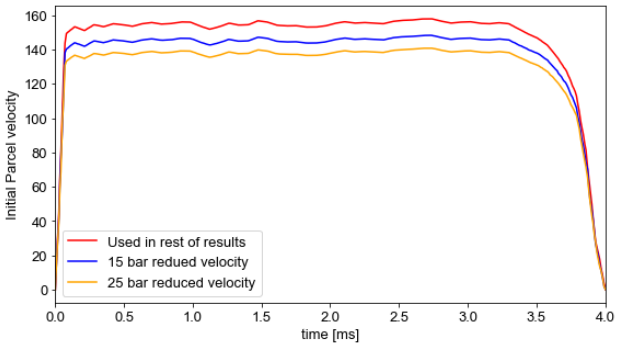

Figure 40: The reduced initial velocities based on the reduction in pressure difference over the injector.

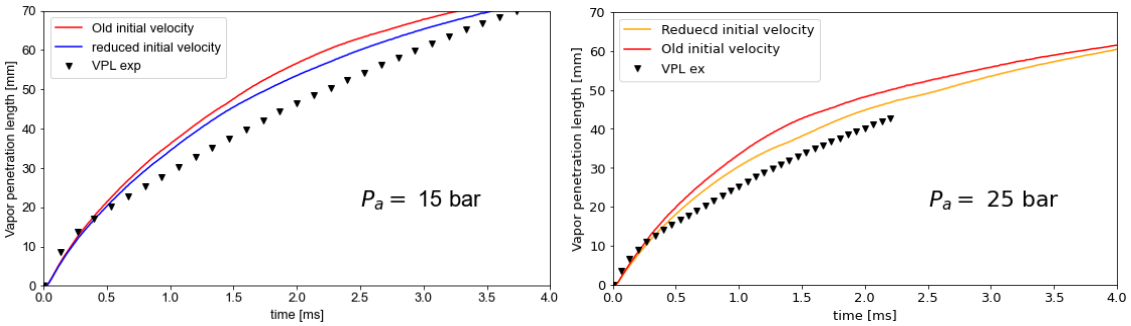

Figure 41: Reduced initial velocity effect on Vapor penetration length for the ambient pressure conditions 15 and 25 bar.

The effect on penetration length was the same for liquid and vapor; hence only vapor is shown. This is presented in Figure 41. The observed penetration lengths are noticeably lower with the reduced velocities, and the effect is more pronounced for the 25 bar case. This leads to better agreement with experimental data, although the curvature of the graphs still doesn't align and results in overprediction in the middle of the spray duration. Some of the overpredictions observed in Figure 36 can thus potentially be explained due to the initial conditions, although the difference for the 15 bar case is not significant. The initial velocities change had a negligible effect on the spray shape. This suggests that backpressure must be accounted for when modelling GDI sprays with unknown injection parameters when setting up simulations for different conditions. Neglecting the ambient pressure when calculating the initial droplet velocity, as done in the spray rate calculator, could be a reasonable approximation for diesel injections characterized by high injection pressures. However, this approach is less suitable for GDI injections, where the ambient pressure has a more pronounced impact on the total pressure difference.

5 Application of spray modelling in engine

In this section, sprays are modelled in an engine simulation model with combustion. A parametric study is conducted investigating the effect of different injection timings for ammonia and the orientation of the diesel injector on engine performance and emissions. This section aims to show the application of the spray simulations conducted earlier and the importance of the spray setup on engine modelling. The author has not developed the numerical engine model, and the current contributions involve.

- Selecting injector configurations and injection timings to consider.
- Set up liquid ammonia spray simulations based on thermodynamic conditions and injector design.
- Running the simulations.
- Preliminary combustion analysis - identity favourable injection strategies.

First, the engine in the model is introduced. Then the simulation setup is described. Finally, the results are presented together with a brief analysis. The engine's performance is complex, and in this analysis, only some key parameters are assessed, thus only providing a limited perspective of the overall pictures. However, it could still provide valuable insight and help set up experiments in the research engine in the lab.

5.1 Engine case description

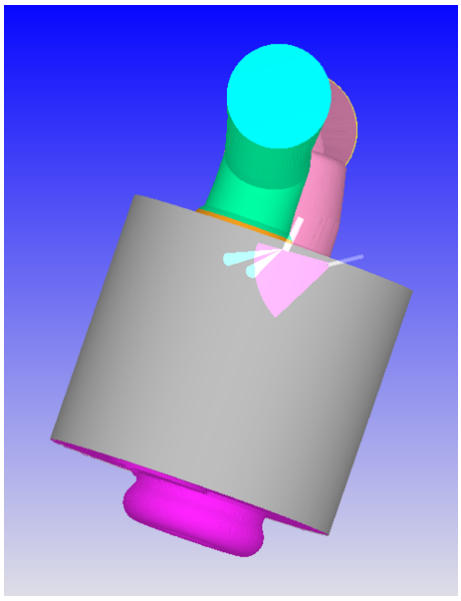

Figure 42: Engine model with modified diesel injector (blue nozzles) and retrofitted GDI injector (pink nozzles). The injector configurations correspond to the first configuration.

The engine is a single-cylinder Hatz 1B30 Diesel (CI) engine model from the EPT motor lab at NTNU and is a 4-stroke engine with a bowl-in-piston design. It has been retrofitted with a GDI injector for the injection of ammonia fitted at an angle as seen in Figure 42. The diesel is injected with a high-pressure common rail injector which is modified by welding shut 4 out of 6 holes due to the decreased diesel mass flow in dual fuel operation. The ammonia is pressurized up to 200 bar for injection by a nitrogen bottle. The use of a GDI injection system for ammonia in this engine is partially driven by practical considerations. Using a GDI injector for ammonia enables precise

control of the fuel injection and reduces the need for high injection pressures, thus eliminating the need for a high-pressure pump. This simplifies the system and is also an advantage due to the corrosive properties of ammonia. Selected characteristics of the engine are presented in Figure 13.

The operating point is based on an experiment run in the lab and operates at a speed of 1780 rpm. The start of injection (SOI) for diesel injection occurred at 15.5 crank angle degrees (CAD) before Top Dead Center (bTDC). For ammonia injection, the SOI was set at 19.14 CAD bTDC. The injection duration was measured to 17.7 CAD (1.66 ms) for diesel and 18.2 CAD (1.7 ms) for ammonia, and the mass per cycle was estimated to be 9.54 mg and 27.3 mg for diesel and ammonia, respectively. When considering the energy per cycle using the Lower Heating Value (LHV), this corresponds to 425.5 J and 507.8 J, for diesel and ammonia, resulting in a total of 933.3 J of supplied energy per cycle. Meaning that the ammonia content is 54 % on energy and 74% on a mass basis. The calculations are based on the lower heating values of 44.6 and 18.6 MJ/kg for n-Heptane (surrogate fuel used in simulation) and ammonia, respectively.

Table 13: Selected engine characteristics [40].

Parameter	-
Bore	80 mm
Stroke	69 mm
Displacement	347 cm^3
Compression ratio	21.5
max power	5 kW
max Torque	16.2 Nm
Inlet valve opening	-100 CAD
Outlet valve opening	100 CAD

5.2 Injection timing and nozzle configuration

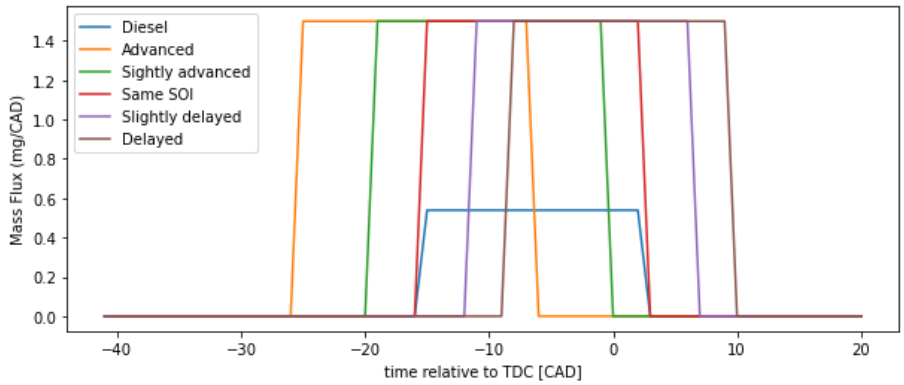

Figure 43: Average mass flux for diesel and ammonia for the various injection timings for ammonia. The injection rate profiles used in the model are based on experiments and have a more complex shape.

Five different injection timings for ammonia were considered, and to reduce the number of variables, the diesel injection timing was kept constant. All of the considered ammonia injections are close to diesel injection, which is considered the most promising from the literature review. Two before diesel injection named advanced and slightly advanced with the start of injection at -25 CAD and -19.14 CAD, respectively. Allowing more time for fuel to mix. One with the same SOI as diesel at -15.5 CAD and two after with the slightly delayed starting at -11.85 CAD and delayed at -8.22 CAD. Figure 43 shows the different injection timings compared to the diesel injection. The mass flux in the figure is the average over the injection to show the difference in the order of magnitude for the two injections. In the model, the mass flow is set to vary in time based on experimental profiles. The injection of ammonia after diesel is the most considered approach in

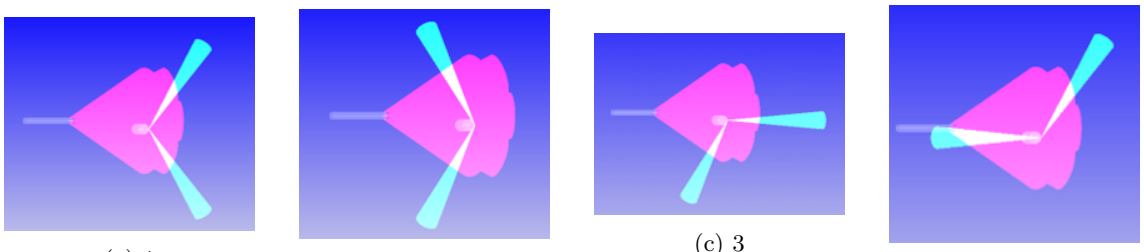

(a) 1 (b) 2 (c) 3 (d) 4

Figure 44: The different configurations of the diesel injector considered, seen from the top. The direction of the diesel nozzles is shown in blue.

the literature, but the cases here differ from these of HPDF due to the long duration and size of the diesel injection. Also, the injection pressure of ammonia is higher for the HPDF approach. All the considered injection timings significantly overlap with the diesel injection, as seen in the figure.

Table 14: Different for injection timings of ammonia and the thermodynamic condition of the liquid ammonia.

-	Advanced	Slightly advanced	Same as diesel	Slightly delayed	Delayed
SOI	-25 CAD	-19.14 CAD	-15.5 CAD	-11.86 CAD	-8.22 CAD
$\frac{P_a}{P_s}$ (T_f=293 k)	2.14	2.91	3.51	4.13	4.68
$\frac{P_a}{P_s}$ (T_f=338 k)	0.62	0.85	1.02	1.20	1.36

The degree of superheat is calculated based on the pressure in the engine at the different injection timings. For a fuel temperature of 293 K, what is considered here, all injection timings are severely subcooled, as seen in Table 14. The two advanced injections are within the range of pressure ratios considered in Part 2. The calculations are repeated for a higher fuel temperature to show the effect on conditions. By increasing the fuel temperature to 338 K, two of the injection timings would be superheated for the ammonia.

Four different configurations of the modified diesel injector have been considered to examine the effect of interactions between sprays and directions of sprays. In configuration 1, seen in Figure 44, the diesel nozzles point in the same direction as ammonia injection. This configuration is currently fitted in the engine. For number two, the direction is pointing in the opposite direction. The injector is rotated 60 degrees clockwise from the initial two configurations for configurations three and four.

5.3 Simulation setup and combustion modelling

A brief explanation of the simulation setup and how the combustion process is modelled is presented in this section. As I have not been building this model and the engine modelling is not directly relevant to this thesis, the model setup and theory behind the combustion modelling are not explained in detail. The simulation setup employed here is similar to that used by Lewandowski et al. [78][40].

The software and numerics employed in the modelling are the same as were utilized for the spray simulations. In the engine model, N-heptane is employed as a surrogate fuel to simulate the combustion behaviour of diesel. The mesh size is also the same as for the spray simulation, i.e. 2 mm with refinement to 0.25 mm with AMR based on velocity gradients. The moving parts in the engine are thus handled by creating a new mesh for each time step. Here, liquid and wall Interaction is encountered, and this is handled with a wall film model by O'Rourke [81]. To model the combustion process, the SAGE combustion model [41], a detailed chemistry kinetics solver, is applied. This approach is based on the fact that chemical kinetics are most important to resolve in the combustion process and have a greater impact than turbulence.

By solving the governing equations presented in section 3.3, the mixing of the flow field (mass, momentum, energy, species) is resolved, and the thermodynamic properties, pressure, temperature and composition, are obtained for each cell. The detailed kinetics solver solves then for the change of species concentration and calculates the heat release in the cell, and is coupled with the governing equations for species and energy. Chemical kinetics is solved using input files containing chemical mechanisms and thermodynamic data, which are essential for accuracy. The chemical reaction mechanism file contains elementary reactions that together form an overall chemical reaction. Here a reduced (less computationally expensive) chemical kinetics scheme by Xu et al. [82] is used to handle the combustion of ammonia and the surrogate N-heptane. The reaction file consists of 69 species and 389 reactions. To reduce the computational cost, cells with similar temperatures and species compositions are solved together based on average cell values. The model assumes that each cell is treated as a well-stirred reactor and chemical reactions occur with constant volume.

5.3.1 Spray setup

Table 15: Injector and injection characteristics for the ammonia injection.

-	Constant volume chamber injection [4]	Injection in engine
Orifice diameter	150 µm	227 µm [35]
Step diameter	365 µm	453 µm [35]
Nozzles	7	6 [35]
Drill angle	46°	38° [26]
Inj. mass	40 mg	27 mg
Inj. duration	4 ms	1.7 ms
Inj. Pressure	120 bar	200 bar
Fuel temperature	293 K	293 K

The ammonia spray setups are based on the degree of superheating and are also adjusted to fit the injector in the engine. The injector and the injection differ from those considered in earlier results, and some assumptions are made. Selected characteristics of the two injectors and injections can be seen in Figure 15. The input angles have been changed to account for the difference in spray characteristics. The cone angle is obtained in the same way as in Part 2. However, the plume angle is decreased. The angle near the injector is approximately 71° for the higher pressures in Pelé's study, as seen in Table 12. This is assumed to apply to even higher pressures. This angle is scaled to fit the new injector with the relation between the drill angles for the two injectors, and then the corresponding input angles are calculated from Equation 46. This results in a plume direction angle of 19°. How good this assumption is not known, as injector angles are just one of many parameters that differ between these cases. To obtain the initial droplet velocity, the discharge coefficient is set to set to 0.48. This is what was reported by Bjørgen et al. [46] for the same injector, with an injection pressure of 200 bar and a backpressure of 20 bar ($\frac{P_a}{P_s} = 2.3$). This also corresponds well to the injector pressure using the spray rate calculator in the software. The simplification that the initial droplet velocity is the same for all the injection timings has thus been made. Table 16 summarises the injection parameters applied.

Due to the severely subcooled conditions for all injection timings, the submodels for the spray physics are set up the same as for the subcooled cases in the result part 2 (Table 11). As seen from Table 14, preheating of the fuel changes superheat degrees completely and would require a different setup, especially for the input angles. The spray simulations from the last section were validated for temperatures much lower than what is occurring under actual engine conditions. Also, the injector is of another kind. However, sprays with the same order of superheating were considered. The injections in the engine are much shorter and will also hit the piston after approx 30 mm for slightly advanced injections. Since a reasonable agreement with the experimental data was experienced for the start of the injection, the spray modelling is considered sufficient for preliminary results and to "tell about the trends". It could be valuable for setting up future engine experiments in the real engine. The engine simulations were conducted for an engine cycle from the intake stroke at -360 CAD to the exhaust valve opening at 100 CAD after TDC.

Injection model	Blob w/ parcels evenly distributed
Discharge coefficient	0.48
Mass rate-shape	ECN spray A [61]
Cone angle	20.5°
Plume direction angle	19°

Table 16: Injection parameters for ammonia spray in the engine.

5.4 Result and discussion

First, the engine simulation was run with the injection strategy as in the experiment, i.e. configuration one and slightly advanced ammonia injection. Three different sets of spray angles were employed while keeping all other parameters constant. This was done to examine the impact of different input angles on the simulation results and to validate the model. Pressures and heat release rates were used when comparing the simulation and the experiment. Then the combustion characteristics of the different injection strategies were examined by looking at heat release rates and fuel burnout. In addition, the peak pressure and nitrogen emissions were considered. This analysis aimed to identify favourable injection strategies.

5.4.1 Effect of different input angles

The three sets of angles considered are presented in Table 17 and consist of the pair scaled to the injector as described previously, the angles used by Lewandowski et al. in the CPOTE paper [40], where the input angles are set to match the narrower spray angle measured at half penetration. Furthermore, input angles without considering the difference in injectors. The last set results in a plume direction angle that exceeds the injector's physical drill angle by a significant margin.

	Scaled to Injector	CPOTE angles [40]	Not scaled
Cone angle [°]	20.5	10.96	20.5
Plume direction angle [°]	19	13.53	25.5

Table 17: Different injection angles considered.

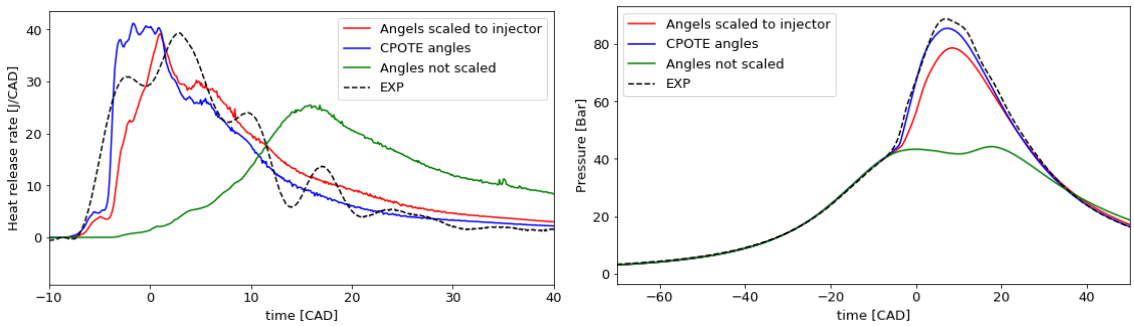

Figure 45: Heat release rates (left) and in-cylinder pressure (right) with the different angles. Injector configuration number 1, and the start of ammonia injection at -19.14 CAD.

Figure 45 shows the heat release rate and in-cylinder pressure for selected simulation time periods. The experimental measurements from the lab are included with a dotted line. Compared to the experiment, the first two sets of angles replicate the ignition delay well and show agreement in the order of magnitude of the peak in HRR. However, the shape of the heat release rate curve is not accurately captured for either, and a significant deviation in behaviour is seen. Regarding the pressures, both simulations result in underpredictions. But the CPOTE angels are in better agreement with the experiment. The superior result with the CPOTE angles could indicate the plume angle of 19° leads to a too wide spray and that angles should be scaled even further. Unfortunately, experimental data were only available after running the rest of the simulations,

and other angles were not considered. Although it is not a perfect match, the simulation with the reduced chemical kinetics scheme can capture some of the critical characteristics of the combustion process.

The last set of angles yields completely different characteristics, and the fuel does not seem to ignite properly, which can also be seen from the pressure curve where the pressure is low through expansion. This may indicate that for these wide angles, the sprays from the different injectors interact, and the ammonia inhibits the ignition of the diesel. This behaviour was experienced by Scharl et al. [28] when ammonia was injected first, and the sprays were interacting.

Here only one aspect of the spray modelling is considered, the input angles, but the significant difference in results still shows that spray modelling is critical for engine simulation. For setting up engine simulations in the future, sprays modelling should be validated first. If the spray is modelled accurately, the number of unknowns can be reduced. Opposite, if the spray is modelled inaccurately/wrong and another parameter is adjusted for the engine simulation to match experimental data, a reliable and robust model cannot be achieved, leading to trouble and bad results.

5.4.2 Different injection strategies

Heat release rates from the experiment were not accurately captured for the operating point considered above. There could be several explanations, such as using N-heptane instead of diesel fuel, inaccuracies in the spray and mixing modelling, and inaccuracies in the combustion modelling (chemical kinetic scheme, grid size, etc.). Still, the model is considered good enough to examine differences in behaviour for the different injection strategies considered.

Figure 46 shows the heat release rates for all cases considered from -10 CAD to 40 CAD after TDC. For the ammonia injections starting after the diesel injection (-11.86 CAD and -8.22 CAD), the graphs are characterised by the premixed combustion phase for all configurations. And the combustion regime is characterised by a distinct peak early in the HRR. Ignition can be seen to occur around -5 CAD with a small peak beforehand, representing low-temperature combustion. The ammonia is thus injected before the diesel ignition for all considered timings. The rapid combustion peak indicates that a considerable amount of mixing has occurred during the ignition delay period and that this happens independently for all the injector configurations. And as this behaviour becomes more distinct with later injection, it indicates that the increased temperature and the lower amount of ammonia injected increase the evaporation and mixing. It also indicates that the combustion is mainly diesel. For these two late injections, the diagram is similar, with slight differences in the premixed peak and the mixing-controlled combustion phase depending on the configurations where configuration 4, the only with direct interactions between the sprays as seen in Figure 47, having the lowest premixed peak.

For the earlier injections (-25 CAD, -19.14 CAD and -15.5 CAD), the location of the diesel injector is crucial for the combustion behaviour, and the regimes are utterly distinct based on injector configuration. For configurations 1 and 4, mixing is delayed, and less premixed combustion can be seen. After ignition, the HRR speeds up due to better mixing from rapid evaporation, resulting in a wider and delayed mixing-controlled combustion peak. For configurations 2 and 3, where at least one nozzle is pointing in the opposite direction of the ammonia spray, a distinct premixed peak is observed. For configuration 3, diesel is injected into both areas with ammonia and not, and two separate combustion phases are observed.

For the earliest injection (-25 CAD), no proper ignition is seen for configuration 1, and the ignition is significantly delayed for number 4. This timing stands out as all the ammonia is injected before the earliest diesel ignition at approximately -5 CAD. This timing leads to two distinct peaks in HRR for configuration 2, meaning that the mixing-controlled combustion is happening at a very high rate. For the later injections, ammonia enters the chamber also after ignition, and a much lower HRR characterises the mixing-controlled combustion for this configuration.

Injecting the diesel in the same direction as the ammonia thus gives rise to little combustible mixture during the ignition delay. The presence of ammonia has a deteriorating effect and leads to inadequate mixing. A possible explanation is that the fuel deposits on the wall and limited

evaporation occurred before ignition. From Figure 47, it can be seen that the liquid ammonia hits the wall and accumulates. The significant cooling impact of ammonia, resulting from its high latent heat of vaporisation, is believed to have a crucial role in the situation, causing a delay in the evaporation of diesel. Furthermore, this lack of combustible diesel/air mixture also delays and inhibits diesel ignition, as observed for the earliest injection timing. Another aspect that could affect the mixing is the difference in turbulence. When nozzles are oriented in opposite directions, enhanced mixing is anticipated due to a rise in turbulence.

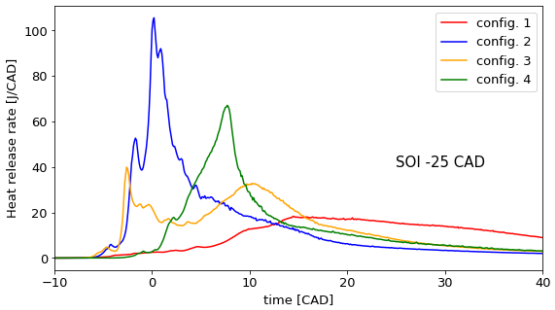

(a) Advanced ammonia injection.

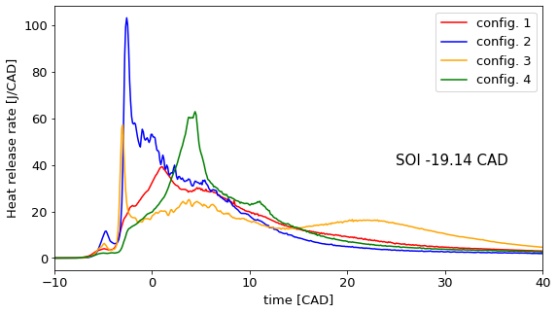

(b) Slightly advanced ammonia injection.

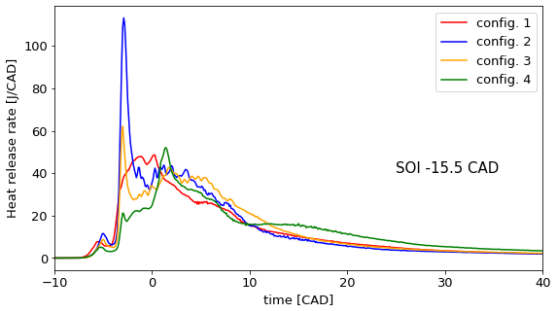

(c) Same as diesel.

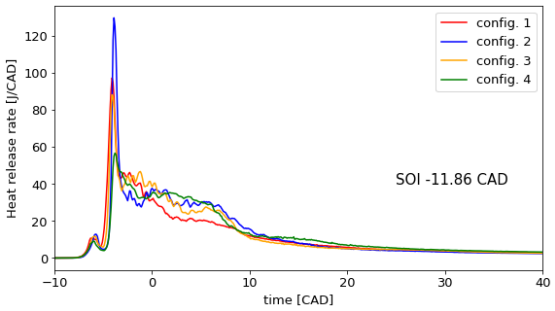

(d) Slightly delayed ammonia injection.

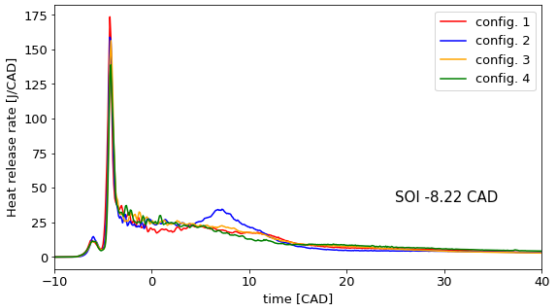

(e) Delayed ammonia injection.

Figure 46: Heat release rate for the various injection timings of ammonia and configuration of the diesel injector.

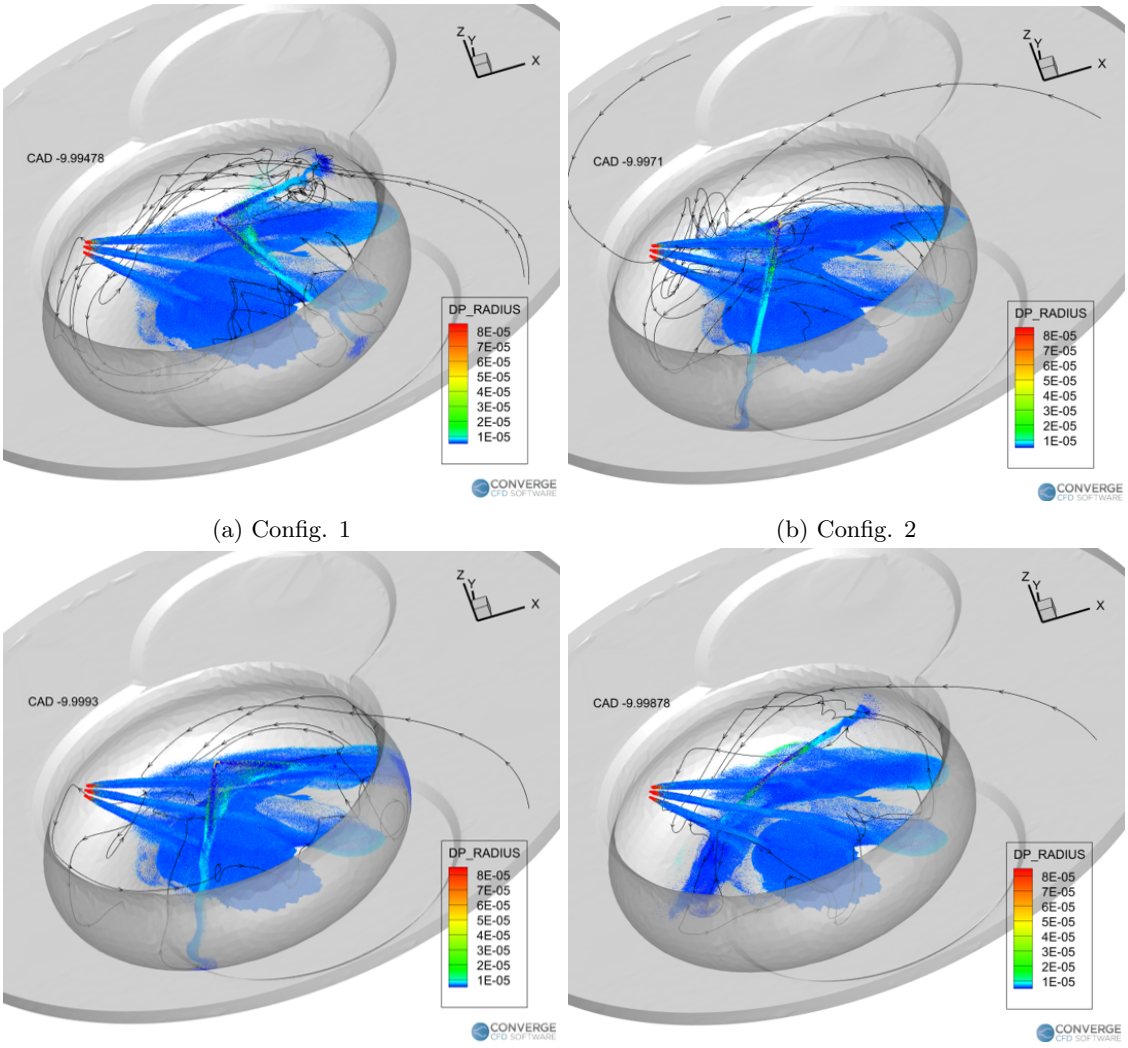

(a) Config. 1

(b) Config. 2

(c) Config. 3

(d) Config. 4

Figure 47: Different diesel nozzle configurations shown at -10 CAD for the case where both injections start at -15.5 CAD. The black streamlines show the counter-clockwise swirl of the gases in the cylinder bowl.

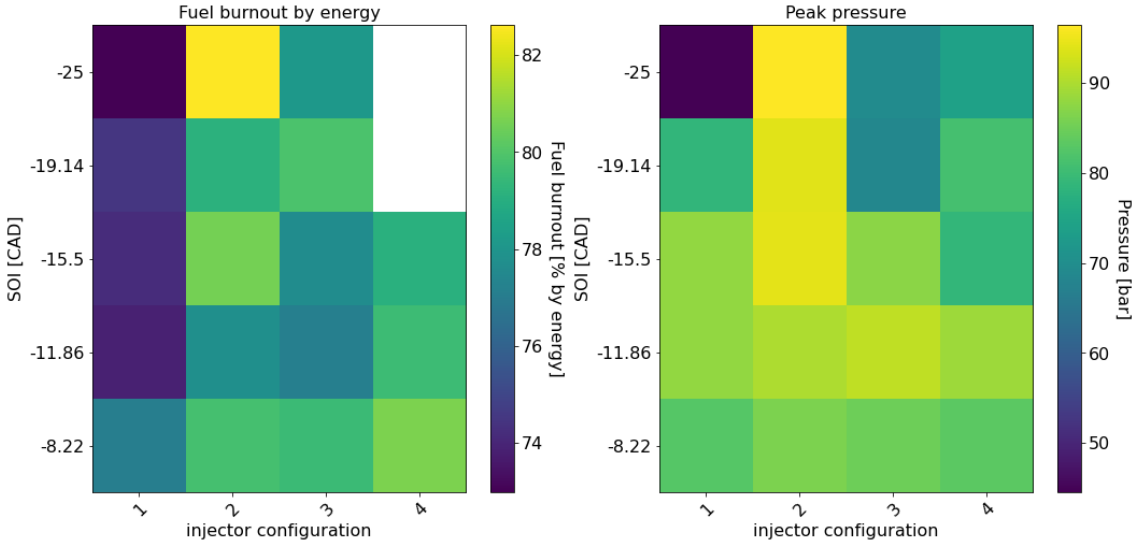

Figure 48: Burnout rate by energy (left) and peak in-cylinder pressure (right) for the various injection timings of ammonia and configurations of the diesel injector.

A summary of the two key parameters, burnout and peak cylinder pressures, is presented in Figure 48. The two early injections for configuration four did not fully converge, and thus the results at the end time at valve opening were not achieved. Burnout is calculated by dividing the integrated heat release rate by the supplied energy to the engine. In this graph, the burnout for both fuels is considered simultaneously. The graph shows that low burnout is achieved in the current configuration, where diesel is injected in the same direction as ammonia. As expected, the lowest value is found for the earliest injection timing where ignition is inhibited. The two highest burnouts are found for configuration 2. Apart from this, the latest injections, -8.22 CAD, with configurations 2,3 and 4, and the three latest timings for configuration 4 also stand out. Furthermore, configuration 3 with the injection timing -19.14 CAD also looks promising regarding burnout. However, from Figure 46, it is evident that some of the contributions to the high burnout are due to the elevated HRR late in the combustion, and this case is in fact not particularly good, which is reflected in the low pressure in Figure 48. In the pressure matrix, it is seen that configuration two yields the highest values also in terms of peak pressures, and they are found for the three earlier injection timings. Excluding configuration 2, the two injection timings, -11.86 CAD and -15.5 CAD, generally have the highest peak cylinder pressures. Lower pressures and amplified variations are observed for the earlier injections, reflecting the significant difference in combustion behaviour presented earlier. This variety is also seen in the nitrogen emissions in Figure 49. Considering only nitrogen emissions, the injection strategy where both fuels have the same SOI and configuration one is applied one of the best, with some of the lowest values of both N_2O and NO_x. However, this injection case exhibits low fuel burnout.

This brief analysis shows that configuration two and the early injection timings of ammonia are the most promising, with the earliest injection timing the superior. This also applies to NO_x emissions; however, this is not true for N_2O. If the emissions of N_2O are to be strongly emphasized, the two latest timing with configuration 4 is promising as these cases emit low levels of N_2O and at the same time exhibit high peak pressure and burnout. Configuration 4 has one nozzle that directly interacts with the ammonia spray, as seen in Figure 47. These cases are thus partially in accordance with what Scharl et al. [28] and Zhou et al. [7] found to be best, i.e. injection of diesel first and interaction between the sprays. More interactions between plumes for the late injections would be interesting to explore and are expected to have a less pronounced premixed peak and a more comprehensive mixing-controlled combustion phase. On the negative side, the latest injections for configuration 4 demonstrate some of the highest levels of NO_x emissions.

This analysis has not considered other diesel injection settings, which would be worth investigating. Advancing the diesel injection were found to increased the burnout of NH_3 for Zhou et al. [7] and would be interesting to explore here. Additionally, investigating the potential of shorter diesel

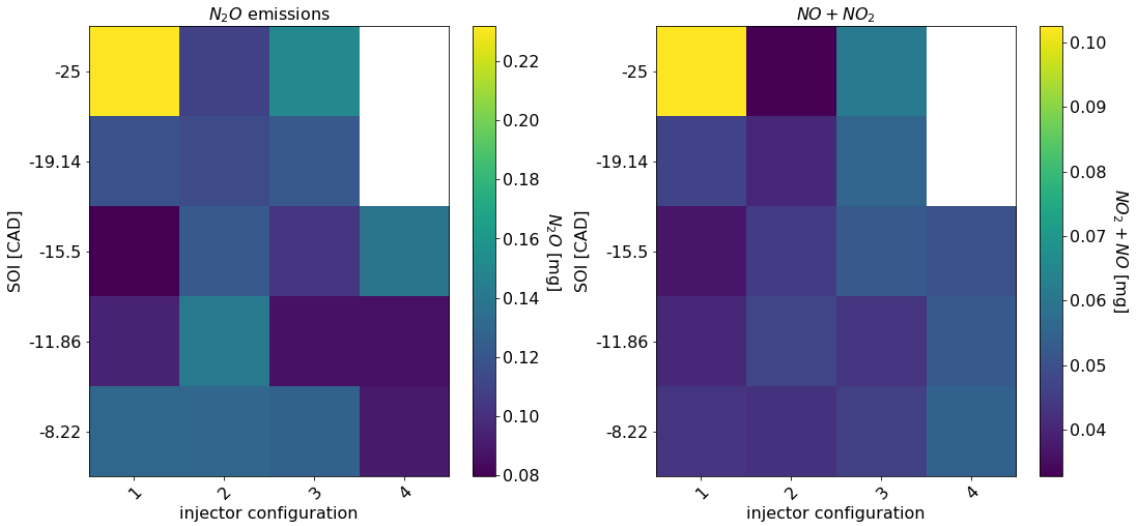

Figure 49: Nitrogen emissions from the engine simulations, N_2O left and NO_x right. NO_x is calculated as the sum of NO and NO_2.

injections to enhance ignition and smaller diesel injections to reduce the premixed combustion stage and reduce carbon emissions would also be of interest.

The small analysis conducted here only considers a few parameters and thus tells only a tiny part of the whole picture regarding engine performance, as this is complex. E.g. as shown previously, high burnout could come from late combustion phases and does not necessarily indicate a positive outcome. Additionally, the result has significant uncertainty as HRR and pressure from the experiment were not accurately captured. The remarkably high premixed peaks could potentially suggest weaknesses in the reduced chemical kinetic scheme.

6 Conclusions

In this thesis, simulations of liquid ammonia spray from multi-hole GDI injectors were carried out. The multiphase flow of the spray was handled with the Eulerian-Lagrangian approach and solved using the finite volume method with the software Converge 3.0. The aim was to accurately reproduce ammonia spray characteristics under multiple thermodynamic conditions, both with and without flash boiling. Through a literature review and parametric studies, appropriate models and injection parameters were chosen to account for the spray development processes and the effects occurring within and near the nozzle under various conditions. First, attempts were made to reproduce spray characteristics from an experiment conducted in a constant volume chamber [31]. Then, spray simulations were set up within an engine simulation framework with combustion. The engine simulations aimed to evaluate the combustion of various injection strategies in a dual-fuel engine, including different injector configurations and injection timings for ammonia, to identify favourable injection strategies. The primary contribution of this thesis was a method for applying input angles under various conditions based on experimental data. The main conclusions drawn from the study are:

- Spray shape with the characteristics collapse of plumes into a single body was reasonably captured under strong flash boiling conditions. However, neither the liquid nor vapor penetration lengths were not accurately reproduced. A significant underestimation was observed, and after approximately 1.7 ms, an unrealistic and highly exaggerated increase in penetration was encountered for the most superheated condition. For strong flash boiling conditions, further model development is needed to handle the flash boiling effect on the vaporization and breakup of droplets.
- For subcooled conditions, shape was also reasonably captured, and better agreements were found for the penetration lengths. Nonetheless, some overprediction in penetration was experienced after a certain period after the start of the injection. This discrepancy increased with higher chamber pressures, and some of the inconsistency could be attributed to assumptions made in the injection modelling.
- Characteristics on the smaller scale were not well replicated, and the obtained droplet sizes differed greatly from the experimental values for the subcooled sprays. The need for modifications in breakup model parameters, specifically the initial KH breakup, was suggested to improve the accuracy of the model under subcooled conditions.
- The effect of different input angles in spray modelling on engine simulations was demonstrated, emphasizing the importance of the prescription of input parameters and accurate spray modelling.
- For early injections of ammonia when the pilot fuel diesel is injected in the same direction, the ammonia was found to have a deteriorating effect on the mixing process and low burnout and delayed ignition was encountered, which may be attributed to the cooling effect of ammonia evaporation. The best outcomes were observed for the earlier ammonia injections with the diesel injection pointing in the opposite direction.

7 Future work

Future work on this topic should include:

- Further model development on flash boiling ammonia sprays, which includes the implementation of a model to account for the thermally induced breakup. This can be added as a user-defined function in Converge as done by Shin and Park [50] and Duronio et al. [57]. Moreover, there is a need for additional improvements in the vaporization models, specifically targeting the augmentation of size reduction during the initial phase and reducing size reduction in the subsequent stages.
- Calibrating parameters in the KH-RT breakup model to get more accurate results for the subcooled cases regarding local droplet size and penetration lengths, with a particular emphasis on the KH breakup. Based on the preliminary analysis of breakup parameters, it appears that increasing the time constant $B1$ leads to improved results. However, alterations in other parameters, such as C_{RT}, should also be considered.
- Also consider ammonia sprays under higher temperatures to see how the current model setup performs in such scenarios. In the experiment by Pelé [31], sprays for ambient temperatures of 80° C and 120° are also available and can be used for this purpose. Ultimately, conditions with pressure and temperature as under engine-relevant conditions near TDC are of interest. Additional experiments are necessary to explore these conditions with GDIs, as currently, only an experiment with a single-hole diesel injector is available for such conditions [27].
- Future spray validation studies should also take into account the direction of the plumes when comparing sprays to experimental data, i.e. only consider penetration along the spray axis to ensure better comparability with the experimentally obtained penetration lengths. This particularly affects subcooled sprays, where the narrowing effect is less pronounced. Conversely, when a spray experiment is conducted, the distance travelled away from the spray axis is also accounted for in the penetration lengths.
- To obtain a more accurate numerical engine model, additional experimental measurement from the injector in the engine is required. Particularly the spray angles close to the injector, which are vital for choosing the input angles to be incorporated into the model. To validate the model setup, obtaining both the spray angle for full spray and the penetration lengths is necessary. Additionally, experiments that accurately measure the cone angle under various conditions would be valuable. Currently, the cone angle for flash boiling conditions is based on sprays from a diesel injection system and the angles for subcooled conditions are based on uncertain measurements. Furthermore, experimental data for the mass and discharge coefficient for various conditions is also of interest.

8 Acknowledgements

I would like to thank Michal T. Lewandowski for his invaluable guidance throughout the past two semesters.

I would thank Krister Aaen Pedersen for providing the engine simulation setup and Karl Oscar Bjørgen for providing pictures and mass flux measurements from ammonia injections from the EPT motor lab at NTNU.

Manith Randula Attanapola and Kristian Augland are highly acknowledged for providing crucial IT support.

NTNU is acknowledged for granting access to the computing cluster IDUN.

Convergent Science is acknowledged for providing licenses and technical support for the software CONVERGE.

References

1. United Nations Framework Convention on Climate Change. The Paris Agreement. https://unfccc.int/process-and-meetings/the-paris-agreement/the-paris-agreement. 2015. [Accessed on: 2023 Feb 28]
2. Mertens J, Belmans R and Webber M. Why the carbon-neutral energy transition will imply the use of lots of carbon. C 2020; 6:39
3. Veritas DN, Lloyd G and Dnv G. Maritime Forecast to 2050. Energy Transition Outlook 2019 :118
4. Zohuri B. Hydrogen energy: Challenges and solutions for a cleaner future. Springer, 2019
5. Dimitriou P and Javaid R. A review of ammonia as a compression ignition engine fuel. International Journal of Hydrogen Energy 2020; 45:7098–118
6. Toolbox E. Ammonia - Vapour Pressure at Gas-Liquid Equilibrium. https://www.engineeringtoolbox.com/ammonia-pressure-temperature-d_361.html. 2003. [Accessed on: 2023 May 10]
7. Zhou X, Li T, Wang N, Wang X, Chen R and Li S. Pilot diesel-ignited ammonia dual fuel low-speed marine engines: A comparative analysis of ammonia premixed and high-pressure spray combustion modes with CFD simulation. Renewable and Sustainable Energy Reviews 2023; 173:113108
8. Giddey S, Badwal S and Kulkarni A. Review of electrochemical ammonia production technologies and materials. International Journal of Hydrogen Energy 2013; 38:14576–94
9. Ishimoto Y, Voldsund M, Nekså P, Roussanaly S, Berstad D and Gardarsdottir SO. Large-scale production and transport of hydrogen from Norway to Europe and Japan: Value chain analysis and comparison of liquid hydrogen and ammonia as energy carriers. International Journal of Hydrogen Energy 2020; 45:32865–83
10. Wärtsilä. Combustion engine vs gas turbine: part load efficiency and flexibility. Available from: https://www.wartsila.com/energy/learn-more/technical-comparisons/combustion-engine-vs-gas-turbine-part-load-efficiency-and-flexibility [Accessed on: 2022 Dec 19]
11. Afif A, Radenahmad N, Cheok Q, Shams S, Kim JH and Azad AK. Ammonia-fed fuel cells: a comprehensive review. Renewable and Sustainable Energy Reviews 2016; 60:822–35
12. De Vries N. Safe and effective application of ammonia as a marine fuel. 2019
13. Erdemir D and Dincer I. A perspective on the use of ammonia as a clean fuel: Challenges and solutions. 2021
14. Scharl V, Lackovic T and Sattelmayer T. Characterization of ammonia spray combustion and mixture formation under high-pressure, direct injection conditions. Fuel 2023; 333:126454
15. Agency EP. Appendix A to Part 355—The List of Extremely Hazardous Substances and Their Threshold Planning Quantities. Code of Federal Regulations. 40 C.F.R. Part 355. 2019. Available from: %5Curl%7Bhttps://www.ecfr.gov/current/title-40/chapter-I/subchapter-J/part-355/%7D [Accessed on: 2023 Apr 21]
16. IPCC. Climate Change 2022: Mitigation of Climate Change. Contribution of Working Group III to the Sixth Assessment Report of the Intergovernmental Panel on Climate Change. Ed. by Shukla P, Skea J, Slade R, Khourdajie AA, Diemen R van, McCollum D, Pathak M, Some S, Vyas P, Fradera R, Belkacemi M, Hasija A, Lisboa G, Luz S and Malley J. Cambridge, UK and New York, NY, USA: Cambridge University Press, 2022. Available from: https://www.ipcc.ch/report/ar6/wg3/downloads/report/IPCC_AR6_WGIII_FullReport.pdf
17. Nadimi E, Przybyła G, Lewandowski MT and Adamczyk W. Effects of ammonia on combustion, emissions, and performance of the ammonia/diesel dual-fuel compression ignition engine. Journal of the Energy Institute 2023; 107:101158
18. Ryu K, Zacharakis-Jutz GE and Kong SC. Effects of gaseous ammonia direct injection on performance characteristics of a spark-ignition engine. Applied energy 2014; 116:206–15
19. Lhuillier C, Brequigny P, Contino F and Mounam-Rousselle C. Experimental study on ammonia/hydrogen/air combustion in spark ignition engine conditions. Fuel 2020; 269:117448

20. Blarigan PV. Advanced internal combustion engine research. *Proceedings of the DOE hydrogen program review*. NREL/CP-570-28890. 2000

21. Heywood JB. Internal Combustion Engine Fundamentals. Automotive technology series. McGraw-Hill, 1988. Available from: https://books.google.co.in/books?id=O69nQgAACAAJ

22. Yousefi A, Guo H, Dev S, Lafrance S and Liko B. A study on split diesel injection on thermal efficiency and emissions of an ammonia/diesel dual-fuel engine. Fuel 2022; 316:123412

23. Yousefi A, Guo H, Dev S, Liko B and Lafrance S. Effects of ammonia energy fraction and diesel injection timing on combustion and emissions of an ammonia/diesel dual-fuel engine. Fuel 2022; 314:122723

24. Okafor EC, Yamashita H, Hayakawa A, Somarathne KKA, Kudo T, Tsujimura T, Uchida M, Ito S and Kobayashi H. Flame stability and emissions characteristics of liquid ammonia spray co-fired with methane in a single stage swirl combustor. Fuel 2021; 287:119433

25. Ryu K, Zacharakis-Jutz GE and Kong SC. Performance characteristics of compression-ignition engine using high concentration of ammonia mixed with dimethyl ether. Applied energy 2014; 113:488–99

26. Lewandowski M, Pasternak M, Haugsvær M and Løvås T. Simulations of ammonia spray evaporation, cooling, mixture formation and combustion in a direct injection compression ignition engine. International Journal of Hydrogen Energy. Under Review

27. Li T, Zhou X, Wang N, Wang X, Chen R, Li S and Yi P. A comparison between low-and high-pressure injection dual-fuel modes of diesel-pilot-ignition ammonia combustion engines. Journal of the Energy Institute 2022; 102:362–73

28. Scharl V and Sattelmayer T. Ignition and combustion characteristics of diesel piloted ammonia injections. Fuel Communications 2022; 11:100068

29. Frankl S, Gleis S, Karmann S, Prager M and Wachtmeister G. Investigation of ammonia and hydrogen as CO2-free fuels for heavy duty engines using a high pressure dual fuel combustion process. International Journal of Engine Research 2021; 22:3196–208

30. Duronio F, De Vita A, Allocca L, Montanaro A, Ranieri S and Villante C. CFD numerical reconstruction of the flash boiling gasoline spray morphology. Tech. rep. SAE Technical Paper, 2020

31. Pelé R, Mounam-Rousselle C, Bréquigny P, Hespel C and Bellettre J. First study on ammonia spray characteristics with a current GDI engine injector. Fuels 2021; 2:253–71

32. Xu M, Zhang Y, Zeng W, Zhang G and Zhang M. Flash boiling: easy and better way to generate ideal sprays than the high injection pressure. SAE International Journal of Fuels and Lubricants 2013; 6:137–48

33. Li S, Li T, Wang N, Zhou X, Chen R and Yi P. An investigation on near-field and far-field characteristics of superheated ammonia spray. Fuel 2022; 324:124683

34. Lewandowski M and Pasternak M. 3D CFD modelling of ammonia injection: Work package 3 Milestone report 1. Unpublished report within project ACTIVATE 2021 :405–12

35. Gaucherand J, Netzer C, Lewandowski MT and Løvås T. Modelling of liquid injection of ammonia in a direct injector using Reynolds-averaged Navier–Stokes simulation. Scandinavian Simulation Society 2022 :405–12

36. Zhang Y, Xu L, Zhu Y, Xu S and Bai XS. Numerical study on liquid ammonia direct injection spray characteristics under engine-relevant conditions. Applied Energy 2023; 334:120680

37. Battistoni M, Zembi J, Pandal A, Rousselle C, Pelé R, Brequigny P and Hespel C. Numerical Study of Ammonia Spray with a GDI Engine Injector. *1st Symposium on Ammonia Energy*. Presentation. Cardiff, UK, 2022 Feb

38. Pandal A, Zembi J, Battistoni M, Hespel C, Pele R, BREQUIGNY P and Rousselle C. GDI Ammonia Spray Numerical Simulation by Means of OpenFOAM. Tech. rep. SAE Technical Paper, 2023

39. Ailaboina A and Saha K. On Modeling of Spray G ECN Using ROI-based Eulerian-Lagrangian Simulation. Frontiers in Mechanical Engineering :56

40. Lewandowski M, Pasternak M and Løvås T. Simulations of ammonia spray evaporation, cooling and mixture formation in a direct injection compression ignition engine. *7th International Conference on Contemporary Problems of Thermal Engineering*. Poland, 2022 Feb

41. ConvergentScience. CONVERGE 3.0 Manual. Available from: https://hub.convergecfd.com/downloads/category/22-documentation [Accessed on: 2022 Sep 1]

42. Haugsvær M. Computational Fluid Dynamic Simulations of Liquid Ammonia Spray. Project Work. Internal Report. NTNU, 2022

43. Cheng Q, Ojanen K, Diao Y, Kaario O and Larmi M. Dynamics of the ammonia spray using high-speed schlieren imaging. SAE International Journal of Advances and Current Practices in Mobility 2022; 4:1138–53

44. Zhang Z, Long W, Dong P, Tian H, Tian J, Li B and Wang Y. Performance characteristics of a two-stroke low speed engine applying ammonia/diesel dual direct injection strategy. Fuel 2023; 332:126086

45. Fang Y, Ma X, Zhang Y, Li Y, Zhang K, Jiang C, Wang Z and Shuai S. Experimental Investigation of High-Pressure Liquid Ammonia Injection under Non-Flash Boiling and Flash Boiling Conditions. Energies 2023; 16:2843

46. Bjørgen K, Borsheim N and Løvaas T. Momentum Flux Measurements of Liquid Injection of Ammonia using a GDI Injector. *Proceedings of the European Combustion Meeting 2023*. Norwegian University of Science, Technology, Department of Energy and Process Engineering. Trondheim, Norway, 2023

47. Zuo B, Gomes A and Rutland C. Studies of superheated fuel spray structures and vaporization in GDI engines. *Eleventh international multidimensional engine modeling user's group meeting*. 2000

48. Adachi M, Tanaka D, Hojyo Y, Al-Roub M, Senda J and Fujimoto H. Measurement of fuel vapor concentration in flash boiling spray by infrared extinction/scattering technique. JSAE review 1996; 17:231–7

49. Price C, Hamzehloo A, Aleiferis P and Richardson D. An approach to modeling flash-boiling fuel sprays for direct-injection spark-ignition engines. Atomization and Sprays 2016; 26

50. Shin J and Park S. An ammonia flash break-up model based on bubble dynamics with force and energy analysis on droplet. Fuel 2023; 342:127841

51. An Z, Xing J and Kurose R. Numerical study on the phase change and spray characteristics of liquid ammonia flash spray. Fuel 2023; 345:128229

52. Liu L, Wu Y and Wang Y. Numerical investigation on the combustion and emission characteristics of ammonia in a low-speed two-stroke marine engine. Fuel 2022; 314:122727

53. Wang Y, Zhou X and Liu L. Feasibility study of hydrogen jet flame ignition of ammonia fuel in marine low speed engine. International Journal of Hydrogen Energy 2023; 48:327–36

54. Price C, Hamzehloo A, Aleiferis P and Richardson D. Numerical modelling of fuel spray formation and collapse from multi-hole injectors under flash-boiling conditions. Fuel 2018; 221:518–41

55. Kamoun H, Lamanna G, Weigand B and Steelant J. High-speed shadowgraphy investigations of superheated liquid jet atomisation. ILASS Americas 2010

56. Price C, Hamzehloo A, Aleiferis P and Richardson D. Numerical modelling of droplet breakup for flash-boiling fuel spray predictions. International Journal of Multiphase Flow 2020; 125:103183

57. Duronio F, Di Mascio A, Villante C, Anatone M and De Vita A. ECN Spray G: Coupled Eulerian internal nozzle flow and Lagrangian spray simulation in flash boiling conditions. International Journal of Engine Research 2022 :1530–44

58. Gao S, Yan J, Lee TH and Lee CF. Model development for flash boiling spray and validations with isooctane, hexane, ethanol and their binary mixtures. Fuel 2022; 321:123917

59. Price C, Hamzehloo A, Aleiferis P and Richardson D. Aspects of numerical modelling of flash-boiling fuel sprays. SAE Technical Paper 2015; 24:2463

60. Reitz R et al. Modeling atomization processes in high-pressure vaporizing sprays. Atomisation and Spray technology 1987; 3:309–37

61. Network EEC. ECN Engine Combustion Network. Available from: https://ecn.sandia.gov/gasoline-spray-combustion/ [Accessed on: 2022 Dec 7]

62. O'Rourke PJ and Amsden AA. The TAB method for numerical calculation of spray droplet breakup. Tech. rep. Los Alamos National Lab.(LANL), Los Alamos, NM (United States), 1987

63. Reiter AJ and Kong SC. Demonstration of compression-ignition engine combustion using ammonia in reducing greenhouse gas emissions. Energy & Fuels 2008; 22:2963–71

64. Sher E, Bar-Kohany T and Rashkovan A. Flash-boiling atomization. Progress in energy and combustion science 2008; 34:417–39

65. Plesset MS and Prosperetti A. Bubble dynamics and cavitation. Annual review of fluid mechanics 1977; 9:145–85

66. Patterson MA and Reitz RD. Modeling the effects of fuel spray characteristics on diesel engine combustion and emission. SAE transactions 1998 :27–43

67. Yakhot V, Orszag S, Thangam S, Gatski T and Speziale C. Development of turbulence models for shear flows by a double expansion technique. Physics of Fluids A: Fluid Dynamics 1992; 4:1510–20

68. Liu AB, Mather D and Reitz RD. Modeling the effects of drop drag and breakup on fuel sprays. SAE Transactions 1993 :83–95

69. Amsden AA, O'Rourke PJ and Butler TD. KIVA-II: A computer program for chemically reactive flows with sprays. Tech. rep. Los Alamos National Lab.(LANL), Los Alamos, NM (United States), 1989

70. Schmidt DP and Rutland C. A new droplet collision algorithm. Journal of Computational Physics 2000; 164:62–80

71. Post SL and Abraham J. Modeling the outcome of drop–drop collisions in Diesel sprays. International Journal of Multiphase Flow 2002; 28:997–1019

72. Faeth G. Current status of droplet and liquid combustion. *Energy and combustion science*. Elsevier, 1979 :149–82

73. Reitz RD. Mechanism of breakup of round liquid jets. Encyclopedia of fluid mechanics 1986; 10

74. Xin J, Ricart L and Reitz R. Computer modeling of diesel spray atomization and combustion. Combustion science and technology 1998; 137:171–94

75. Joseph DD, Belanger J and Beavers G. Breakup of a liquid drop suddenly exposed to a high-speed airstream. International Journal of Multiphase Flow 1999; 25:1263–303

76. Beale JC. Modeling fuel injection using Kelvin-Helmholtz/Rayleigh-Taylor hybrid atomization model in KIVA-3V. University of Wisconsin–Madison, 1999

77. Senecal P, Pomraning E, Richards K and Som S. Grid-convergent spray models for internal combustion engine CFD simulations. *Internal Combustion Engine Division Fall Technical Conference*. Vol. 55096. American Society of Mechanical Engineers. 2012 :697–710

78. Lewandowski MT, Netzer C, Emberson DR and Løvås T. Numerical investigation of optimal flow conditions in an optically accessed compression ignition engine. Transportation Engineering 2020; 2:100036

79. Xue Q, Som S, Senecal PK and Pomraning E. Large eddy simulation of fuel-spray under non-reacting IC engine conditions. Atomization and Sprays 2013; 23

80. Xu L, Bai XS, Jia M, Qian Y, Qiao X and Lu X. Experimental and modeling study of liquid fuel injection and combustion in diesel engines with a common rail injection system. Applied energy 2018; 230:287–304

81. O'Rourke PJ and Amsden A. A spray/wall interaction submodel for the KIVA-3 wall film model. SAE transactions 2000 :281–98

82. Xu L, Chang Y, Treacy M, Zhou Y, Jia M and Bai XS. A skeletal chemical kinetic mechanism for ammonia/n-heptane combustion. Fuel 2023; 331:125830

Appendix

A Angle measurements Part 2

The measurement of the spray angles at half penetration in Figure 34 is presented in Figure 50

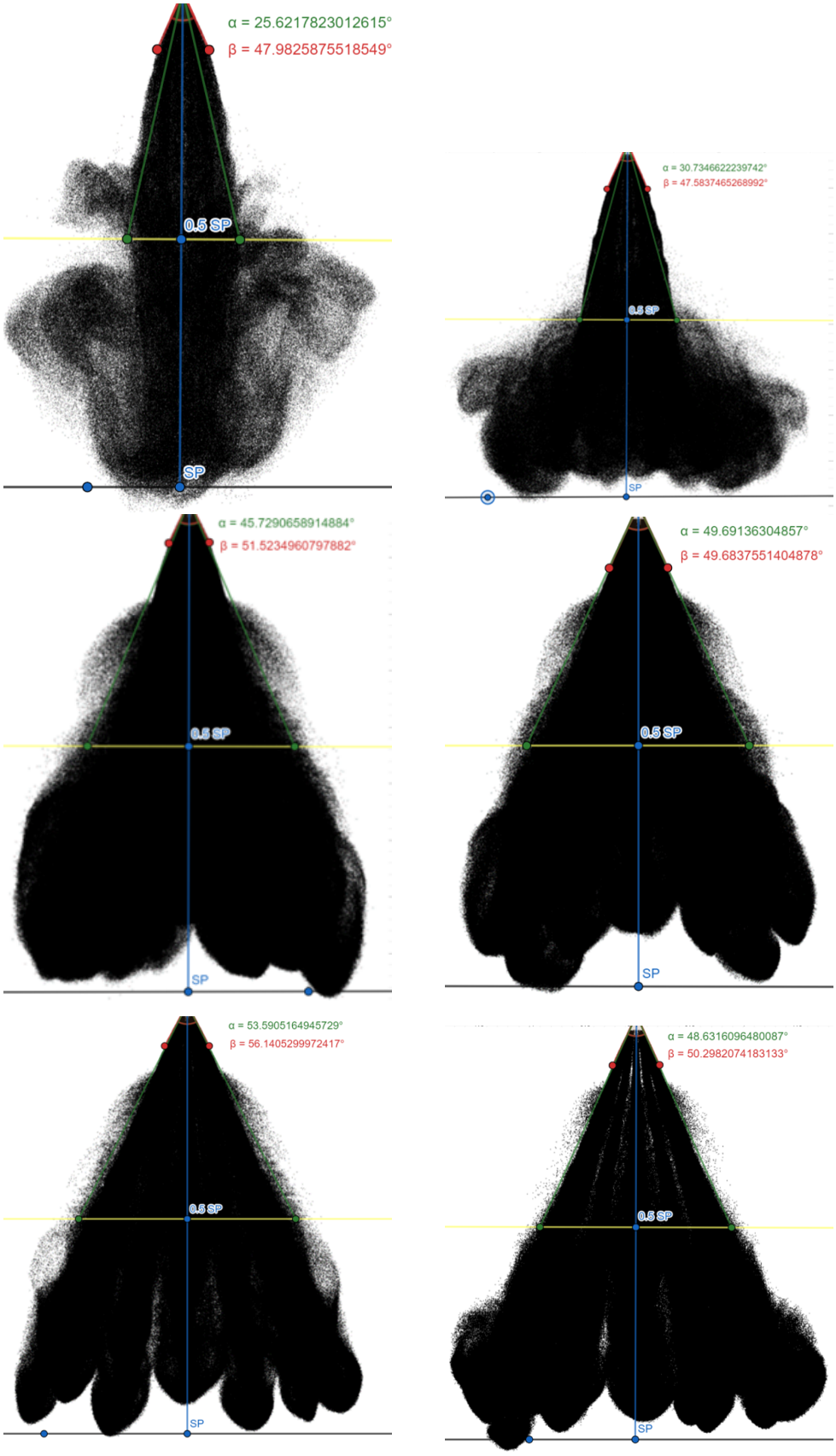

Figure 50: Measurements of spray angle. both near injector and at half penetration length 2 ms after start of injection. From top left corner 2,4,7,10,15,25 bar

B Preliminary near nozzle measurements from Lab

Figure 50 shows the Preliminary near nozzle measurements from the EPT motor lab at NTNU. These measurements are from a 6-hole GDI injector, similar to that fitted in the dual fuel engine in the EPT motor lab. 10 bar and 5 bar ambient pressure are considered and the fuel temperature is assumed to be 293 K $P_s = 8.6$ bar. There was 360 µs of lag, meaning that the time of 0.5 ms corresponds to 0.14 ms after the start of the injection. for subcooled case: cone angle around 20-21 ˚approximately. As seen in Figure 50 superheated: plumes are increased, but the increase is not possible to quantify from current pictures.

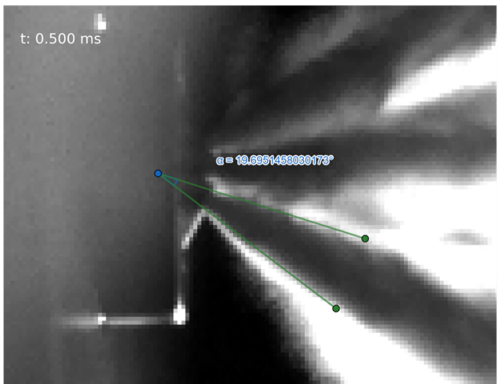

Figure 51: 0.5 ms, $\frac{P_a}{P_s} = 1.16$

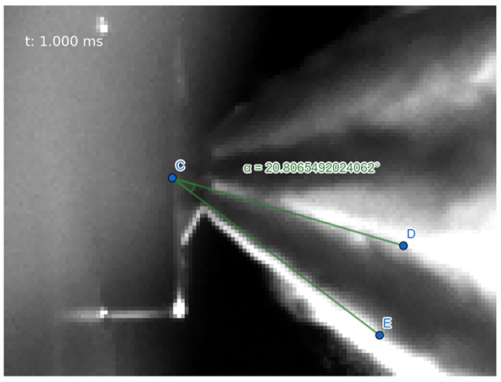

Figure 53: 1 ms, $\frac{P_a}{P_s} = 1.16$

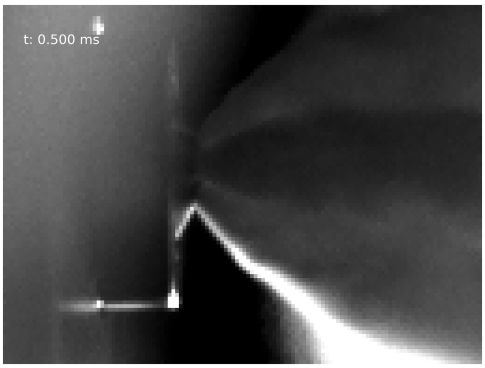

Figure 52: 0.5 ms, $\frac{P_a}{P_s} = 0.58$

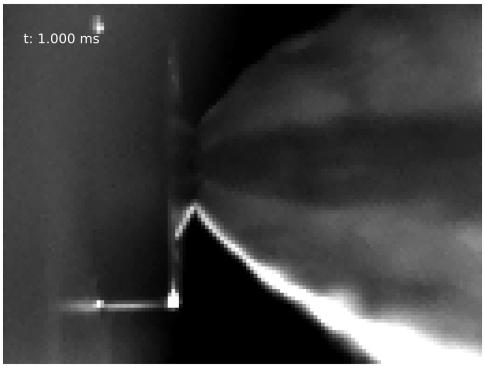

Figure 54: 1 ms, $\frac{P_a}{P_s} = 0.58$

Figure 55: picture of near nozzle behaviour from lab. injection pressure of

C Temperature model for higher pressures

The more accurate discretized temperature model has been used for the flashing case considered in the parametric study solving for droplet larger than 1 μm as the simplified temperature models tends to overpredict evaporation [41]. Figure 56 shows the pressure condition of 7 bar ($\frac{P_a}{P_s} = 0.81$ transition region) and with breakup as GDI-non flash tested with the two different approaches for calculating droplet temperature.

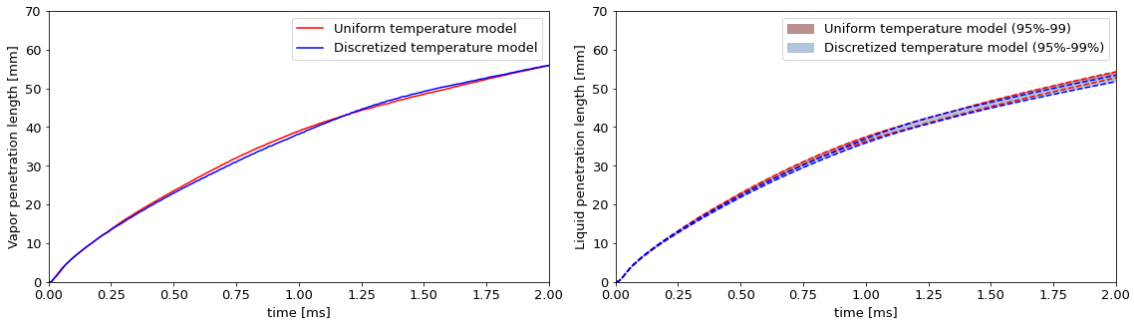

Figure 56: Effect of temperature model on weak flash conditions. Pressure 7 bar KH-RT GDI non-flash

As seen in Figure, there is no apparent difference in temperature models. For less superheated conditions and for subcooled spray, the computationally expensive discretized temperature model is not necessary, and the uniform temperature model will be used.

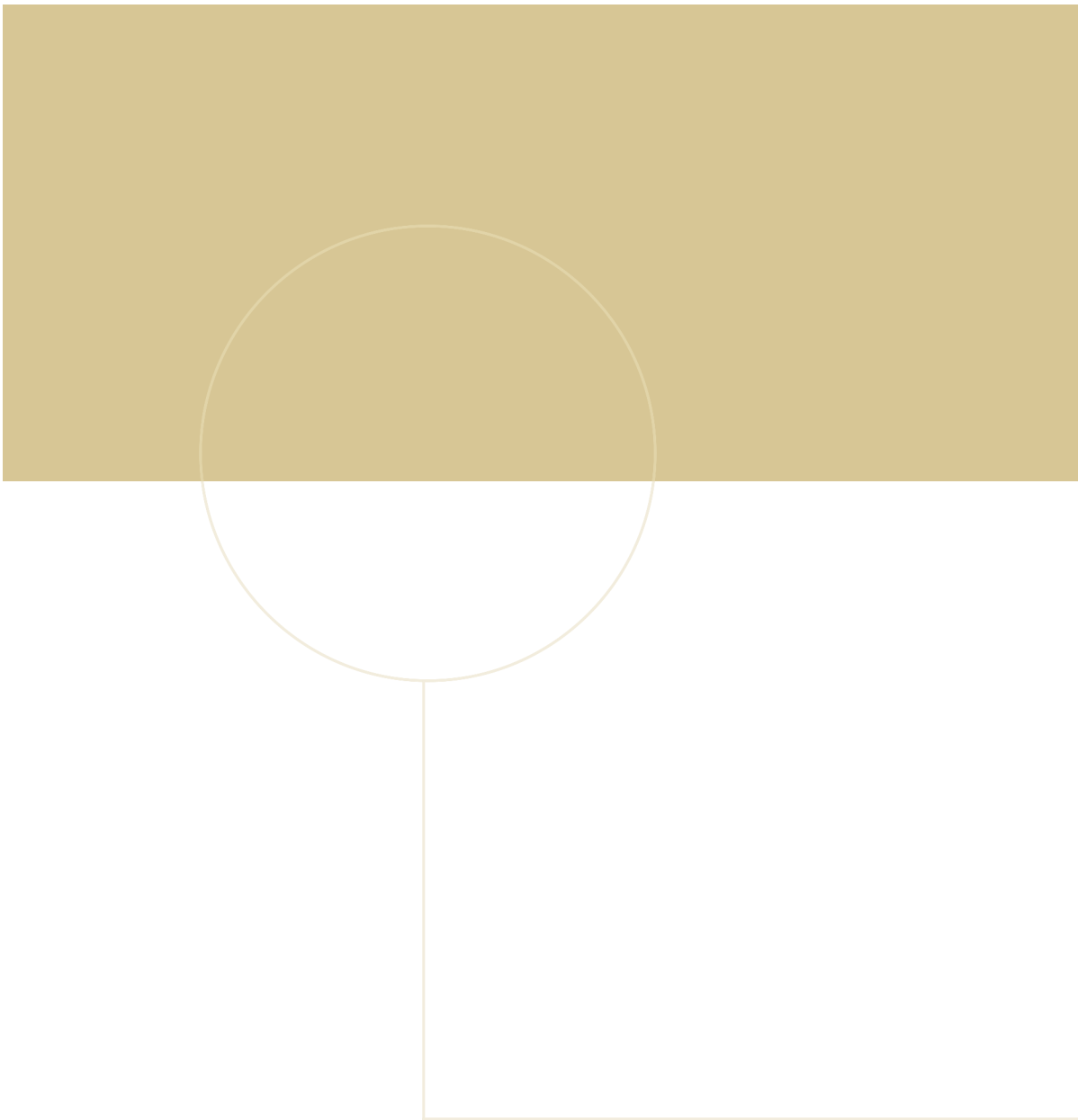

NTNU

Norwegian University of
Science and Technology